TECHNISCHE
UNIVERSITÄT
DARMSTADT

Physik

Internal structure and dynamics of PNIPAM based microgels in bulk and adsorbed state at different internal crosslinker distributions

Dem Fachbereich Physik
der Technischen Universität Darmstadt

zur Erlangung des Grades
eines Doktors der Naturwissenschaften (Dr. rer. nat.)

Dissertation von
M. Sc. Tetyana Kyrey
(Ukraine)

Erstgutachterin: Prof. Dr. Regine von Klitzing
Zweitgutachterin: Prof. Dr. Christine Papadakis

Darmstadt 2019
D17

Kyrey, Tetyana: Internal structure and dynamics of PNIPAM based microgels in bulk and adsorbed state at different internal crosslinker distributions
Darmstadt, Technische Universität Darmstadt
Jahr der Veröffentlichung der Dissertation auf TUprints: 2019
URN: urn:nbn:de:tuda-tuprints-94781
Tag der mündlichen Prüfung: 13.11.2019

TECHNISCHE
UNIVERSITÄT
DARMSTADT

Erklärung gemäß §9 Promotionsordnung

Hiermit versichere ich, dass ich die vorliegende Dissertation selbstständig angefertigt und keine anderen als die angegebenen quellen und Hilfsmittel verwendet habe. Alle wörtlichen und paraphrasierten Zitate wurden angemessen kenntlich gemacht. Die Arbeit hat bisher noch nicht zu Prüfungszwecken gedient.

_____

Datum und Unterschrift

You cannot hope to build a better world without improving the individuals.
To that end each of us must work for his own improvement.

– Marie Sklodowska Curie –

Acknowledgments

There are many persons who supported me during the time of my PhD and in a certain way contributed to the work. At this point I would like to express my gratitude to all of them.

My special thanks are to Prof. Dr. Regine von Klitzing for the opportunity of gaining the doctorate under her supervision, her constant interest in this work and efficient scientific discussions.

I thank Prof. Dr. Christine Papadakis for agreeing to be the second reviewer.

I would like to express my cordial gratitude to Dr. Olaf Holderer and Dr. Stefan Wellert for their brilliant scientific guidance during my PhD. I deeply appreciate their extremely well mentoring, enthusiastic encouragement, constructive criticism of the present work as well as patience.

I would like to sincerely thank Judith Witte for prosperous collaboration we have had during the last few years and especially for the high quality samples.

Furthermore, I would like to thank the BornAgain group for the excellent software they develop and especially Dr. Marina Ganeva and Dr. Walter Van Herck for the intense discussions we had and help with simulation of the data, which are an important contribution to this work.

I thank Dr. Henrich Frielinghaus, Dr. Vitaliy Pipich, Dr. Artem Feoktystov and Dr. Alexandros Kountsioupas for the helpful discussions and support during the neutron experiments. The performed experiments would not happen without the professional technical and scientific support of Dr. Baohu Wu, Dr. Egor Vezhlev, Dr. Stefan Mattauch, Dr. Aurel Radulesku and Dr. Stefano Pasini.

I'm grateful to Marcus U. Witt the operative sample preparation, Mathias Kühnhammer and Patrick Schöffmann for support in AFM measurements.

For the help in overcoming bureaucratic obstacles I sincerely thank Petra Erdmann, Maria Bülth, Franziska Michels and Monika Krug. Special thanks to Dr. Markus Domschke for continuous support and help in all bureaucratic questions in TU Darmstadt.

I would like to thank JCNS for the excellent opportunity to be involved and be able to perform experiments at the best neutron scattering instruments, for excellent technical support and pleasant working atmosphere.

I thank Deutsche Forschungsgemeinschaft (DFG) [Grants HO 5488/2-1 and WE 5066/3-1] for financial support.

And last but not least, I am grateful to my dear family, and especially to my husband, sister and my dear children for the best emotional support and belief in me. The special thanks to my grand-mother and mother for the correctly guiding me into this life.

Persönlicher Werdegang

Name: Tetyana Kyrey

Geburtsdatum: 26-04-1989

Geburtsort: Brovary (Ukraine)

Nationalität: ukrainisch

12-2016 – heute Promotionsstudium in Rahmen des DFG-Projekts zwischen TU Berlin, TU Darmstadt und Jülich Forschungszentrum GmbH (JCNS am MLZ) unter der Leitung von Prof. Dr. Regine von Klitzing, Garching bei München, Deutschland

09-2010 – 05-2012 Masterstudium in Physik (Schwerpunkt: Medizinische Physik), Nationale Taras-Schewtschenko-Universität Kiew, Ukraine

09-2010 – 05-2012 Masterarbeit im Arbeitskreis von Prof. Dr. Leonid Bulavin und Dr. Mikhail Avdeev, Frank Laboratorium für Neutronenphysik, Vereinigtes Institut für Kernforschung, Dubna, Russland

Master thesis: *"Solvatochromic effect and aggregation process of fullerene C_{60} in liquid solutions with different polarity"*

09-2006 – 06-2010 Bachelorstudium in Physik, Nationale Taras-Schewtschenko-Universität Kiew, Ukraine

02-2010 – 06-2010 Bachelorarbeit im Arbeitskreis von Prof. Dr. Leonid Bulavin und Dr. Mikhail Avdeev, Frank Laboratorium für Neutronenphysik, Vereinigtes Institut für Kernforschung, Dubna, Russland

Bachelorarbeit: *"Solvatochromic effect of fullerene C_{60} liquid solutions"*

List of publications

1. T. Kyrey, M. Ganeva, K. Gawlitza, J. Witt, R. von Klitzing, O. Soltwedel, Zh. Dib, S. Wellert, O. Holderer, Grazing incidence SANS and reflectometry combined with simulation of adsorbed microgel particles, *Physica B: Condensed Matter* (2018) **551**, 172–178, doi: 10.1016/j.physb.2018.03.049.

2. T. Kyrey, J. Witte, M. Gvaramia, S. Wellert, A. Koutsioubas, S. Mattauch, O. Holderer, H. Frielinghaus, Simpler neutron resonator enhances the wave-field for grazing incidence scattering experiments with lower parasitic scattering, *Physica B: Condensed Matter* (2018) **551**, 405–406, doi: 10.1016/j.physb.2018.07.022.

3. H. Frielinghaus, T. Kyrey, O. Holderer, Single channel waveguide with roughness, *JPS Conf. Proc.* (2018) **22**, 011031, doi: 10.7566/JPSCP.22.011031.

4. T. Kyrey, J. Witte, V. Pipich, A. Feoktystov, A. Koutsioubas, E. Vezhlev, H. Frielinghaus, R. von Klitzing, S. Wellert, O. Holderer, Influence of the cross-linker content on adsorbed functionalised microgel coatings, *Polymer* (2019) **169**, 29–35, doi: 10.1016/j.polymer.2019.02.037.

5. J. Witte, T. Kyrey, J. Lutzki, M. Dahl, A. Radulescu, L. Stingaciu, M. Kühnhammer, M. Witt, A comparison of the network structure and inner dynamics of homogeneously and heterogeneously crosslinked PNIPAM microgels with high cross-linker content, *Soft Matter* (2019) **15**, 1053–1064, doi: 10.1039/c8sm02141d.

6. T. Kyrey, J. Witte, A. Feoktystov, V. Pipich, B. Wu, S. Pasini, A. Radulescu, M.U. Witt, M. Kruteva, R. von Klitzing, S. Wellert, O. Holderer, Inner structure and dynamics of microgels with low and medium crosslinker content prepared via surfactant-free precipitation polymerization and continuous monomer feeding approach, *Soft Matter* (2019), **15**, 6536–6546, doi: 10.1039/C9SM01161G

7. J. Witte, P. Krause, T. Kyrey, M. Ganeva, A. M. Dahl, A. Koutsioubas, B. Schmidt, J. Lutzki, O. Holderer, S. Wellert, Grazing incidence neutron spin echo study of PNIPAM brushes, *Macromolecules* (2019), submitted.

8. T. Kyrey, M. Ganeva, J. Witte, R. von Klitzing, S. Wellert, O. Holderer, Evanescent wave simulations: challenges and opportunities for the interpretation of grazing incidence scattering experiments (2019), in preparation.

Abstract

Stimuli-responsive microgels are a unique class of polymer structures which can undergo a fast response to an external trigger such as light, temperature or pH. It provides a wide potential application spectrum in optical devices, smart surface coatings, emulsion stabilisation etc. The most prominent example of these microgels are poly(N – isopropylacrylamide)(PNIPAM) microgels.

During the last decades PNIPAM-based microgels were widely studied and serve nowadays as model systems for the investigation of the basic properties of microgels and the principles of supported transport of active substances, e.g. drug delivery. The responsive behaviour of the microgels is governed by the polymer network structure, i.e. the crosslinking of the polymer chains has a considerable influence on the physico-chemical and mechanical properties of the microgels. Especially the amount and the crosslinker distribution within a single microgel have a high relevance for the application as well as for the understanding of the microgel nature.

This thesis focuses on a detailed analysis of microgels in solution and at interfaces with scattering experiments. Neutron and X-ray scattering provide a unique insight into the structure and dynamics of microgels, especially at the interface with grazing incidence small angle neutron scattering and neutron spin-echo spectroscopy (GISANS and GINSES). New insights into the inner structure and dynamics have been gained with improved experimental conditions and data analysis.

This thesis is divided into the two main parts. In order to characterise the internal structure and dynamics of the PNIPAM microgels with respect to the crosslinker (N,N' – methylenebis(acrylamide), BIS) distribution, sophisticated analysis of the internal microgel (domain-like) structure and studies of its influence on the polymer dynamics in nanometer and nanosecond scales are presented in the first part of the thesis. In the context of smart polymer coatings, the influence of the confinement to the solid surface on the internal architecture and the thermoresponsiveness of the adsorbed PNIPAM microgels is investigated. It is shown that in contrast to the atomic force microscopy, the inhomogeneities of the polymer network of the adsorbed soft microgels can be achieved with surface sensitive neutron reflectometry and GISANS.

The second part of the thesis aims at the peculiarities of the scattering experiments of thin polymer layers under grazing incidence conditions. Simulation of the scattering signal within the Distorted Wave Born Approximation is presented in order to improve the analysis of the GINSES data and to simplify the initial planing and performance of the grazing incidence experiments.

The main impacts of this thesis are (i) an extended description of the complex internal structure, dynamics and the thermoresponsiveness of the PNIPAM microgel before and after adsorption onto a solid surface and (ii) demonstration the advantages of the investigation

of the polymer systems at grazing incidence conditions in combination with numerical simulations.

Zusammenfassung

Stimuli-responsive Mikrogele gehören zu der einzigartigen Klasse von Polymerstrukturen, die schnell auf externe Auslöser wie Licht, Temperatur oder pH-Wert reagieren. Es bietet breite potenzielle Anwendungsmöglichkeiten für optische Geräte, intelligente Oberflächenbeschichtungen mit schaltbaren optischen Eigenschaften, Emulsionsstabilisierung etc. Der bekannteste Vertreter dieser Mikrogele sind Poly(*N*-isopropylacrylamid)(PNIPAM)-basierte Mikrogele.

In den letzten Jahrzehnten wurden PNIPAM-Mikrogele umfassend untersucht und dienen heute als Modellsysteme zur Untersuchung der Mikrogeleigenschaften und beispielsweise der Prinzipien des unterstützten Transports von Wirkstoffen, z.B. der Wirkstoffabgabe. Das responsive Verhalten der Mikrogelen ist durch die Polymernetzstruktur bestimmt, d.h. die Vernetzung der Polymerketten hat einen erheblichen Einfluss auf die physikalisch-chemischen und mechanischen Eigenschaften der Mikrogele. Insbesondere die Menge und die Vernetzerverteilung innerhalb eines einzelnen Mikrogels haben eine hohe Relevanz für die Anwendung sowie für das Verständnis der Eigenschaften des Mikrogels.

Neutronen- und Röntgenstreuung bieten hierbei Einblicke in die Struktur und Dynamik von Mikrogelen. Insbesondere an Grenzflächen sind es die Kleinwinkel-Neutronenstreuung und Neutronen Spin-Echo Spektroskopie unter streifendem Einfall (GISANS und GINSES). In dieser Arbeit sind Mikrogele in Lösung und an Grenzflächen mit Streuexperimenten detailliert untersucht und durch verbesserte experimentelle Bedingungen und Datenanalyse neue Einblicke in die interne Struktur und Dynamik gewonnen worden.

Diese Dissertationsarbeit ist in zwei wichtige Teilen aufgeteilt. Um die interne Struktur und Dynamik der PNIPAM-Mikrogele in Bezug auf die Verteilung des Quervernetzer (*N,N'*-Methylenebisacrylamide, BIS) zu charakterisieren, wurde im ersten Teil dieser Arbeit eine Analyse der internen Inhomogenität des Mikrogels und Untersuchungen ihres Einflusses auf die Polymerdynamik im Nanometer- und Nanosekundenbereich durchgeführt. Für zweidimensionale Polymer-Beschichtungen wird der Einfluss der harten Grenzfläche auf die innere Struktur und die Thermoresponsivität der adsorbierten PNIPAM Mikrogele dargestellt. Es wird gezeigt, dass im Gegensatz zum AFM die internen Strukturparameter der adsorbierten weichen Mikrogele mit oberflächenempfindlichen Neutronenstreuungstechniken wie Neutronenreflektometrie und GISANS ermittelt werden können.

Der zweite Teil der Arbeit zielt auf die Besonderheiten der Streuexperimente dünner Polymerschichten unter streifenden Einfallsbedingungen. Die Simulation des Streusignals innerhalb der Distorted Wave Born Approximation wird in Bezug auf die Verbesserung der Analyse der GINSES-Daten und die Vereinfachung der anfänglichen Planung und Durchführung der Experimente in Geometrie unter streifendem Einfall vorgestellt.

Die wichtigste Auswirkung dieser Arbeit ist eine erweiterte Beschreibung der komplexen internen Struktur, Dynamik und der Thermoresponsivität des PNIPAM-Mikrogels

vor und nach der Adsorption an feste Oberflächen und die Demonstration der Vorteile der Untersuchung der Polymersysteme mit grenzflächenempfindlichen Streumethoden in Kombination mit numerischen Simulationen.

Contents

Chapter 1

Introduction

More than half of the century environmentally sensitive polymer structures attract a high scientific attention due to their unique ability to respond to an external stimulus, such as temperature, pH, light or solvent quality. The sensitivity of their swelling ability in three- or two-dimensional arrays inspired a fulfil discussion of their application as bio-sensors, protection coating or controlled drug-release.

One prominent representative of a stimuli-responsive system are microgels based on the poly(*N*-isopropylacrylamide) (PNIPAM). Below the volume phase transition temperature (VPTT) the PNIPAM polymer chains are swollen in water, while at higher temperatures (above the VPTT) the polymer partially releases water molecules and a decrease of the microgel size due to the chain collapse occurs. Due to its VPTT that is close to the physiological temperature (∼32 °C), the PNIPAM serves as a model system for bio-relevant research.

The physical and chemical properties (and further applications) of the microgel directly depend on its macro- and micro parameters. Therefore, a thorough characterization of the internal structure and dynamics of the microgels on different length- and time-scales is of high importance. A clear understanding of the stimuli-sensitive microgel properties in bulk as well as in adsorbed state is demanded. However, the access to the nanoscale properties becomes the most challenging task, especially at the presence of a solid surface. At this point, scattering techniques with neutron and X-ray come into play, providing the right length- and time-scales with suitable contrast conditions.

Classical transmission geometry is not suitable for the structure and dynamics investigation of the adsorbed polymer films due to the low scattering volume, and the grazing incidence geometry becomes more suitable. While the grazing incidence small-angle neutron and X-ray scattering are commonly used for structure investigations, grazing incidence neutron spin-echo spectroscopy is a novel technique for the study of dynamics of microgels, microemulsions, membranes close to the rigid interface. Combining grazing incidence geometry as well as neutron properties, GINSES is a unique tool accessing internal thermally driven dynamics of polymer and bio-systems. However, experiment performance as well as further data analysis are the challenging tasks nowadays.

Therefore, this thesis is dedicated to two main tasks. The first one aims at the fundamental understanding of the complex internal structure of the individual PNIPAM microgel and its influence on the polymer dynamics in dependence on (i) the preparation process, (ii) microgel composition (ratio of the chemical components) and (iii) space confinement: in bulk and adsorbed state (Chapter 4–5). The second task of the thesis is

the solution of the problems emerging during the investigations of the polymer systems at the grazing incidence conditions (Chapter 6–7).

In particular, Chapter 4 of this thesis deals with the PNIPAM microgels prepared via batch- and feeding approaches in bulk state. Application of the different preparation processes permits the variation of the internal structure and thus the properties of the microgels. Structure and dynamics of the microgels were studied by means of dynamic light scattering, small-/very small-angle neutron and X-ray scattering and neutron spin-echo spectroscopy. The combination of such methods allows a detailed structure description within a single microgel at different temperature conditions, namely in swollen and collapsed state. Moreover, the influence of the amount and the distribution of the crosslinker within the microgel network on its internal structure and dynamics is studied.

With respect to the possible application of the adsorbed polymer microgels as protect coating or sensoric devices, the low- and medium crosslinked PNIPAM microgels prepared via batch synthesis and adsorbed onto a silicon block were studied in Chapter 5. To reach information about structural arrangement of the microgels in the vicinity to the solid surface, surface-sensitive neutron scattering methods were applied. Namely, with neutron reflectometry the polymer density profile of the adsorbed microgels was probed in direction normal to surface when microgels are in the swollen state. The influence of the solid surface and temperature variation on the internal structure of the PNIPAM films was investigated with grazing incidence small-angle neutron scattering (GISANS). Complementary information on the shape of the microgels was obtained with atomic force microscopy (AFM).

In Chapter 6 it is shown, how computer simulations in the frame of the Distorted Wave Born Approximation can improve the GISANS and GINSES data treatment and help to understand the polymer dynamics in the vicinity to the solid surface. The peculiarities and pitfalls of modelling continuous density changes by a surface roughness parameters are demonstrated.

Chapter 7 aims at solving the problems of low intensity scattering signal under grazing incidence conditions. A test of a simple 3-layer resonator is presented. The influence of the resonating structure positioned between solid surface and polymer system on the scattering intensity is demonstrated.

The basic theory which is essential for the understanding of the characteristic process inhered to the microgels and principles of the scattering methods applied for the microgel characterisation and theoretical models used for the experimental data treatment are presented in Chapter 2. Microgel preparation process as well as instrumental setups and experiment configuration are introduced in Chapter 3.

Chapter 2

Theoretical background

Within scope of this chapter the broad scientific background corresponding to the objects and experimental methods of the current thesis are presented. The first part is dedicated to the PNIPAM microgels. Current state of the investigations and open questions are discussed. In the second part of the chapter the main principles of the used experimental techniques and applied theoretical models are described.

2.1 Stimuli responsive microgels

Microgels are colloidal particles consisting of a three-dimensional chemically or physically cross-linked network structure. When dispersed in a good solvent, these particles are highly swollen with sizes ranging from 100 to 1000 nm.

The main feature of the stimuli-responsive or intelligent microgels is the ability to alter their swelling degree due to the change of the external variables such as temperature, pH, light or solvent quality[1–12]. *Tanaka*[13] showed, that the radius of the gel (R) and its diffusion coefficient (D) determine the characteristic time (τ) of the gel volume changes as presented in Eq. 2.1. Thus, microgels possess similar properties to a gel with the same content, but due to size exhibit faster respond on the changes of the environment[14].

$$\tau = \frac{R^2}{\pi^2 D} \tag{2.1}$$

Such unique ability raises a huge interest during the last half a century and open a wide opportunity for the practical application: for drug delivery, sensors, biotechnological application, etc.[15–24].

In current work thermoresponsive microgels based on the poly(N-isopropylacrylamide) (PNIPAM) polymer are in sight. Due to a reversible temperature induced volume phase transition, that is close to the physiological temperature, PNIPAM microgels serve as a model systems for the basic research and have been studied intensively[1–7,25–28].

At first thermoresponsiveness of PNIPAM was investigated in 1960s by Heskin and Guillet[29]. The lower critical solution temperature (LCST) of the monomer (NIPAM) leads to a reversible volume phase transition (VPT) at a typical temperature of around 32°C in water. The change of the temperature allows to tune polymer properties. At temperature below the LCST the amide groups of the polymer interact strongly with the water through the hydrogen bonding. At higher temperature the hydrogen bonding is broken and intra- or inter-molecular hydrogen bonds are formed. Water becomes a poor solvent and the

phase separation occurs. A crosslinked PNIPAM undergoes a sharp transition from highly swollen to shrunken network by crossing the VPTT (conformational from coil-to-globule transition)[30,31]. The schematic illustration of the PNIPAM microgel swelling/deswelling due to the temperature change is presented in Figure 2.1A.

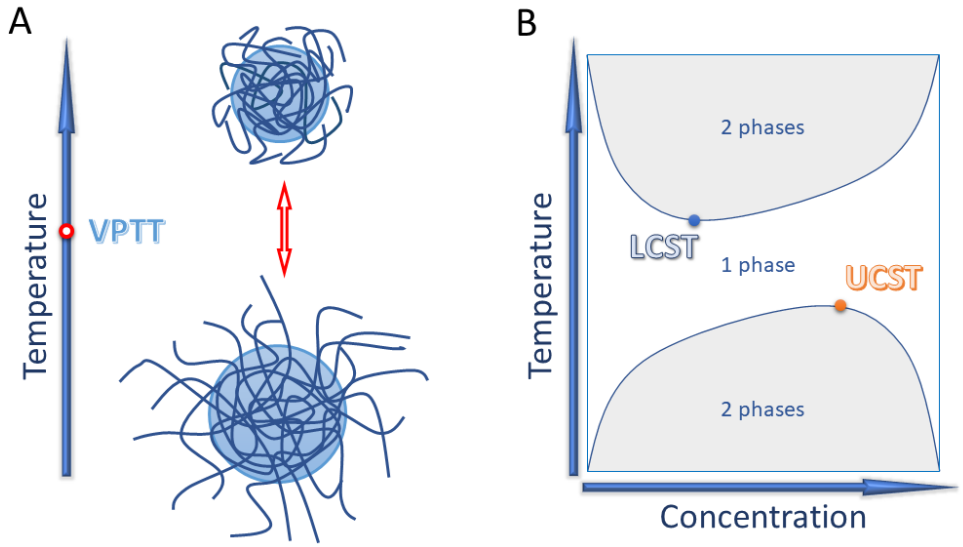

Figure 2.1: A: Temperature transition of the PNIPAM microgel. B: Polymer phase diagram with upper (UCST) or lower (LCST) critical solution temperature (reproduced according to Ref.[32]).

In Figure 2.1B the general phase diagram of a thermoresponsive polymer system with lower (LCST) or upper (UCST) critical solution temperature is presented. According to this diagram they can exhibit two phase or one phase structure depending on the temperature and polymer concentration in solution.

From the diagram, LCST is the minimum of the binodal and thus for a polymer solution exhibiting a LCST such as PNIPAM. The polymer and solvent mix at all concentrations at the temperature below LCST[33].

2.1.1 Influence of the crosslinker on microgels

To prevent dissolving of the polymer in water crosslinking comonomer is used[20]. *N,N'*-methylenebisacrylamide (BIS) is commonly used as a crosslinker in PNIPAM microgels. *Wu et al.*[34] showed that the crosslinker BIS possesses faster consumption compared to NIPAM. It leads to a uniform internal microgel composition. Due to the distribution and incorporation of the crosslinker molecules during the preparation process, different types of polymer inhomogeneities in the microgel can be formed[35].

According to *Bastide and Leibler*[36], the microgel network in swollen state could be described in the framework of the mesh model. In this model, the microgel is considered as a combination of blobs and their connection with each other corresponding to the crosslinkers and PNIPAM chains respectively (Figure 2.2). A decrease of temperature and swelling process lead to an inhomogeneous polymer chain conformations in the microgels. There the formation of the domains with frozen neighbour-junctions which do not swell homogeneously occurs (Figure 2.2B).

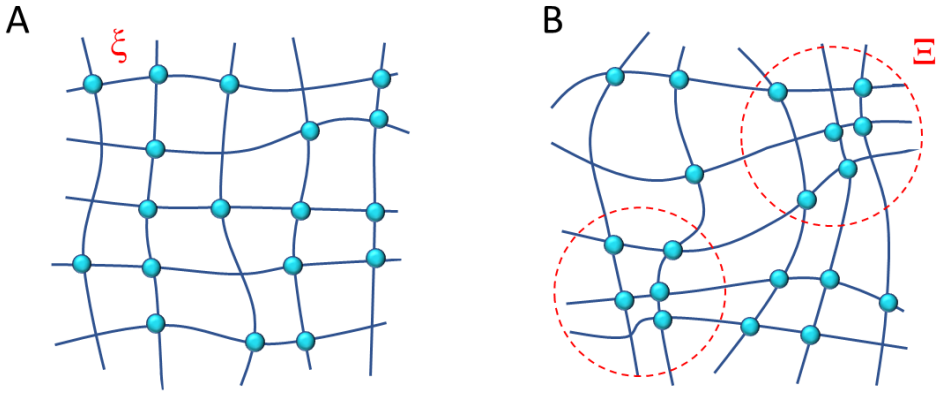

Figure 2.2: Illustration of the mesh model: A) a two-dimensional reaction bath well above the chain gelation threshold, B) a swollen gel by the addition of solvent. The blue dots represent interchain cross-links. Dashed-circles depict domains with frozen neighbour-junctions which do not swell. Reproduced according to Ref.[36].

In the frame of the mesh model, internal concentration fluctuations can be described as a sum of the thermal fluctuations and static inhomogeneities. Thermal fluctuation is time-dependent, while the static inhomogeneities are time-independent and appears because of the inhomogeneous crosslinking density of the polymer network[35]. The combination of both fluctuation types are presented in Fig. 2.3.

A sophisticated statistic theory of the polymer gels proposed by *Panyukov and Rabin*[37] allows quantitative description of the internal inhomogeneities. According to the Panyukov-Rabin theory the concentration fluctuation can be presented as a sum of the thermal and frozen concentration fluctuation, that reads:

$$\rho(r) = \rho^{th}(r) + \rho^{eq}(r) \tag{2.2}$$

where $\rho^{th}(r)$ is the thermal concentration fluctuation and $\rho^{eq}(r)$ is the static or equilibrium inhomogeneities introduced by the crosslinking reaction.

Variation of the crosslinker distribution. The different internal crosslinker distribution

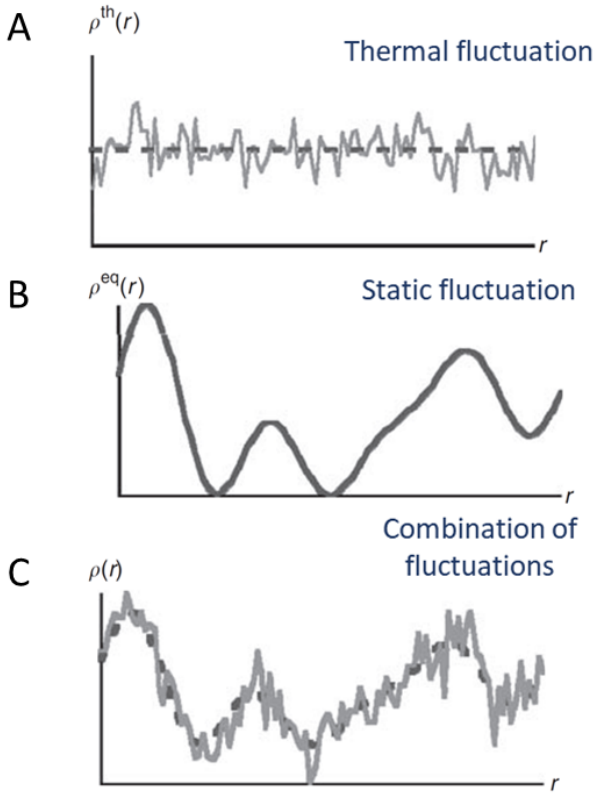

Figure 2.3: Thermal (A) and static (B) fluctuations together with their combination (C) along the space coordinate r. Reproduced according to Ref.[35].

within microgels can be achieved via different synthesis routes. In this thesis PNIPAM microgels prepared via batch and feeding synthesis are studied (details of microgel preparation are presented in Section 3.1.1). Microgel preparation via classical precipitation polymerization (batch synthesis) leads to the microgels with a crosslinker-rich core and a fluffy shell[38,39]. Microgel preparation via continuous monomer feeding approach (feeding synthesis) is assumed to lead to a more homogeneous crosslinker distribution[16,17,40,41]. It was observed by a homogeneous elastic modulus and a homogeneous distribution of the embedded nanoparticles within the microgel[40].

Structure of the PNIPAM-based microgels prepared via classical precipitation polymerization in different solvents were extensively studied by means of atomic force microscopy (AFM), dynamic light scattering (DLS) and small-angle X-ray or neutron scattering (SAXS/SANS)[2,23,35,42–44].

It was shown, that such microgels synthesited by the batch method form a core-shell structure with a homogeneous core and a uniform crosslinker distribution and a less dense shell with a polymer density gradient from the core to the outer surface[22,38,43,45–47]. The

core-shell model as well as polymer density (ϕ) as a function of the distance from centre to outer particle part (r) is presented in Figure 2.4.

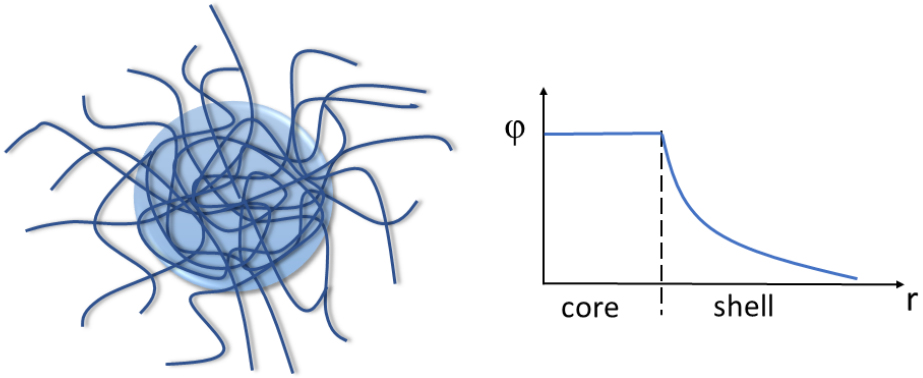

Figure 2.4: Core-shell microgel structure. Graphic represents distribution of the polymer within the microgel according to the core-shell model.

However, *Ikkai et al.*[48] showed, that depending on the microgel size crossing the VPTT can lead to a phase separation. Due to a competition of the hydrophobic and electrostatic interactions at temperature increase, a strong concentration fluctuation appears when the microgel size becomes larger than the wavelength of the concentration fluctuation Λ (see Fig. 2.5). At microgel sizes of a few tens of nanometer, concentration fluctuations are deteriorated by wave-propagation through its surface. Contribution of the microgel surface to the scattering spectra was commonly observed[6,49].

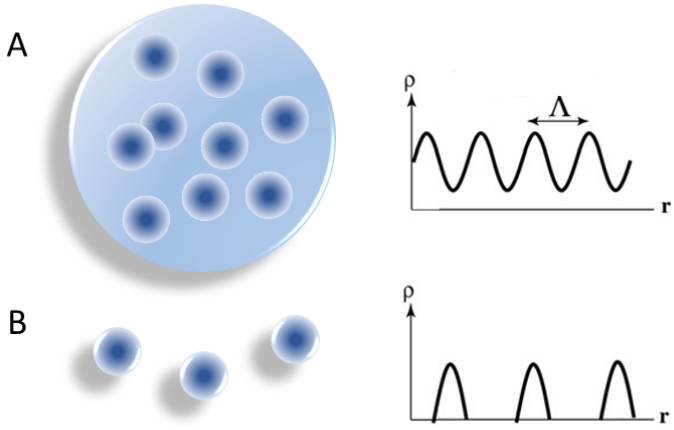

Figure 2.5: Phase separation at temperature above VPTT according to the size of microgel (A – larger than the wavelength of the concentration fluctuation Λ, B – smaller than Λ). Graphs show density (ρ) fluctuation. Reproduced according to Ref.[48].

Studies of more complex microgels composed of polymers with different VPTT with neutron scattering techniques allows more detailed description of the structure within a

single microgel. *Keerl et al.*[50] propose a "dirty snowball" form factor for the description of the nanophase separated internal structure. In a copolymer microgel consisting of PNIPAM and PNIPMAM (*N*-isopropylmethacrylamide) at transition temperature (30°C) the PNIPAM domains ("dirt") are collapsed and the PNIPMAM ("snowball") is still in the swollen state. *Wellert et al.*[51] used a model with two correlation lengths to describe the evolution of the internal structure of the PEG-microgels during synthesis. *Papagiannopoulos et al.*[52] reported about a formation of flower-like micelles below VPTT for triblock PS-PNIPAM-PS polymer microgels.

Very recently, the first attempt to demonstrate a clusters-like internal structure of the PNIPAM microgels was performed with super-resolution fluorescence microscopy[53,54]. By means of fluorophore tagged crosslinker, *Karanastasis et al.*[53] reveal the presence of higher cross-link density clusters embedded in a lower cross-link density matrix within the core of individual microgel. *Siemens at al.*[54] demonstrate a different dependency of polymer and crosslinker density in the PNIPAM/BIS microgel (from center to the outer region). They observed that decrease of the polymer density does not lead directly to the decrease of the crosslinker density and visa versa. However, by means of scattering techniques a detailed information about the internal core structure has never been obtained.

Studies of the internal structure of microgels prepared via continuous monomer feeding approach are very limited. Recent publications focused on studies of the microgels properties by means of optical microscopy or light scattering to prove the homogeneous crosslinker distribution in PNIPAM microgels[55–57]. Such approaches do not give direct access to the internal structure and crosslinker distribution inside of the microgel. Therefore, in this thesis neutron scattering methods, which provide insight into the internal structure, were used for detailed investigation of the internal microgel structure in dependence on the preparation process and crosslinker concentration. Due to the key advantage of the neutrons, namely adjustable scattering contrast by using D_2O as a solvent, and the variation of the q-range, studies of the microgel structures in nm to μm size range were performed (see Chapter 4).

The amount of the crosslinker influences viscoelastic properties and swelling ability of the microgels. Increasing of the crosslinker amount leads to an increase of the solid-like properties and decrease of the swelling capacity[38,58,59]. Moreover, properties of the microgel are closely related to their internal structure. More homogeneous distribution of the crosslinker leads to significantly higher swelling degree[41]. The variation of the mesh size, which depends on the crosslinker distribution, plays a crucial role in the ability of the microgels to control drug delivery, i.e. the microgel matrix is used for a loading of drugs into the polymer network[60]. Therefore, detailed insight into the microgel and investigation

of the internal arrangement within a single microgel is of high importance.

2.1.2 Adsorption of the microgel onto solid surface

Transition of the microgels from 3D to 2D due to their adsorption onto a solid surface allows to use their unique physical properties and results in large variety of potential applications. The possibility to arrange microgels of various compositions into one- and two-dimensional arrays inspires a series of technological applications in the field of soft nanotechnology utilizing their stimuli-responsive behaviour. Some examples aim at the use of the adsorbed microgels in biotechnological and medical applications[19–21]. Here, the search for stimuli-responsive and biocompatible host and carrier media for a dedicated and controlled drug release on demand is underway. Such coatings could also improve performance of implants such as neural electrodes[61]. Surfaces coated with PNIPAM are promising for the controlled adjustment of cell adhesion. It allows cell growth with high cell densities and prevents a post-transplantation inflammation[62]. Such surfaces permit the adhesion/detachment of the cell culture by a simple temperature switch[63–65]. Microgels in combination with metal nanoparticles are explored as building blocks for optical devices in nanooptics[15,23,46,66,67].

One pathway for the preparation of such surface structures is a controlled lateral arrangement of the PNIPAM microgels at solid surfaces. The lateral arrangement of the microgels in a surface layer depends on substrate properties, particle deposition technique, solvent quality and microgel properties[68,69]. The deposition of the microgels onto a solid surface can be realised in different ways, e.g. spin-coating[70,71]. In this case the coating density can be tailored with variation of the rotation speed. An other way is the coating from the oil/water interface when microgels initially are dropped onto oil/water interface and then transferred on solid surface via submergence of the latter[72]. In this case initial application of the lateral pressure to the microgels on the oil/water interface allows to alter the coating density as well as microgel size.

The structure and the shape of the adsorbed microgel results from the competition between the entropy loss due to the confinement of the chains at the surface and the energy gain of the adsorbed monomers[73]. The maximal gain would be achieved if all free chains are adsorbed, but this would lead to the high penalty in elasticity[47]. Therefore, commonly adsorbed microgels show the typical fried-egg structure[74].

According to *Vilgis et al.*[73], the competition between capillarity characterized by a spreading parameter S, and elasticity characterized by the bulk shear modulus G defines a typical length scale of the gel deformation as:

$$l \propto S/G \tag{2.3}$$

Positive values of the spreading parameter S allows spreading of the polymer gel on surface. Further deformation to some extent and formation of the foot of extension (l) occur (Figure 2.6).

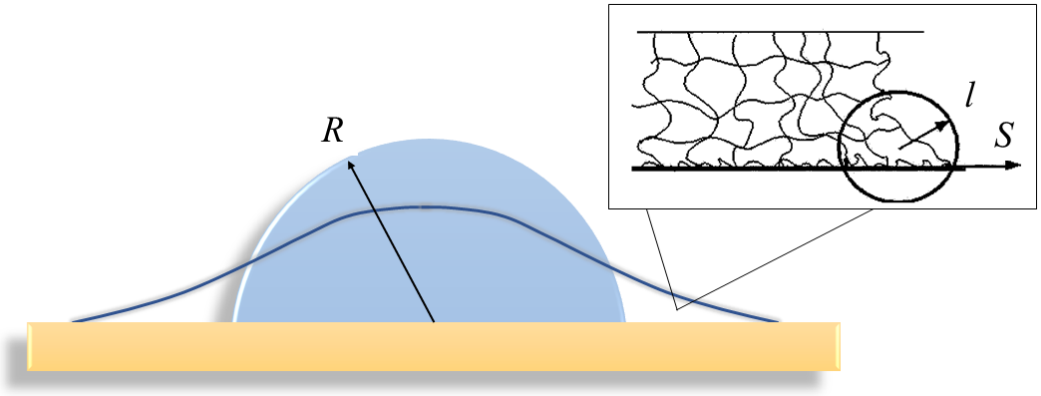

Figure 2.6: Deformation of the microgel shape due to adsorption: blue half-sphere – in contact with a non-adsorbing surface and solid line – in contact with well-adsorbing surface. The change in height and length is related to the scale l. Insert: The deformed region in the circle of radius l determines a microscopic extension for the local deformation in foot. Reproduced according to Ref.[73].

Gels larger than l deform mostly at their edges. Microgels smaller than l show deformation despite the elastic stresses. In this case strong adsorption overcomes the elasticity. Such behaviour was observed for the ultra-low crosslinked microgels[47].

The presence of the confining surface influences also the structure of the adsorbed poly(NIPAM-co-AAc) microgels[71]. The microgel volume decreases by about one order of magnitude during adsorption. An attractive interactions between network and surface leading to deformation and compression of the polymer network inside the adsorbed microgels were discussed as possible reasons for the stiffening in the adsorbed state[75].

For such investigations AFM or ellipsometry methods were used. They allow studies of the swelling behaviour, stiffens of the microgel and care only averaged (or any) information about internal polymer network structure of the adsorbed microgels. By *Schutle et al.*[26] the internal inhomogeneity inside adsorbed PNIPAM microgels by comparing core-shell and hollow microgels have been investigated by scanning force microscopy (SFM). However, sharp tips used in SFM technique can penetrate either deform the microgel, that leads to the incorrect characterisation of the microgel internal structure. The first try to demonstrate the inhomogeneous internal structure of the adsorbed PNIPAM microgel

was performed by *Matsui et al.*[76] by means of high-speed AFM. During the temperature increase, they observed a presence of domains of several tens of nanometer in size within the microgels.

The particular description of the scattering techniques is presented in Section 2.5, however, here should be noted, that scattering under grazing incidence conditions in contrast to the more classical transmission geometry overcomes the sample volume limitation and allows investigation of the small volume of the adsorbed sample. Combination of the grazing incidence geometry and the neutron scattering with the contrast variation using mixtures of D_2O and H_2O opens additional opportunities for the detailed investigation of the internal properties of the bio- and polymer structures[77–79]. Moreover, an illumination of the whole sample surface with a neutron beam yields a better statistical information compared to imaging techniques such as AFM, SFM etc.

Magerl et al.[80] investigated the influence of geometrical confinement on the chain conformation of cyclic PNIPAM in silicon-supported films by means of GISANS. They observed a preferential selection of stretched PNIPAM ring conformations in thin films and a preferential orientation of macromolecules parallel to the film interfaces with the substrate and air.

The temperature dependences of the correlation length of network fluctuations in weakly negatively charged poly-(NIPAM-co-AAc) microgels adsorbed onto positively charged silicon substrate surface were studied by *Wellert et al.*[75]. The analysis of the temperature-dependent GISANS measurements shows a decrease in the specular peak intensity which corresponds to the volume phase transition in the adsorbed state, while the lateral correlation length does not change with temperature. Comparison of results in the bulk and adsorbed state revealed that the solid substrate significantly effects the temperature-dependent behaviour and leads to the suppression of the divergence of internal fluctuations in the adsorbed microgels.

2.1.3 Polymer dynamics

Dynamics of the polymers covers a wide time and length scale. In Figure 2.7 the possible type of polymer dynamics is presented. The associated length scale varies from the bond length of angstroms to the inter-chain distances of tens of angstroms. The plateau regime corresponds to the distances of 50 – 100 Å. In the flow regime the proper chain dimensions determine scale length[25].

Below the glass transition temperature (T_g) only small amplitude motions like vibrations and short rang rotations may be observed. At the T_g α-relaxation allowing the system flow becomes active. The time range of such relaxations covers more than ten orders of

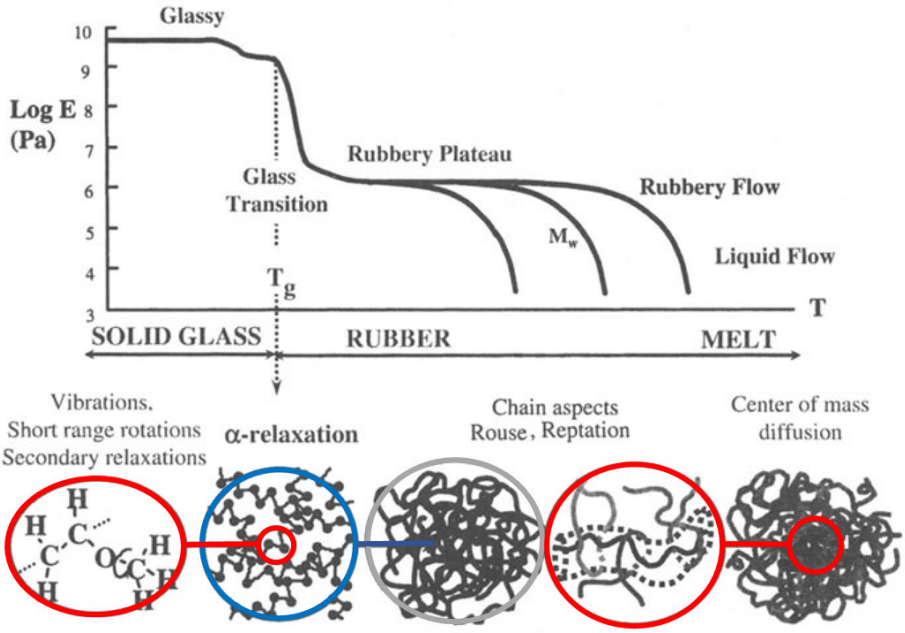

Figure 2.7: Variety of the polymer dynamics depending on the temperature. From Ref.[25].

magnitude. The length scale of the α-relaxation corresponds to the inter-chain distance of two polymer chains.

At the rubbery plateau the large scale motions within a polymer chain occur. Due to the mutually interpenetrated chains, the relaxation in this range is confined. In this case, the confinement effect is described in terms of a tube following the coarse grained chain profile. Motion is only allowed along the tube profile, therefore snake-like motions of the polymer or reptation process occurs.

When chains loss the memory of their initial state, the rubbery flow is observed. The rubbery flow passes over liquid flow, which is characterised by the chain translational diffusion coefficient[25].

Crosslinker distribution and internal microgel structure strongly influence the dynamics properties of the microgels[19,28,43,81].

Hellweg et al. reported on investigations of the dynamics of the macro- and microgels with low and medium crosslinker concentration. On a local scale differences in the network dynamics between microgels and macrogels prepared via surfactant-free emulsion polymerisation were found[82]. Moreover, it was shown, that the crosslinker concentration increase leads to the decrease of the collective diffusion coefficient of the microgels[3].

Richtering et al.[28] probed the dynamics of the responsive poly(*N*-isopropylacrylamide) (PNIPAM) and poly(*N,N*-diethylacrylamide) (PDEAAM) microgels in respect to their architecture and cononsolvency. It was found that in the collapsed state microgels behave

as solid diffusing objects with only very small additional contributions from the internal motions. In the swollen state PDEAAM microgels dynamics combines two regimes, namely Zimm segmental dynamics at the high momentum transfer and a collective diffusive motion for the smaller q-values were found.

The investigation of the internal dynamics of the feeding-microgels is still limited.

Zimm dynamics in polymer solution

The first successful model for the description of the conformational dynamics of an ideal chain was proposed by Prince E. Rouse in 1953[83] (known as *Rouse model*). Within the Rouse model polymer chains are considered as N beads connected by harmonic springs and committed to Brownian motion (Figure 2.8). The springs correspond to the entropic forces between the beads and the distance between the beads corresponds to the segment length of the polymer[84].

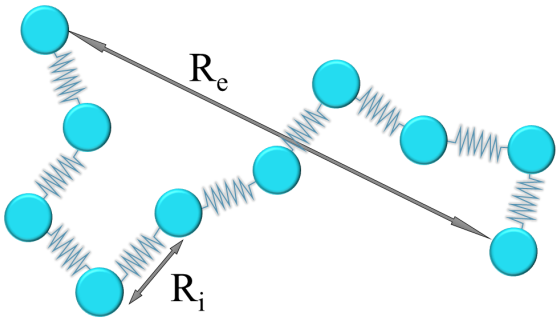

Figure 2.8: Polymer chain in the Rouse model: beads and springs correspond to the monomers connected via bonds. R_e correspond to the end-to-end distance, R_i is the segmental length

Significant observables of a polymer are the center of mass

$$\mathbf{R} = \frac{1}{N}\sum_{i=1}^{N}\mathbf{R_i} \tag{2.4}$$

the radius of gyration

$$R_g^2 = \frac{1}{N^2}\sum_{i=1}^{N}\langle(\mathbf{R_i} - \mathbf{R})^2\rangle \tag{2.5}$$

and the end to end distance[85]

$$R_e^2 = (\mathbf{R_n} - \mathbf{R_i})^2 \tag{2.6}$$

The thermally activated motion of the Rouse model can be described with a Langevin

equation in terms of a stochastic force (thermal fluctuations $f_n(t)$ with $< f_n(t) > = 0$), a friction force with friction coefficient ζ and the entropic force determine the relaxation of polymer chains as:

$$\zeta \frac{d\mathbf{R}_n}{dt} + \frac{3k_BT}{l^2}(\mathbf{R}_{n+1} - 2\mathbf{R}_n + \mathbf{R}_{n-1}) = f_n(t) \tag{2.7}$$

where k_B is the Boltzmann constant and T is the temperature.

Solution of the Langevin equation[85] leads to an expression for the mean square displacement as:

$$\langle(\mathbf{R}(t) - \mathbf{R}(0))^2\rangle = 6\frac{k_BT}{\zeta N}t \tag{2.8}$$

From the mean square displacement the diffusion coefficient can be computed as:

$$D = lim_{t\longrightarrow\infty}\frac{1}{6t}\langle(\mathbf{R}(t) - \mathbf{R}(0))^2\rangle = \frac{k_BT}{\zeta N} \tag{2.9}$$

The Rouse model takes into account an interaction of the beads through the connecting springs only. Therefore, the dynamics of the short polymer chains in the melt can be described with the Rouse model, while for the polymer solution, where hydrodynamic interaction is important, the Rouse model needs to be extended. The hydrodynamic interaction forces are a long-range and act on solvent via the particles motion in the solvent[86]. To consider a hydrodynamic interaction between monomers in polymer chain and between monomers and solvent, *Zimm model* was proposed[87]. This model accounts for the forces exerted on other chain segments by a moving segment of the same chain via the induced motion of the surrounding fluid.

Analogous to the Rouse model, the Langevin equation for the Zimm model can be presented as[84]:

$$\zeta \frac{d\mathbf{R}_n}{dt} = \sum_m H_{nm}\frac{k_BT}{l^2}\frac{\partial R_m}{\partial m^2} + \mathbf{f}_n(t) \tag{2.10}$$

The hydrodynamic interaction is presented here by Oseen tensor H_{nm}.

After solution of Eq. 2.10 the expression for the diffusion coefficient becomes:

$$D = \frac{k_BT}{\eta_s N^\nu b} \tag{2.11}$$

The exponent ν is called Flory exponent, η_s is solvent viscosity.

Comparison of the Zimm and the Rouse models reveals the difference in the accounted motions. While in Rouse model the chain in dilute solution can move a distance of the order of its size and diffusion coefficient is proportional to N^{-1}, in Zimm model

the hydrodynamic interactions is taken into account by means of the Oseen matrix, the diffusion coefficient depends on solvent viscosity and scales with $D \propto N^{-\nu}$, where $\nu<1$ depends on the boundary conditions[85]. In dilute solution the Zimm motion has less friction than the Rouse motion, and thus Zimm motion is faster[84].

The long time limits of Eq. 2.11 represents the global diffusion of a Gaussian polymer chain in the Zimm model. At shorter times, segmental (internal) motion is described by Eq. 2.10. The correlation function as measured with NSE and GINSES for this regime is described in Section 2.2.3. Segmental dynamics of microgels involves some modifications, the relevant length scale is the length between cross-links instead of R_e, and the apparent viscosity may differ from the pure solvent viscosity.

Dynamics of thin polymer films

The internal dynamics as well as structure of the adsorbed thin polymer films can not be achieved via classical transmission experiments. Dynamics investigation with most techniques gives only indirect access to the dynamics of the adsorbed systems. In scanning-force microscopy thermally activated cantiliver is used to probe polymer film dynamics at the surface. Here, excitation energies of a few k_BT generate excitation amplitudes of a few Å. In this way, the dynamical response of the neutral polymer and polyelectrolyte brushes on the environment variation were probed[88,89].

Application of neutron scattering for the dynamics investigation of the adsorbed polymer systems in combination with the grazing incidence geometry give a direct access to their internal dynamics. *Jaksch et al.*[90] give the recent overview of the neutron GIS for the in-situ and in-operando investigation in the soft matter and biophysics.

Gawlitza et al.[91] probed the internal dynamics of the adsorbed ethylene glycol based microgels at silicon surface by means of GINSES. The slowing down of the inner dynamics in the vicinity to the surface compared to the bulk behaviour was found. However, at increase of the distance from surface a bulk-like relaxation was observed.

Frielinghaus et al.[92] probed dynamics of microemulsion adjacent to a planar hydrophilic surface with GINSES. The depth dependent investigation of the near surface dynamics with such technique allows to obtain that the dynamics of an induced lamellar microemulsion to be three times faster compared to the bicontinuous bulk structure.

Dynamic membrane properties of phospholipid membranes close to silicon interface was studied by *Jaksch et al.*[93]. The local interaction and friction parameters were measured with GINSES. Author found an excitation mode of the phospholipid membrane that has not been reported previously and only became visible using the combination of grazing incidence geometry with neutron spin-echo spectroscopy.

Nylander et al.[94] also used GINSES for the investigation of the dynamics of nanostructure films formed by mixtures of soy phosphatidylcholine and glycerol dioleate at the silicon-aqueous interface. They showed direct influence of the structural phase on the dynamics properties. It was observed, that the cubic phase from the spin-coated film provides a very rigid layer at the substrate interface, whereas the hexagonal spin-coated phase is much more mobile and flexible. The presence of the rigid interface modified the undulations of the investigated film, so that it becomes similar to a flat membrane close to a wall.

All in all, GINSES is unique technique giving access to the thermal fluctuation close to the interface, and can be applied to a wide class of polymer- and bio-systems. However, due to novelty and complexity of the method, further improvement of the experimental conditions and further data treatment are needed.

2.2 Structure and dynamics investigation

In order to investigate dynamics and structure of the polymer microgels different methods were applied. Thus comprises most importantly the scattering techniques such as small-angle neutron and X-ray scattering (SANS/SAXS), neutron reflectometry (NR), neutron spin-echo (NSE) spectroscopy, grazing incidence small-angle neutron scattering (GISANS), grazing incidence neutron spin-echo spectroscopy (GINSES), dynamic light scattering (DLS) and atomic force microscopy (AFM). While with light scattering and AFM the microgel shape and outer dimensions were probed, with neutron scattering the internal structure and the polymer chains dynamics within one microgel were investigated. The current chapter is devoted to the brief description of the basic principles of the scattering and imaging techniques. The chapter is based on Ref.[25,95–98].

2.2.1 Basic principles of the scattering

The general principle of the scattering independent of the scatterer source (neutron, X-ray or light) is presented in Figure 2.9 and based on the momentum transfer $\hbar q$ and the energy transfer $\hbar\omega$:

$$\mathbf{q} = \mathbf{k_i} - \mathbf{k_f} \tag{2.12}$$

$$\hbar\omega = E_i - E_f \tag{2.13}$$

where $\mathbf{q}$ is the scattering vector with $\mathbf{k_i}$ and $\mathbf{k_f}$ being the wavevector of the incoming and scattered beams respectively.

Radiation incident on a sample, partially passes it non-affected, whereas another part is scattered. The intensity of the scattered signal $I(q,\omega)$ is measured then by detector at

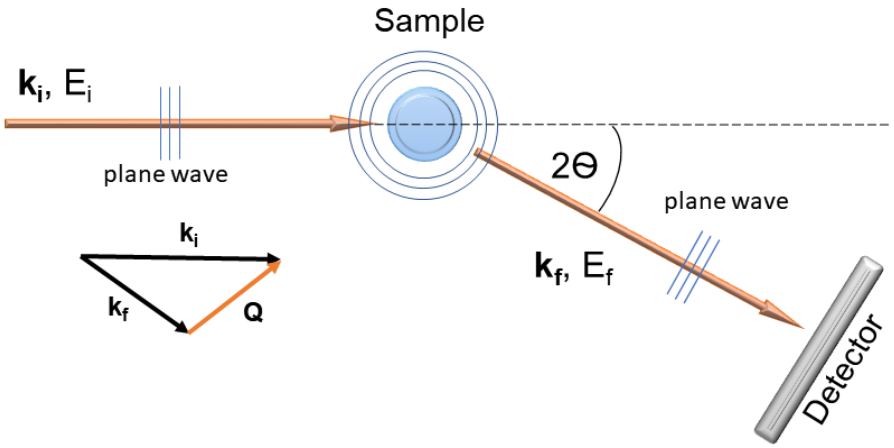

Figure 2.9: Scattering process with the waves characterized by wavevector $\mathbf{k_i}$ (incoming) and $\mathbf{k_f}$ (diffracted) and scattering vector $\mathbf{q}$.

scattering angle 2θ.

In case of elastic scattering, energy loss or gain are considered as 0, and scattering function becomes energy-independent $I(q, \omega = 0) = I(q)$, as for SANS/SAXS. However energy change is crucial for NSE techniques and inelastic scattering should be accounted for. Details of each scattering method are further described in corresponding section.

2.2.2 Neutron and X-ray small-angle scattering

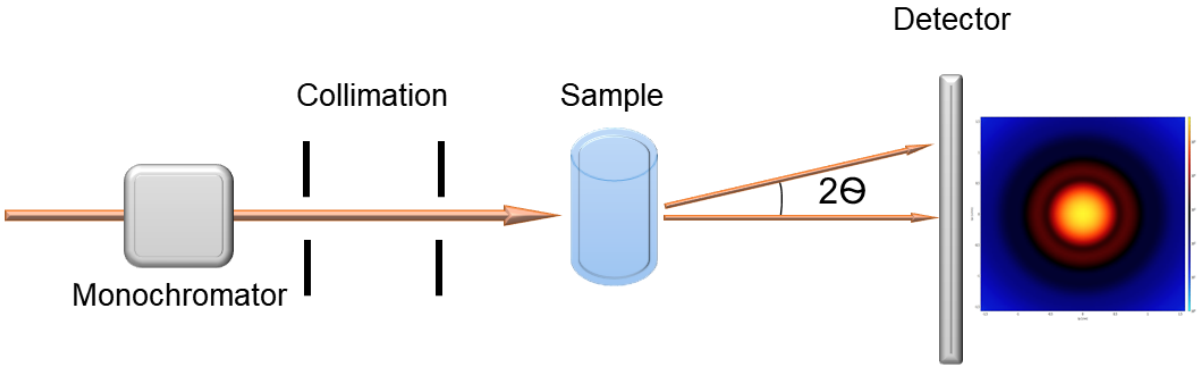

Figure 2.10: Principal scheme of the small-angle scattering experiment.

The typical scheme of small-angle scattering experiment is presented in Figure 2.10. A monochromator or wavelength selector determines the wavelength of the incident neutrons. In order to measure the scattered intensity at very low angles, the angular divergence of

the beam has to be minimized, which is achieved by collimation of the incoming beam. Optimal conditions in terms of resolution and intensity are achieved when collimation and detector distances are the same. For this reason, small-angle instruments have a long flight path, with detector and collimation distances reaching 20 m each for many SANS instruments. In order to cover a large momentum transfer range, measurements are usually performed at several detector distances[99].

Since the neutrons interact with the nuclei and the X-ray with the electron cloud of the atoms, the neutron scattering has an advantage over the X-ray scattering due to non-regular dependence of the neutron scattering cross-section across the periodic table and among the isotopes (see Figure 2.11). This is used to advantage in deuterium labelling using the fact that the scattering lengths for hydrogen and deuterium are widely different (b_H = -3.739·10^{-13} cm and b_D = 6.671·10^{-13} cm respectively)[100]. The neutron is quite sensitive to light atoms like hydrogen, oxygen, etc. which have much higher interaction probability with neutrons than with X-rays. The neutron scattering is a powerful technique for studying objects like polymer microgels, brushes or microemulsions and therefore is the key techniques of the current work. But also SAXS, which has better wavelength-resolution in probed q-range, was applied. The further description concerns mainly the neutron scattering, however the principles are applicable to X-ray scattering with different contrast conditions.

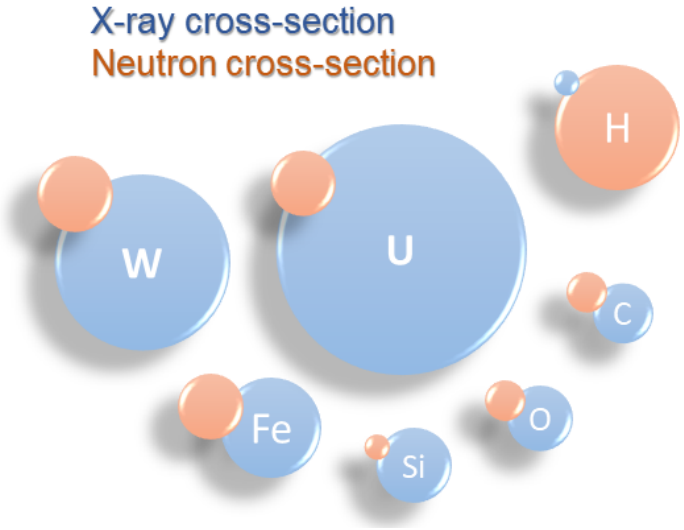

Figure 2.11: Neutron and X-ray scattering cross-sections compared for several elements. Ratio of spheres size schematically illustrate ratio of scattering cross-section of different elements in X-ray (blue) and neutron (orange) scattering.

In SAS the nucleus is considered as rigidly fixed at the origin of coordinates and energy change in the scattering process is neglected. In this case the scattering depends upon the

interaction potential $\mathbf{V}(\mathbf{r})$ between the neutron and the nucleus, where $\mathbf{r}$ is the distance between them. This potential is very short range and falls rapidly to zero at a distance of the order of 10^{-15} m. This value is much shorter than the neutron wavelength which is of the order of several Å for the described techniques and as a result the nucleus acts as a point scatterer.

The incident neutron beam can be described as plane wave with a wavefunction:

$$\Psi_i = exp(ikz) \tag{2.14}$$

where z is the distance from the nucleus in the propagation direction and $k = 2\pi/\lambda$ is the wavenumber of the neutrons with a wavelength λ. The scattered wave will then be spherically symmetric (as a result of the nucleus being a point scatterer) with a wavefunction:

$$\Psi_s = -\frac{b}{r}\, exp(ikr) \tag{2.15}$$

or in three-dimensional representation:

$$\Psi_s = -\sum_j \left(\frac{b_j}{r}\right)\ exp\ (ikr + i\mathbf{qr}) \tag{2.16}$$

where $r = |\mathbf{r}|$ – the radius around scattering centre, b is the scattering length. The magnitude of the scattering vector can be calculated from scattering angle 2Θ and wavelength λ as:

$$q = |\mathbf{q}| = \sqrt{k_i^2 + k_f^2 - 2k_i k_f cos2\Theta} => q = \frac{4\pi}{\lambda} sin\Theta \tag{2.17}$$

Usually investigations of the polymer systems by means of small-angle scattering (SAS) are concentrated on the length scales that are much large than inter-atomic distances, thus materials of interest can be represented in terms of the scattering length density:

$$\rho(r) = \sum_i b_i\ \delta(\mathbf{r} - \mathbf{r_i}) \tag{2.18}$$

or

$$\rho = \frac{\sum_i^n b_i}{\overline{V}} \tag{2.19}$$

where ρ is the scattering length density, $\overline{V}$ is the volume containing the n atoms and b_i is the scattering length of the i-th atom. This value depends on the strength of the interaction between neutron and a given nucleus (see Figure 2.11). The values of b_i are well known for each element and isotope, see e.g. *Sears*[101]. In case of X-rays, the scattering

arises from the interaction between the incident wave and the electron cloud of an atom in the material. Hence, the X-ray scattering length density is:

$$\rho_X = \frac{\sum_i Z r_e}{V_m} \tag{2.20}$$

where $r_e = 2.85 \cdot 10^{-5}$ Å is the radius of electron, Z is the atomic number, V_m is a molecular volume[102].

The integral of the scattering length density distribution across the whole sample normalized by the sample volume is presented by Rayleigh-Gans equation and represents small-angle scattering as a result of inhomogeneities in scattering length density (ρ(r)):

$$\frac{d\Sigma}{d\Omega}(\mathbf{q}) = \frac{N}{V}\frac{d\sigma}{d\Omega}(\mathbf{q}) = \frac{1}{V}\left[\int_V \rho(\mathbf{r}) exp(i\mathbf{qr}) d\mathbf{r}\right]^2 \tag{2.21}$$

The differential cross section $d\sigma/d\Omega$ sets the probability that neutrons fly out of the sample at a certain angle Ω in the solid angle element $d\Omega$ and is the directly measured quantity in a scattering experiment. The integral term is the Fourier transform of the scattering length density distribution and the differential cross section is proportional to the square of its amplitude. This latter fact means that all phase information is lost and we cannot simply perform the inverse Fourier transform to restore the scattering length density distribution back from the macroscopic cross section.

In case of elastic neutron scattering (the energy loss is neglected) on non-magnetic systems the scattering cross-section can be represented as a sum:

$$\frac{d\Sigma}{d\Omega}(\mathbf{q}) = \frac{d\Sigma_{coh}}{d\Omega}(\mathbf{q}) + \frac{d\Sigma_{inc}}{d\Omega}(\mathbf{q}) + \frac{d\Sigma_{abs}}{d\Omega}(\mathbf{q}) \tag{2.22}$$

or

$$I(\mathbf{q}) = I_{coh}(\mathbf{q}) + I_{inc} + I_{abs}(\mathbf{q}) \tag{2.23}$$

Information about the distribution of matter in the sample is contained in the coherent component (I_{coh}). It describes the scattering of a single neutron from all the nuclei in a sample. The incoherent component (I_{inc}) is q-independent and involves correlation between the position of an atom at time 0 and the same atom at time t. The incoherent scattering is isotropic and in small-angle scattering experiment thus contributes to the background signal. The absorption component (I_{abs}) for neutrons is usually small and simply reduces the overall signal, while for X-ray scattering absorptions may significantly reduce the scattering signal and must be taken into account.

To analyse small-angle scattering data model-dependent and model-independent ap-

proaches are applied. The first consists of building a mathematical model of the scattering length density distribution, whilst the second consist of direct analysis of the scattering data to yield useful information.

Guinier analysis

Depending on the sample size, additional scattering contribution, size distribution, there may not always the clear scattering shape can be achieved. However some information about scattering object can be drawn from the model free analysis. When the probed range ($2\pi/q$) is larger than the scattering object size, the radius of gyration R_g of the non-interacting particles can be obtained from the Guinier analysis:

$$I(q) = I_0 exp\left(-\frac{q^2 R_g^2}{3}\right) \tag{2.24}$$

The range of a Guinier plot corresponds to $qR_g < \sqrt{3}$. The radius of gyration represents the effective size of the scattering "particle" whether it is a polymer chain, part of a protein, a micelle, or a domain in a multiphase system[100]. The radius of gyration is not equal to the spherical particle radius, but can be calculated for many simple bodies as given in Table 2.1[103].

Table 2.1: Radii of gyration of some common polymer architectures and solid objects.

Object	R_g^2
Linear chain	$Nb^2/6$
Rings	$Nb^2/12$
Sphere	$3R^2/5$
Disk	$R^2/2$

Porod law

In double logarithmic plot the spherical factor in high q-range has a slope of -4. It was shown by *Porod*[104] and is known as Porod low. In this case intensive forward scattering from polymer rich aggregates formed above VPTT dominates and direct estimation of the microgel radius is not possible. Porod law gives the characteristic q^{-4} behaviour at high q:

$$I_P(q) = \frac{I_0}{q^4} = \frac{2\pi(\Delta\rho)^2(S/V)}{q^4} \tag{2.25}$$

where $\Delta\rho$ is the contrast between the two phases (i.e. aggregates and solvent) and S/V is the specific surface of the particles.

While Eq. 2.25 is introduced for the particle with the smooth surface only, in this thesis the general power low with variable parameter α was applied:

$$I_P(q) = \frac{I_0}{q^\alpha} \tag{2.26}$$

In Figure 2.12 the different polymer networks at variables α are presented. For example, a slope of $\alpha = 2$ signatures a Gaussian chains in a dilute environment, a slope of 5/3 is for swollen coils[100].

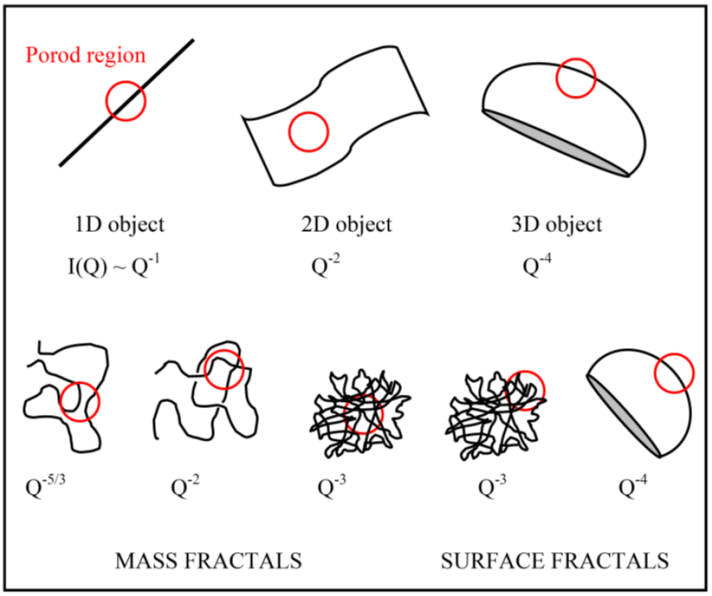

Figure 2.12: Porod low for different shape objects. From Ref.[100].

Internal inhomogeneity

Based on the Panyukov-Rabin theory presented in Section 2.1, the Fourier conjugates of $\rho^{th}(r)$ and $\rho^{eq}(r)$ gives thermal and frozen structure factors, $G(q)$ and $C(q)$, as:

$$\begin{aligned} G(q) &= \langle \rho^{th}(r)\rho^{th}(-r)\rangle, \\ C(q) &= \langle \rho^{eq}(r)\rho^{eq}(-r)\rangle \end{aligned} \tag{2.27}$$

The scattering profile of the microgels in the swollen state can be described by a sum of both structure factors[48]:

$$S(q) = C(q) + G(q)$$

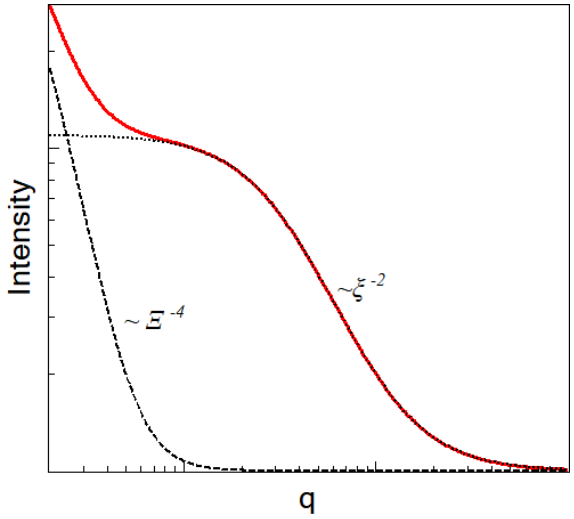

Figure 2.13: Spectrum according to the Ornstein-Zernike (dotted line) and Debye-Bueche (dashed line) functions. Red spectra corresponds to the sum of both functions.

According to *Bastide and Leibler*[36] *G(q)* and *C(q)* can be presented as the Ornstein-Zernike and Debye-Bueche functions (2.28). The first one represents thermal fluctuations on a very local scale of polymer chain segments in the present case inside the microgel and contributes to the higher q-range, while the second one describes the frozen inhomogeneities[35], which are detectable at smaller q (Figure 2.13):

$$G(q) \propto I_{OZ}(q) = \frac{I_{OZ}(0)}{1+\xi^2 q^2}$$

$$C(q) \propto I_{DB}(q) = \frac{I_{DB}(0)}{(1+\Xi^2 q^2)^2}$$

$$I_{inh}(q) = \frac{I_{OZ}}{1+\xi^2 q^2} + \frac{I_{DB}}{(1+\Xi^2 q^2)^2} + I_{inc} \tag{2.28}$$

where ξ is the correlation length, Ξ is the characteristics size of the inhomogeneities, I_{OZ} and I_{DB} are the scattering signals from the thermal fluctuations and frozen inhomogeneities at $q = 0$, I_{inc} takes into account incoherent scattering.

Scattering from spherical particles

The coherent scattering cross section for small-angle scattering can be written as:

$$I(q) = \frac{d\Sigma}{d\Omega}(q) = n\Delta\rho^2 P(q) S(q) \tag{2.29}$$

where n is the number density of particles, $\Delta\rho = (\rho_{solvent} - \rho_{particle})$ is the scattering contrast between the particle ($\rho_{particle}$) and the solvent ($\rho_{solvent}$) scattering length density, $P(q)$ is the particle form factor, and $S(q)$ is the structure factor[105]. The particle form factor describes the morphology of the individual particles and fulfills the condition of $P(0) = V^2$ with V being the particle volume.

The form factor of a given particle is the square of its scattering amplitude which can generally be derived by the Fourier transform of the radial density distribution as:

$$P(\mathbf{q}) = F^2(\mathbf{q}) = \left| \int \rho(\mathbf{r}) exp(i\mathbf{qr}) d\mathbf{r} \right|^2 \tag{2.30}$$

For a **homogeneous spherical particle** with density ρ at $r < R$, the scattering amplitude $F(q)$ is[105]:

$$F_{sphere}(q) = 4\pi \int_0^R \frac{sin(qr)}{q} r dr = \frac{4}{3}\pi R^3 \frac{3\left[sin(qR) - qRcos(qR)\right]}{(qR)^3} \tag{2.31}$$

Spectrum of the $F_{sphere}(q)$ is presented in Figure 2.14.

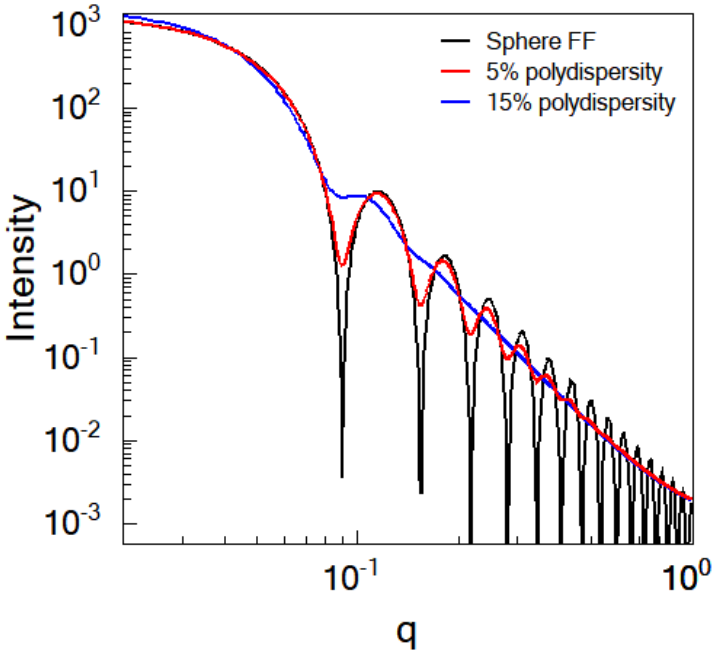

Figure 2.14: Form-factor of homogeneous sphere with respect to polydispersity of sphere radius: black line – scattering on the identical spheres, red line – 5% polydispersity, blue line – 15% polydispersity.

The structure factor provides information on the interaction between the particles and the resulting interference of the scattering from the different particles. For very dilute

dispersions of non-interacting particles, the structure factor approaches 1 and can be neglected, how was done for the batch-microgels in current work. In case of the feeding-microgels correlation of the internal spherical domains significantly influences scattering signal, therefore according to *Teixeira*[106] it was taken into account as presented in Eq. 2.32.

$$S(q) = 1 + \frac{D_f \Gamma(D_f - 1)}{\left[1 + \frac{1}{(ql)^2}\right]^{(D_f-1)/2}} \frac{sin\left[(D_f - 1)tan^{-1}(ql)\right]}{(qr')^{D_f}} \tag{2.32}$$

where l is the correlation length representing the cluster size, $V_{particle} = \frac{4}{3}\pi r'^3$ and D_f is the fractal dimension, representing the self-similarity of the structure.

Size distribution

The expression for the scattering cross section given in equation 2.29 is based on the assumption of monodisperse objects. However, because real samples always exhibit a varying degree of size dispersion, the particle size distribution has to be taken into account. This is achieved by weighting the scattering cross section of non-interacting nanoparticles with a size distribution function $D(r, r_0, \sigma)$:

$$\frac{d\Sigma(q)}{d\Omega} = n\Delta\rho^2 \int P(q, r) D(r, r_0, \sigma) dr \tag{2.33}$$

Figure 2.14 demonstrates an influence of the size distribution on the scattering spectrum of the homogeneous spheres (spectra with polydispersity of 5% and 15% are shown).

SAS instrumental resolution

Next to the particle size distribution, the instrumental q-resolution is another parameter resulting, for instance, in smearing of the form factor minima. In order to get reliable information on particle size and size distribution, the instrumental resolution has to be calculated carefully and implemented into the scattering cross section model. An expression for the q-resolution of small-angle scattering instrument[105] is:

$$dq = \sqrt{\left(\frac{4\pi}{\lambda}\right)^2 d\theta^2 + q^2 \left(\frac{d\lambda}{\lambda}\right)^2} \tag{2.34}$$

q-resolution can be implemented into a scattering model by smearing the scattering intensity with a Gaussian function representing instrumental resolution[107].

$$\frac{d\Sigma(q)}{d\Omega} = n\Delta\rho^2 \int P(q, r) q_{res}(q, q_0, \sigma_q) dq \tag{2.35}$$

with

$$q_{res}(q, q_0, \sigma_q) = \frac{1}{\sqrt{2\pi}\sigma_q} exp\left(-\frac{(q-q_0)^2}{2\sigma_q^2}\right) \tag{2.36}$$

2.2.3 Neutron reflectivity and scattering under grazing incidence

Due to the adsorption of the polymer microgels onto solid surface, systems undergo structural changes. Moreover, adsorption process leads to the formation of the thin polymer layers with height up to a few hundreds of nm. Investigation of such systems becomes a challenging task. Due to a much smaller scattering volume, transmission geometry of the scattering experiment is not favourable anymore, nevertheless investigation of the polymer films by means of neutron reflectometry (NR) and scattering under grazing incidence (GISAS) allows to probe their surfaces and interfaces in 3 dimensions, namely normal to the surface and in plane[108]. In this case, the well collimated incident neutron beam impinges the sample at small, well-defined angle. It is then partly refracted into material and partly reflected speculary from the surface, i.e. the outgoing angle α_f is equal to the incident angle α_i[109].

In real experimental conditions and due to the imperfection of the real surfaces and interfaces, pure total reflection does not exists (see Figure 2.15). Therefore specular reflection is always accompanied by the off-specular or diffuse scattering at $\alpha_f \neq \alpha_i$[110].

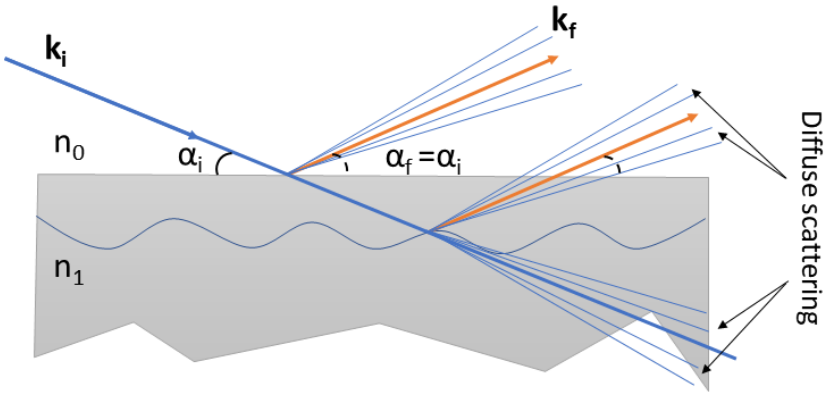

Figure 2.15: Specular and off-specular scattering from a rough interface.

Figure 2.16 presents a general scheme of the GISAS experiment. Here incident radiation impinges system under investigation at shallow incident angle α_i ($< 1°$) with a wavevector $\mathbf{k}_i$ and scattered intensity with wavevector $\mathbf{k}_f$ is detected with a position sensitive detector as a function of scattering (α_f) and out-of-plane (ψ) angles.

In this representation the sample surface is defined as (x, y) plane with the neutron beam being parallel to the x-axis, and the scattering plane is defined by the (y, z) plane[112].

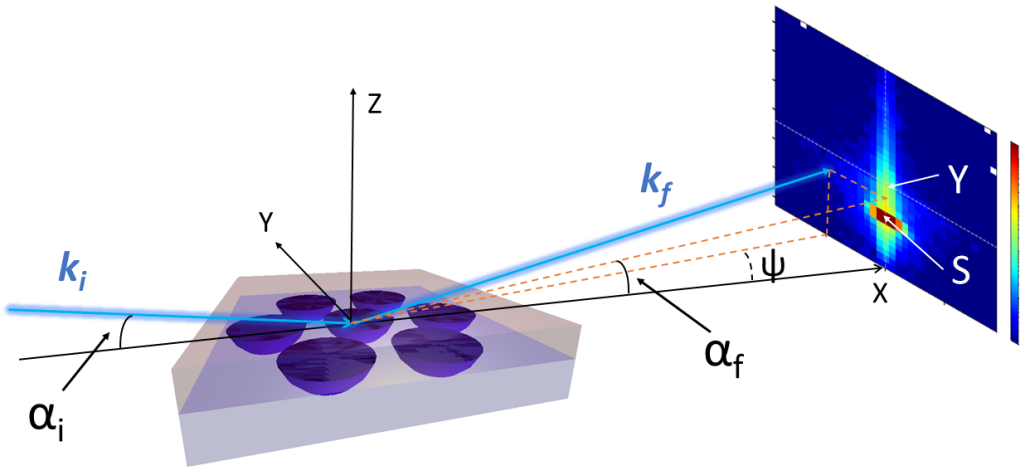

Figure 2.16: Schematic illustration of the scattering geometry under grazing incidence conditions. α_i is incident angle of the neutron beam with incident wave vector $\boldsymbol{k_i}$. A two-dimensional detector is used to measure the specular (S) and diffuse scattering (with wave vector $\boldsymbol{k_f}$) intensity as a function of exit angle α_f and the out-of-plane angle ψ. The horizontal line cut performed at the position of the Yoneda peak (Y) was used for data analysis (from Ref.[111]).

Thus, the scattering vector $\mathbf{q} = \mathbf{k}_f$ - $\mathbf{k}_i$ has following components[108]:

$$\begin{aligned} q_x &= \frac{2\pi}{\lambda}(cos(\psi)cos(\alpha_f) - cos(\alpha_i)) \\ q_y &= \frac{2\pi}{\lambda}sin(\psi)cos(\alpha_f) \\ q_z &= \frac{2\pi}{\lambda}(sin(\alpha_i) + sin(\alpha_f)) \end{aligned} \tag{2.37}$$

The q_y component is oriented parallel to the sample surface and probes lateral structure in GISAS experiment. The characteristic diffuse scattering feature, so-called Yoneda peak[113], appears when the incident angle of the beam is equal to the critical angle of the material, $\alpha_i = \alpha_c$. The Yoneda cut performed at the position of Yoneda peak gives the information on correlations in the lateral density distribution, mainly the average inter-particle distance, the size and the shape of the nanostructures respectively in the near surface regime[114]. If the incident angle α_i is larger than the critical angle α_c of the material, the beam penetrates fully the thin film. A specular reflectivity experiment measures the scattered intensity as a function of $q_z = 2k_z$. As such, the reflectometry experiment provides information about structure perpendicular to the interface. In next two sections specular reflectivity as well as GIS are described more in details.

Specular reflectivity

For the perfect surface a description of the specular reflection can be deduced from quantum theory[99]. The Schrödinger equation for the wave function can be presented in the form:

$$\left[-\frac{\hbar}{2m}\Delta + V(\mathbf{r})\right]\Psi = E\Psi \tag{2.38}$$

where $E = \hbar^2 k^2/2m$ is the energy of the neutrons with the modulus $k = 2\pi/\lambda$ of the wave vector $\mathbf{k}$ and $V(\mathbf{r})$ is a potential. Taking into account experimental conditions of the reflectometry experiment (atomic structure are not resolved), potential V of the homogeneous medium can be presented as a sum of the scattering length densities of all components:

$$V = \frac{2\pi\hbar}{m}Nb \tag{2.39}$$

where N is the atomic number density, b is the coherent scattering amplitude of the bound atom (also called scattering length) and Nb is the neutron scattering length density (SLD). Thus, Eq. 2.38 reduces to:

$$\left[\Delta + k'^2\right]\Psi = 0 \tag{2.40}$$

with index of refraction $n = k'/k$, where k', k are the neutron wave vectors inside and outside the medium. The refractive index of a material against vacuum is commonly written as[98]:

$$n = 1 - \delta + i\mu \tag{2.41}$$

where $\delta = Nb\lambda^2/2\pi$ and $\mu = N\alpha_a\lambda/4\pi$ is a neutron absorption with α_a being the absorption cross-section. μ can be ignored for most materials. Also in most cases $n<1$ and neutrons exhibit an external reflection with Snell's law giving the critical angle below which the total reflection occurs as:

$$cos\theta_c = \frac{n_1}{n_0} \tag{2.42}$$

For neutrons incident on the surface of a material (e.g. water or silicon) from air (which has a refractive index very close to 1) we can obtain a simple relationship between the critical angle, neutron wavelength and scattering length density of the material:

$$\theta_c = \lambda\sqrt{\frac{\rho}{\pi}} \tag{2.43}$$

The reflectivity is given by Fresnel's law where for $\theta \leq \theta_c$ the reflectivity $R = 1$ and for

$\theta \geq \theta_c$:

$$R = |r|^2 = \left| \frac{n_0 sin\theta_0 - n_1 sin\theta_1}{n_0 sin\theta_0 + n_1 sin\theta_1} \right| \tag{2.44}$$

The Fresnel calculation can be extended for the case of a thin film at the interface (Figure 2.15). A beam incident on such a system will be multiply reflected and refracted at the interfaces between the layers. Taking into account the phase changes that occur, the reflection and refraction coefficients for each pair of adjoining media may be calculated by an infinite sum of amplitudes of the reflected and refracted rays. For a single thin film of thickness d this leads to an exact equation for the interference from the film:

$$R = |r|^2 = \left| \frac{r_{01} + r_{12} exp(2i\beta)}{1 + r_{01} r_{12} exp(2i\beta)} \right|^2 \tag{2.45}$$

where r_{ij} is the Fresnel reflection coefficient at interface ij given by

$$r_{ij} = \frac{p_i - p_j}{p_i + p_j} \tag{2.46}$$

with $p_j = n_j sin\theta_j$ and $\beta_j = (2\pi/\lambda) n_j d sin\theta_j$ (the optical path length in the film). This approach can be extended easily to three or four discrete layers, but beyond that level of complexity a more general solution is required. One such standard method is that described by *Born and Wolf*[115] where, on applying the condition that the wave functions and their gradients are continuous at each boundary, a characteristic matrix for each layer can be derived such that for the j-th layer:

$$M_j = \begin{bmatrix} cos(\beta_j) & -(1/p_j) sin(\beta_j) \\ -p_j sin(\beta_j) & cos(\beta_j) \end{bmatrix}$$

The resulting reflectivity is then obtained from the product of the characteristic matrices $M_R = [M_1][M_2]...[M_n]$:

$$R = \left| \frac{(M_{11} + M_{12} p_s) p_a - (M_{21} + M_{22}) p_s}{(M_{11} + M_{12} p_s) p_a + (M_{21} + M_{22}) p_s} \right| \tag{2.47}$$

where M_{ij} are the components of the 2×2 matrix M_R.

Whilst the above calculations are only strictly valid for smooth interfaces between actual physical layers of material, one can imagine description of a layer of varying scattering length density as a series of layers of various scattering length densities. In the limit of infinite number of layers this would converge to an exact description of the scattering length density profile normal to the interface and thus correctly determine the reflectivity.

This, in fact, is the way the matrix formalism is mostly used (though with a limited number of layers). Next, the question of smoothness needs to be addressed.

Roughness. Long range undulations, which can be considered locally flat, do not affect the above calculations. Here we consider deviations from a completely smooth interface that occur on length scales of the same order as the neutron wavelength. Such local roughness modifies the specular reflectivity in a manner similar to a diffuse (non-sharp) interface and in fact the two are indistinguishable in the specular reflectivity experiment. It can be shown that the presence of local roughness will modify the reflected intensity by a Debye-Waller factor as:

$$I(q) = I_0(q)exp(-q_0q_1 < \sigma >^2) \tag{2.48}$$

where $I(q)$ and $I_0(q)$ are the reflected intensity with and without surface roughness, $< \sigma >$ is the root mean square roughness and $q_i = 2ksin\theta_i$. The above result is only valid for bulk interfaces. However it can be extended to interfacial roughness and diffuse interfaces of thin films by applying a Gaussian roughness factor to the Fresnel coefficients of each interface such that:

$$r_{ij} = \left(\frac{p_i - p_j}{p_i + p_j}\right) exp\left(\frac{-q_iq_j < \sigma >^2}{2}\right) \tag{2.49}$$

Reflectometry instrumental resolution. To compute relative resolution in q following relations have been used:

$$\Delta q = \sqrt{\left(\frac{\partial q}{\partial \lambda} \cdot \Delta\lambda\right)^2 + \left(\frac{\partial q}{\partial \theta} \cdot \Delta\theta\right)^2} \tag{2.50}$$

where

$$q = \frac{4\pi}{\lambda} \cdot \sin\theta \approx \frac{4\pi\theta}{\lambda} \tag{2.51}$$

The derivatives are computed as

$$\frac{\partial q}{\partial \lambda} = \frac{4\pi\theta}{\lambda^2} \tag{2.52}$$

$$\frac{\partial q}{\partial \theta} = \frac{4\pi}{\lambda} \tag{2.53}$$

Thus,

$$\frac{\Delta q}{q} = \sqrt{\left(\frac{\Delta\lambda}{\lambda}\right)^2 + \left(\frac{\Delta\theta}{\theta}\right)^2} = \sqrt{0.1^2 + \left(\frac{3 \cdot 10^{-3} \cdot 4\pi}{q\lambda}\right)^2} \tag{2.54}$$

for $\lambda = 1$ nm, $\Delta\lambda = 0.1$ nm, and $\Delta\theta = 3 \cdot 10^{-3}$ rad.

The measured reflectivity depends on the scattering length density profile, ρ(z), perpendicular to the interface. Although the scattering length density profile is normally a continuously varying function, the interfacial structure can often be well approximated by a slab model in which layers of thickness (d_n), scattering length density (ρ_n) and roughness ($\sigma_{n,n+1}$) are sandwiched between two infinite sub-phases. One then uses a refinement procedure to minimise the differences between the theoretical and measured reflectivity curves, by changing the parameters that describe each layer[116].

Scattering under grazing incidence

In grazing incidence geometry correlation lengths, which correspond to the lateral fluctuations at the interface or of the densities inside the layers, are smaller than the projected coherence lengths and therefore multiple scattering processes within this surface occur (Figure 2.17). In this case, the Born approximation fails and a description within the framework of the Distorted Wave Born Approximation (DWBA), a first-order perturbation theory, is used to include strong dynamical effects from total external reflection[99,117,118].

In DWBA the potential in Eq. 2.38 can be presented as a sum of the reference potential V and residual potential $V'(\mathbf{r})$ describing the density fluctuation in lateral direction ($\mathbf{r}$):

$$V(\mathbf{r}) = V + V'(\mathbf{r}) \tag{2.55}$$

The first potential gives rise to the specular reflectivity (as described in "Specular reflectivity") and the second one to the diffuse scattering. The solution of the Schrödinger equation can be found elsewhere[99] and gives the diffuse scattering cross-section of an m-layer system as:

$$\left(\frac{d\sigma}{d\Omega}\right)_{diff} = \frac{C\pi^2}{\lambda^4} \sum_{j,k=1}^{m} \left(n_j^2 - n_{j+1}^2\right)\left(n_k^2 - n_{k+1}^2\right) \sum_{h,l=0}^{3} W_{h,j} W_{l,k} F_{j,k}^{h,l} \tag{2.56}$$

with the Fresnel transmissions coefficients $t_{i,f}$ and the Fresnel reflection coefficients $r_{f,j}$ entering directly in $W_{0,j} = t_{i,j}t_{f,j}$; $W_{1,j} = t_{i,j}r_{f,j}$; $W_{2,j} = r_{i,j}t_{f,j}$ and $W_{3,j} = r_{i,j}r_{f,j}$. C denotes the illuminated surface area and n_j denotes the refractive index of the j-th layer. The data cannot be fitted in a straightforward manner because of the q-dependence of the diffuse scattering factor $F_{j,k}^{h,l}$. The diffuse scattered intensity *I(**q**)* for the lateral density fluctuation on the surface can be expressed as[109]:

$$I(\mathbf{q}) \sim \langle [F_{DWBA}(\mathbf{q})]^2 \rangle S(\mathbf{q}_\parallel) \tag{2.57}$$

where $F_{DWBA}(\boldsymbol{q})$ is a DWBA form factor taking into account terms illustrated in Figure 2.17.

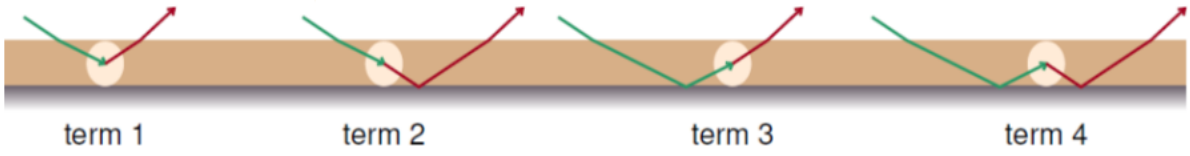

Figure 2.17: The four scattering terms in the Distorted Wave Born Approximation.

Interface sensitivity can be achieved by varying the incident angle in GISANS experiments. At the incidence angle α_i of the impinging neutron beam below the critical angle of total reflection α_c ($\alpha_c = \lambda\sqrt{Nb/\pi}$), a specular reflected beam occurs, i.e. all intensity is reflected and no wave propagation in z-direction exists in the sample. However inside the medium evanescent wave in z-direction with propagation parallel to the surface is induced. This "evanescent wave" arises as a real part of the solution of the Schrödinger equation at $\alpha < \alpha_c$ (mathematical description of the evanescent wave nature can be found elsewhere[119–121]). In the ideal case of perfectly flat interface the penetration depth defined as the depth at which the intensity is attenuated by $1/e$, while at α_i, $\alpha_c < 1$ the evanescent wave possesses exponentially decaying behaviour with the penetration depth following:

$$D = \frac{\lambda}{\sqrt{2}\pi(l_i + l_f)} \tag{2.58}$$

with

$$l_{i,f} = \left[\left(\alpha_c^2 - \alpha_{i,f}^2\right) + \sqrt{\left(\alpha_{i,f}^2 - \alpha_c^2\right) + 4\mu^2}\right] \tag{2.59}$$

where α_c is the angle of total reflection, α_i and α_f are the incident and scattering angle, respectively, μ is the imaginary part of the refractive index from Eq. 2.41.

When the neutron beam enters through a transparent substrate, such as silicon, D represents the distance from the Si-polymer interface into the probed system. Example of the penetration depth as a function of the incidence angle is presented in Figure 2.18.

Model applied to GISANS data analysis

In (GI) geometry, for the quantitative description of the structural information in the lateral direction the following function was used:

$$F(q) = Aexp\left(-\frac{(q - q_{max})^2}{2\sigma^2}\right) + \frac{I_{inh}}{(1 + \Xi_s^2 q^2)^2} + \frac{I_{oz}}{1 + \xi_s^2 q^2} + I_{inc} \tag{2.60}$$

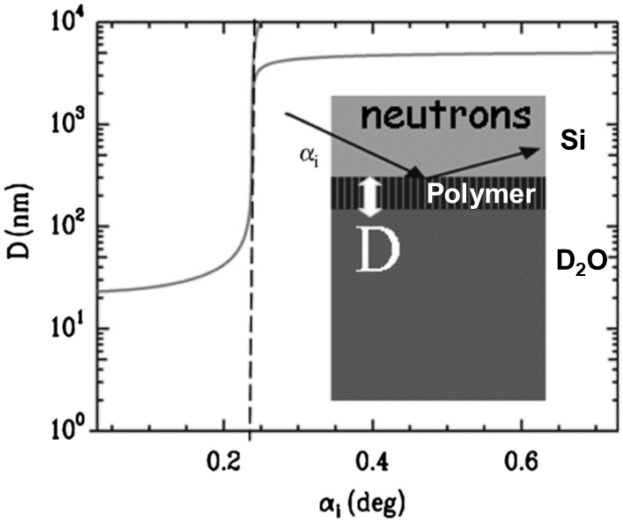

Figure 2.18: Scattering depth D as a function of the incident angle. Dashed line corresponds to α_c. Figure from Ref.[108].

where A is an amplitude, $q_{max} = 0$, σ represents the instrumental resolution, I_{inc} is the incoherent scattering background. The first term describes the experimental resolution function, second and third terms correspond to the Ornstein-Zetnike and the Debye-Bueche functions (analogously to SANS). Figure 2.19 depicts the contribution of each fitting component to the GISANS scattering spectrum.

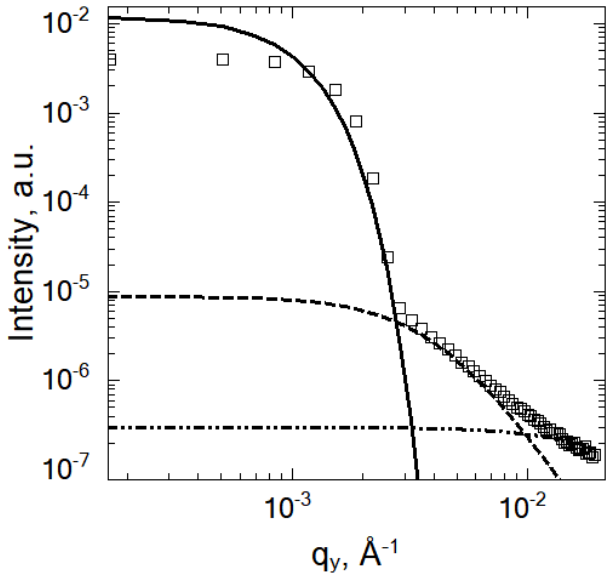

Figure 2.19: Contribution of the different terms in Eq. 2.60: the solid line corresponds to the Gaussian resolution part, dashed line to the Debye-Bueche function with $\Xi \approx 230$ Å and the dash-dotted line to the Ornstein-Zernike function ($\xi \approx 50$ Å).

The additional characterization of the lateral structure of the adsorbed polymer systems was supported with simulations using BornAgain software. Details are presented in Chapter 6.

2.2.4 Neutron spin-echo spectroscopy

In contrast to the previously reported techniques which give structure information, the dynamics of microgel systems was investigated by means of neutron spin echo (NSE) spectroscopy. NSE is, due to its high energy resolution, a well-suited method for studying slow dynamics, such as the dynamics of the soft matter systems (microemulsions, polymers and complex liquids)[122]. Neutron spin-echo spectrometers have the highest energy resolution of all types of the neutron spectrometers and allow analysis of slow motions (up to several 100 ns) on large and intermediate length scales.

An energy resolution necessary to observe processes at time scales of 100 ns and above requires the detection of relative neutron velocity changes in order of 10^{-5} to 10^{-4}, that lead to a significant intensity decrease of the incoming neutron beam (due to "filtering" of all neutrons with unwanted directions and velocities). To avoid such a problem, in NSE the velocity filter transmitting only one extremely narrow band is replaced by a filter with a cosine modulated transmission. A velocity increment $\Delta\nu_c$ of 10^{-5} between adjacent maxima and minima of such a filter enables the detection of a 10^{-5} velocity change without dramatical intensity reduction. The complete information on the distribution of velocity changes during scattering (the Fourier transform of the scattering function $S(q,\omega)$, i.e. the intermediate scattering function $S(q,t)$) is obtained by scanning a parameter that controls the period of the cosine filter[25].

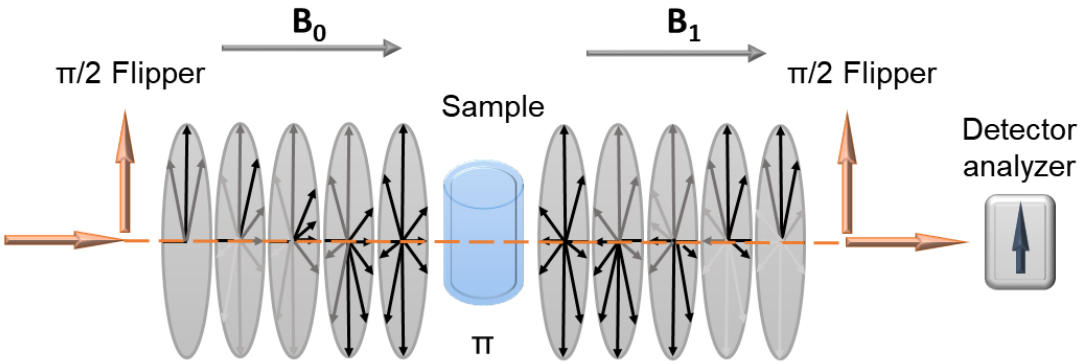

Figure 2.20: Principal scheme of neutron spin-echo instrument.

NSE spectroscopy is based on the neutron property, namely its spin, which orientation can be changed in a magnetic field. The basic principle of the NSE instrument invented by

Mezei[123] is presented in Figure 2.20. Measuring procedure consists of the following steps:

(1) $\pi/2$ **flip**: the neutron beam initially polarised parallel to the magnetic guiding field in the first flipper coil undergoes rotation of the neutron spin by 90° with respect to the guiding field. This $\pi/2$ flip initiates Larmor precession, which acts as a stop watch for each individual neutron.

(2) **Larmor precession**: inside a first magnetic field of variable strength the Larmor precession angle ϕ is proportional to the time the neutron spends traversing the field:

$$\phi = \gamma H l / v \tag{2.61}$$

where γ is the Larmor constant, H is the average strength of the magnetic field of length l between the $\pi/2$ flipper and the π flipper at the sample.

(3) π **flip**: neutrons undergo 180° turn around a properly chosen axis, i.e. the spin angle ϕ is transformed into $-\phi$ with respect to this axis.

(4) **Scattering on the sample** results in an energy change of the neutron with a probability described by the $S(q,\omega)$ dynamic structure factor of the sample. According to Eq. 2.12 the momentum transfer is:

$$\hbar\mathbf{q} = m\mathbf{v'} - m\mathbf{v} \tag{2.62}$$

(5) **Larmor precession in a second field** region will add another angle ϕ' to the apparent precession angle $-\phi$ up to the flipper at the sample. Measure of the neutron energy at the condition $Hl = H'l'$ and at small velocity changes gives:

$$-\phi + \phi' = \gamma H l \left(\frac{1}{v'} - \frac{1}{v}\right) \approx \gamma H l \frac{1}{v}(v' - v) = \frac{\gamma H' l'}{m v^3}\hbar\omega \tag{2.63}$$

where $t = \gamma\hbar H l / m v^3$ is a time parameter.

(6) π**/2 flip and analyser**: The 90° flip turns one (say x) component of the precessing polarization parallel to the guide field direction (say z). The transmission coefficient of the analyzer strongly depends on the P_z component of the beam polarization. This allows us to determine P_x (by comparing the counting rates for P_x and $-P_x$). If the spin echo condition is not met, the probability of a neutron to arrive the detector decreases by $cos(\phi' - \phi)$, due to the polarization analyser. Thus, to calculate the effective polarization (neutrons arrived at the detector) the scattering function $S(\mathbf{q},\omega)$ should be weighted with $cos(\phi' - \phi)$. Finally:

$$P = \frac{\int S(\mathbf{q},\omega) cos(\omega t) d\omega}{\int S(\mathbf{q},\omega) d\omega} \tag{2.64}$$

$S(\mathbf{q},\omega)$ is the real part of the time dependent correlation function, i.e. intermediate scattering function $I(\mathbf{q},\omega)$. Thus, the directly observed result of a NSE experiment is:

$$P = S(\mathbf{q},t) = \frac{ReI(\mathbf{q},t)}{S(\mathbf{q})} \tag{2.65}$$

NSE characterisation of the swollen polymer chains

The overall diffusion of monodisperse sphere was first described by *Tanaka*[124] with a single exponential function:

$$S(q,t) \sim exp(-\Gamma(q)t) \tag{2.66}$$

where Γ is the relaxation rate of the collective network motion, t is a Fourier time. Plotting of the Γ vs. q^2 the collective diffusive coefficient D can be obtained from $\Gamma = Dq^2$[82].

The segmental chain dynamics requires the solution of the Langevin equation 2.10 and further its Fourier transformation from real to the reciprocal space. It gives the intermediate scattering function in Zimm model as[125]:

$$S(q,t) = exp(-q^2 D_i) S_{intern}(q,t) \tag{2.67}$$

The first part describe the diffusion motions with the relaxation rate proportional to q^2, $S_{inter}(q,t)$ corresponds to the internal relaxation.

Taking into account contribution of all polymer chain modes $S_{inter}(q,t)$ reads:

$$S_{inter}(q,t) = \frac{1}{N}\sum_{n,m}^{N} exp\left(-\frac{1}{6}q^2 B(n,m,t)\right) \tag{2.68}$$

with

$$B(m,n,t) = (n-m)^{2\nu} l^2 + \frac{4R_e^2}{\pi^2}\sum_{p=1}^{p_{max}} \frac{1}{p^{2\nu+1}} cos\left(\frac{\pi p n}{N}\right) cos\frac{\pi p n}{N}\left(1 - exp\left(-\frac{1}{\tau_p}\right)\right)$$

where N is number of beads in the chain with R_e being the end-to-end distance, p is the modes contributed to the dynamics.

Intermediate scattering function of Zimm dynamics can be approximated as:

$$S(q,t) \sim exp(-\Gamma_Z t)^{\beta} \tag{2.69}$$

with $\beta = 0.85$. Here Γ is Zimm relaxation rate determined by the solvent viscosity η_s as[126]:

$$\Gamma_Z = \frac{1}{6\pi}\frac{k_b T}{\eta_s} q^3 \tag{2.70}$$

Eq. 2.66 and Eq. 2.69 provide the basis for the description of the dynamics of the polymer systems. Nevertheless, dynamics behaviour of the microgels is not unique and usually more complex descriptions are needed[19,28,43,81,126]. The presence of the internal density inhomogeneities contributes to the dynamics of the microgel and often the intermediate scattering function decays to the certain constant ISF value. Therefore, an additional term $A(q)$, that describes elastic contribution to the scattering signal, is included in fitting function. Thus, Eq. 2.69 is extended to:

$$S(q,t) = A(q) + (1 - A(q))exp(-\Gamma t)^{\beta} \tag{2.71}$$

The microgels investigated in the current thesis show complex dynamics behaviour in probed q-range. The combination of the different function was applied. For the final data analysis the full Zimm-function (Eq. 2.67) taken into account an influence of the cooperative motions on the single polymer chain dynamics was applied[43]. The diffusion coefficient D_i and characteristic time $\tau_p = \eta_s R_e^3 p^{-3\nu}/(\sqrt{3\pi} k_B T)$ with the end-to-end distance of the polymer chain (set to the mesh size) R_e and $\nu = 0.5$[127] were used.

2.2.5 GINSES: opportunities and challenges

While grazing incidence small-angle neutron scattering (GISANS) is a widely used technique that allows accessing of the internal lateral structures of the polymer system adsorbed onto a solid surface or on a water/oil interface[72,90,111,128–132], grazing incidence neutron spin-echo spectroscopy (GINSES) is a novel method for the dynamics investigation of the thin polymer films, lamellar microemulsion, phospholipid membranes in the vicinity to the solid surface[78,91,92,94,133].

Classical neutron spin-echo spectroscopy[123,127] combined with grazing incidence geometry allows probing of the dynamics properties of the adsorbed systems as a function of a penetration depth of an evanescent waves[119]. Analogously to GISANS principles described before, at grazing incidence conditions with $\alpha_i < \alpha_c$, only near-surface dynamics can be probed. At higher incident angle, the penetration depth $\rightarrow \infty$ and more detailed depth profile of the sample can be obtained[90].

GINSES as well as GISANS due to the unique properties of the neutrons gives a direct access to the internal dynamics and structure of the adsorbed systems, but the experiment performing and the further data treatment in particular are a challenging task[134].

In real experiment, incoming beam is not ideal, that complicates the penetration depth estimation. J-NSE spectrometer operated by Jülich Forschungszentrum (MLZ, Garching, Germany)[122,135] has a wavelength resolution of 20%, at SNS-NSE spectrometer at the

Spallation Neutron Source (Oak Ridge, USA)[136] chopper system selects a wavelength band of 3 Å. To correct the difference in the scattering depth, caused by a difference in wavelength within incoming pulse, the application of the focused neutron prism was proposed and tested by *Frielinghaus et al.*[137]. In GI geometry almost whole incoming beam undergoes the total reflection and the scattering signal is usually weak, compared to the transmission geometry. To enhance this signal an application of the resonator was proposed. First experiments with 7-layer resonators show an increase of the scattering intensity on the factor of 3[138].

Above mentioned improves the data quality in the GIS experiment, nevertheless further data treatment is still not trivial. Therefore, application of the computer simulation can improve the quality of the GINSES data treatment and understanding of the internal dynamics at the presence of the solid surface (see Chapter 6).

2.2.6 Dynamic light scattering

Light scattering is a powerful technique in chemistry, biology, engineering, physics and medicine. Dynamic light scattering (DLS) allows to determine the static time-averaged properties, such as molecular weight, radius of gyration, and information on polymer-solvent interactions, based on static light scattering, and time-dependent properties, such as translational diffusion coefficient, hydrodynamic radius and its size distribution[139].

The principle of DLS experiment is presented in Figure 2.21. Here, the particles interact with the laser light and generate single scattering waves. Due to optical interference of all partial waves an overall scattered wave is generated. The random motion (Brownian motion) of the particles changes the distance to each other and therefore the spatial superposition (interference) of the individual scattering waves. Thus the intensity of the entire scattering wave fluctuates between a minimum (destructive interference) and a maximum value (constructive interference) over time. With the help of a photodetector the scattered light intensity is monitored over time and then autocorrelated.

For DLS analysis the hydrodynamic diameter is measured through optical detection of the Brownian motion of the particles in a liquid. The thermally agitated liquid molecules collide with the particles causing a random motion or diffusion. It causes the fluctuation of the scattered light intensity $I(q,t)$ which is detected in DLS experiment and is recorded in terms of the intensity of the time autocorrelation function $g^2(\tau)$ with the correlation time τ:

$$g^2(\tau) = \frac{\langle I(t)I(t+\tau)\rangle}{\langle I\rangle^2} \tag{2.72}$$

In order to determine the diffusion coefficient the first order autocorrelation function

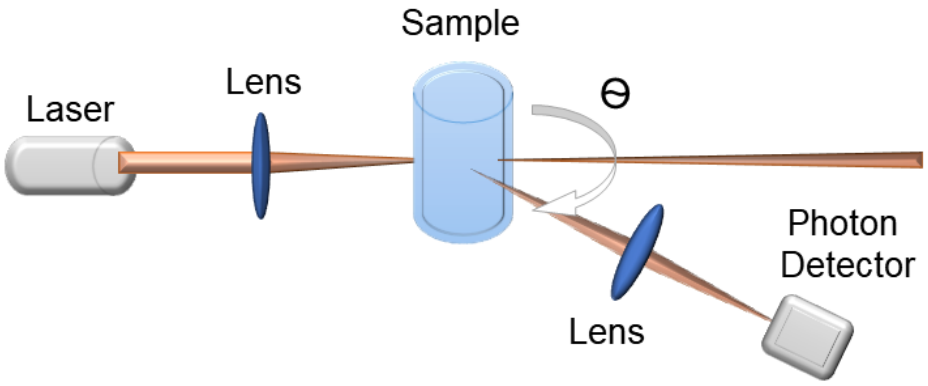

Figure 2.21: Scheme of dynamic light scattering experiment.

$g^1(\tau)$ is needed. From the Siegert relation[2]:

$$g^2(\tau) = 1 + \gamma \left(g^1(\tau)\right)^2 \tag{2.73}$$

where γ is an instrument parameter. For the monodisperse particles $g^1(t)$ is a simple exponential function:

$$g^1(t) = exp(-\Gamma\tau) \tag{2.74}$$

where Γ is the relaxation rate. Since real systems are not monodisperse and possess a size distribution, $G(\Gamma)$ considers this as:

$$g^1(t) = \int_0^\infty G(\Gamma) exp(-\Gamma\tau) d\Gamma \tag{2.75}$$

Using Γ the diffusive coefficient can be obtained as:

$$\Gamma = Dq^2 \tag{2.76}$$

If Γ shows linear dependence from q^2, the size or hydrodynamic radius R_h of the particles can be calculated according to the Stokes-Einstein equation:

$$D = \frac{k_B T}{6\pi\eta R_h} \tag{2.77}$$

where k_B is the Boltzmann constant, η is viscosity and T is the temperature of the liquid.

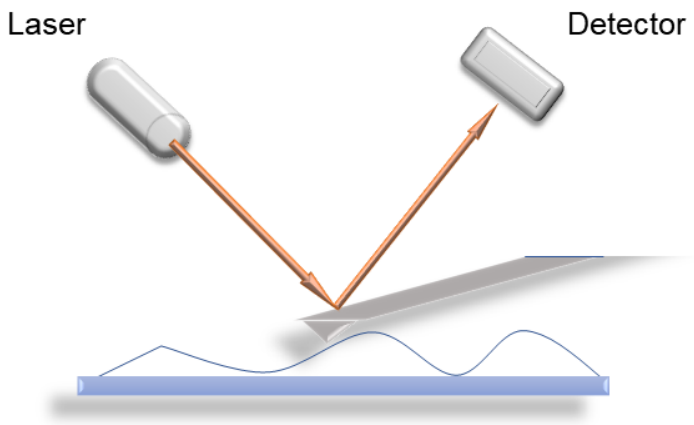

Figure 2.22: Schematic illustration of atomic force microscopy (AFM). The AFM tip scans over the surface to collect continuous images.

2.2.7 Atomic force microscopy

Atomic force microscopy (AFM) is a scanning probe microscopy technique that provides a 3D profile of the sample surface. In contrast to the scattering methods, AFM directly probes real-space length scales.

Figure 2.22 illustrates the main principle of AFM. The probe is supported on a flexible cantilever. When the tip of the probe moves near to a surface, the forces between the tip and sample deflect the cantilever according to Hooke's law:

$$F = -kx \tag{2.78}$$

where F is the force (typical forces between probing tip and sample range from 10^{-11} to 10^{-6} N), k is the spring constant and x is the cantilever deflection. The laser light is reflected from the back of the reflective cantilever and reaches a position-sensitive detector.

The tapping can be performed in different mode. In contact mode the tip is permanently in contact with the probed surface, while in non-contact mode the distance between the tip and the sample is controlled in a way that no contact appears. The AFM images within the current work were collected using the tapping mode. It allows to generate images in rather short time with a high resolution.

Chapter 3

Experimental section

3.1 Materials and sample preparation

Microgels investigated in the current work were prepared by J. Witte. The sample used for the investigation of the influence of the initiator concentration on the internal structure of microgels was prepared by M. U. Witt.

To give an overview about different sample types, a short description of components and preparation methods are given in the current section.

N-isopropylacrylamide ($\geq$ 99 %) (NIPAM), *N,N'*-methylenebisacrylamide ($\geq$ 99.5%) (BIS), 2,2'-azobis(2-methylpropionamidine) dihydrochloride (97%) (AAPH) and poly(ethyleneimine) ($\sim$50% in H_2O) (PEI) were purchased from Sigma-Aldrich (Munich, Germany). All chemicals were used as received. A Millipore Milli-q Plus 185 purification system was used for water purification. Chemical formulas of PNIPAM and BIS are presented in Figure 3.1.

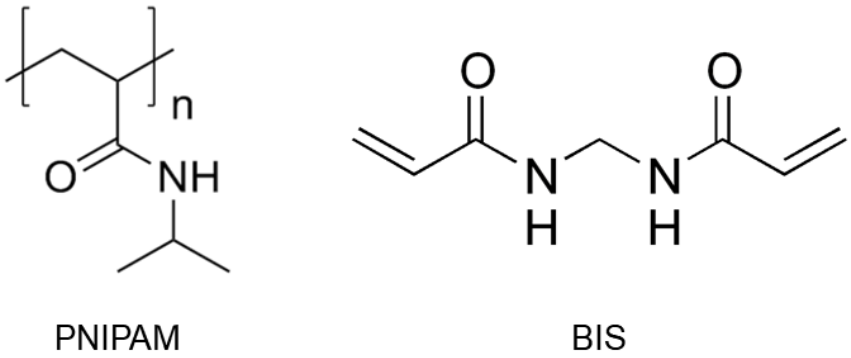

Figure 3.1: Chemical formulas of poly(*N*-isopropylacrylamide) (PNIPAM) and crosslinker *N,N'*-methylenebisacrylamide (BIS).

3.1.1 Microgel synthesis

The different ways of crosslinker incorporation during microgel synthesis may lead to a different crosslinker distribution within the microgel network. Localisation of the crosslinker mostly in the central "core" part during the batch-synthesis[140] and a more homogeneous distribution in the whole microgel volume obtained by the feeding approach[41,56] are expected.

Batch-microgels were synthesized via surfactant-free precipitation polymerization. The amount of the crosslinker varied between 0.5 mol% and 5 mol%. NIPAM (1.688 g, 14.9 mmol ($BIS_{0.5}$); 1.663 g, 14.7 mmol (BIS_2); 1.613 g, 14.3 mmol (BIS_5)) and BIS (0.012 g, 0.075 mmol ($BIS_{0.5}$); 0.046 g, 0.3 mmol (BIS_2); 0.115 g, 0.75 mmol (BIS_5)) were dissolved in 120 ml of water in a batch reactor. The solution was heated to 80°C and degassed with nitrogen for 60 min. Afterwards 1 ml of an aqueous solution of AAPH (0.25 mM for 1.7 mol% and 0.023 mM for 0.16 mol%) was added to the mixture while stirring continuously at 1000 rpm. After 10 min the reaction was quenched with an ice bath.

To access more homogeneous crosslinker distribution a continuous monomer feeding approach[56] was applied. 98 ml water in double walled glass reactor was treated as described. Above mentioned amount of NIPAM and BIS were dissolved in 22 ml water and purged with nitrogen for 60 min. Monomer and crosslinker were filled into a syringe which was mounted onto a pump. Prior to starting the monomer feed, the initiator solution was added into the reactor and the stirrer was set to 1000 rpm. The monomer solution was fed into the reactor at a rate of 2 mL/min. After 11 min 20 s the reaction was quenched.

For purification, the microgels were dialysed for 2 weeks with two water exchanges per day and freeze-dried at -85°C and 1×10^{-3} bar for 7 days.

3.1.2 Microgel deposition

Single crystal silicon blocks (50×80×15) mm were successively cleaned with acetone, ethanol and water and were dried under nitrogen flow. Afterwards, they were stored in an aqueous poly(ethyleneimine) (PEI) solution (0.01 g/mL) for 60 min and subsequently rinsed with water and dried under nitrogen flow. Microgels were deposited onto the PEI-coated silicon blocks via spin coating for 150 s with 500 rpm from aqueous microgel dispersion (0.01 g/mL). For AFM imaging the microgel dispersion was spin coated with identical parameters onto silicon wafers of (20 x 20) mm.

For convenience, microgels prepared via bath synthesis are named b-MG_X or batch-microgel and microgel prepared via continuous monomer feeding approach f-MG_X or feeding-microgel in the following, where x indicates concentration of the crosslinker BIS in the system (0.5 mol%, 2 mol% or 5 mol%). In this series all systems were prepared with 1.7 mol% initiator (AAPH). Additional sample with 0.16 mol% initiator was called b-$MG^*_{0.5}$. For adsorbed microgels additional index A is used: Ab-MG_X.

3.2 Instruments

3.2.1 (Grazing incidence) Small-angle neutron scattering

Small-angle neutron scattering (SANS) experiments in transmission as well as in grazing incidence (GISANS) geometry were performed on small-angle scattering diffractometers KWS-1[141,142], KWS-2[143,144] and on very small angle scattering diffractometer with focusing mirror KWS-3[145]. All instruments are operated by Jülich Centre for Neutron Science (JCNS) at the research reactor FRM II of the Heinz Maier-Leibnitz Zentrum (MLZ) in Garching, Germany. Layouts of the instruments are presented in Figure 3.2, 3.3, 3.4.

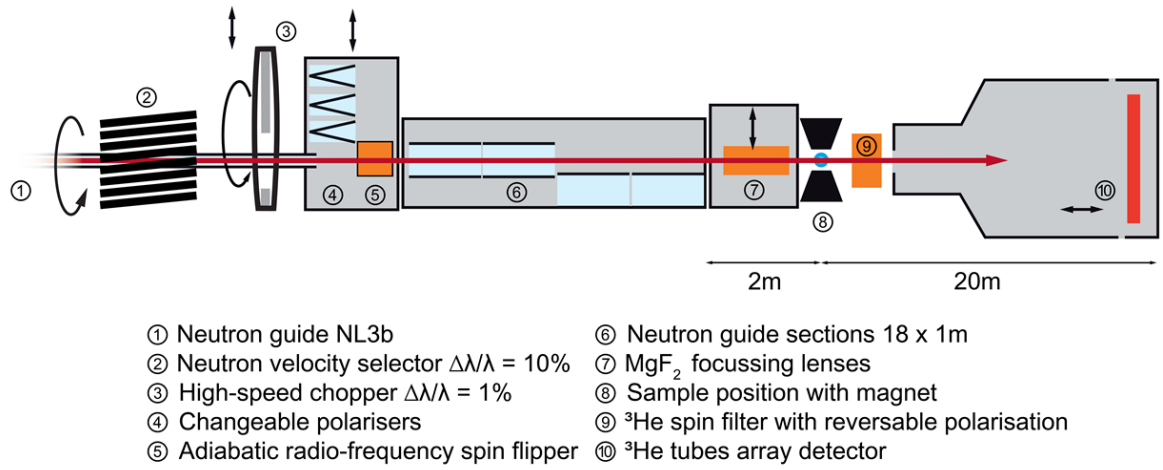

Figure 3.2: Layout of the small-angle diffractometer KWS-1. © FZJ

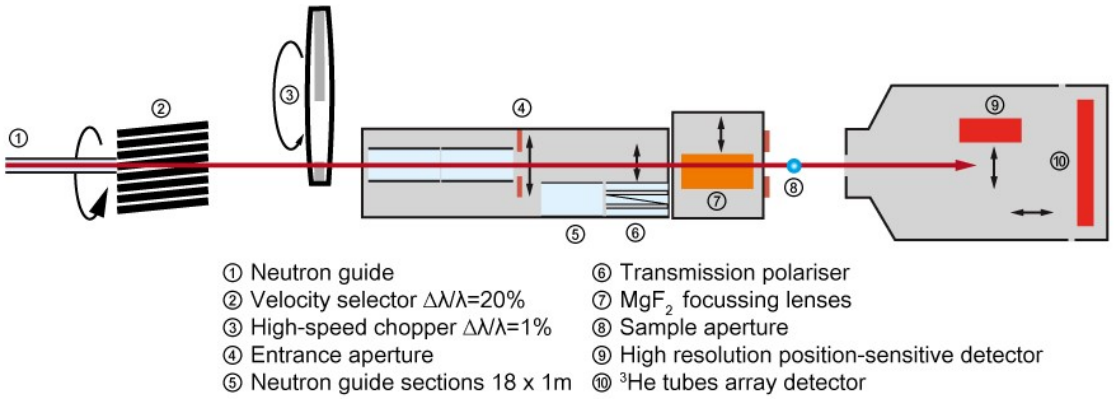

Figure 3.3: Layout of the small-angle diffractometer KWS-2. © FZJ

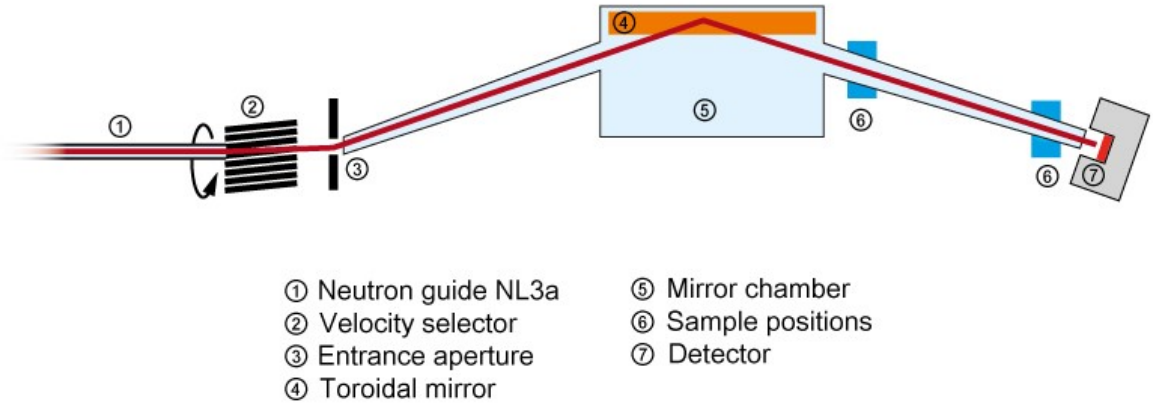

Figure 3.4: Layout of the very small-angle scattering diffractometer with focusing mirror KWS-3. © FZJ

The parameters of instrumental setup used for the SANS and GISANS experiments are presented in Table 3.1. To cover a wide q-range and thus to probe structural features of the microgels in the range from nm to μm different sample-to detector distances (StDD) were used.

The KWS-1 and KWS-2 instruments are optimized to relatively high resolution measurements owing to their neutron velocity selector with $\Delta\lambda/\lambda = 10\,\%$. The neutron velocity selector monochromatices the beam of cold neutrons. The 20 m-long collimation line is enclosed in a nonmagnetic evacuated chamber with five active apertures. The neutron guides themselves have a supermirror coating of nonmagnetic $Ni_{0.96}Mo_{0.04}$/Ti on boron glass. Active apertures are positioned at 2, 4, 8, 14 and 20 m from the sample and are used to define the source aperture for the corresponding collimation distances. The collimation apertures are suitable for GISANS experiments, where one needs slit collimation either in the vertical or in the horizontal direction. Towards the sample, the collimation nose has an adjustable sample slit from 1×1 mm^2 to 30×30 mm^2. Additionally, the center of the sample aperture can be moved in the X and Y directions across the beam.

KWS-1 and KWS-2 are equipped with 2D position-sensitive detectors. The detectors have approx. 144 x 144 pixels active surface with a dead time of about 0.07 μs. A beamstop is used to determine the intensity of the direct beam for transmission measurements.

KWS-3 is a very small angle neutron scattering (VSANS) instrument. The principle of this instrument is a one-to-one image of an entrance aperture onto a 2D position sensitive detector by neutron reflection from a double-focussing toroidal mirror.

The instrument's standard configuration with a 9.5 m sample-to-detector distance allows performing scattering experiments with a wave vector transfer between 4.0×10^{-5} and

Table 3.1: Instrument configurations used in experiment

Instrument	Method	Wavelength, Å	StDD, m	Resolution, $\Delta\lambda/\lambda$
KWS-1	SANS	5	1.5, 8, 20	10%
	GISANS	5	20	10%
KWS-2	SANS	5	2, 8, 20	10%
KWS-3	SANS	12.8	1, 9.5	20%
	GISANS	12.8	9.5	20%

2.5×10^{-3} Å^{-1}. A second sample position at 1.3 m sample-to-detector distance extends the q-range of the instrument to 2.0×10^{-2} Å^{-1} and reaches more than one decade overlapping with the classical SANS instruments (KWS-1: $q = 7 \times 10^{-4}$ – 0.5 Å^{-1} and KWS-2: $q = 1 \times 10^{-4}$ – 1 Å^{-1}).

Further technical details of each instrument could be found in the corresponding references.

In GISANS experiments the samples were mounted in an in-house developed thermostated sample cell[146]. With a Teflon trough inside aluminium housing the sample was sealed against air. To achieve the largest scattering contrast with the protonated microgels, the cell was filled with deuterated water (D_2O). Temperature control of ± 0.1°C precision inside the cell was achieved by water circulation through the aluminium housing. All samples were measured at 20°C and 50°C. These temperatures were chosen to observe the behaviour of the microgels below and above the VPTT. The cell was mounted on a goniometer stage to achieve the necessary angle of incidence. The neutron beam entered the sample through the silicon block. To reduce the background and block the direct neutron beam Cd shieldings at the entrance and exit sides were used.

Obtained data were reduced and analysed using qtiKWS10 and SasView 4.1.2 software.

3.2.2 Small-angle X-ray scattering

Small-angle X-ray scattering (SAXS) experiments were performed on the diffractometer GALAXI[147] operated by Jülich Centre for Neutron Science (JCNS) in Jülich, Germany. The layout of the instrument is presented in Figure 3.5.

As an X-ray source a liquid metal jet of a GaInSn alloy as anode is used. Parabolic optics are used to parallelize the beam and monochromatize it by allowing only the GaKa radiation ($E = 9243$ eV photon energy) to pass. A collimation with two 4-segment slits separated by 4.0 m distance defines the size and the collimation of the beam at the sample position. A third slit is used to reduce the background. At the sample position, the sample

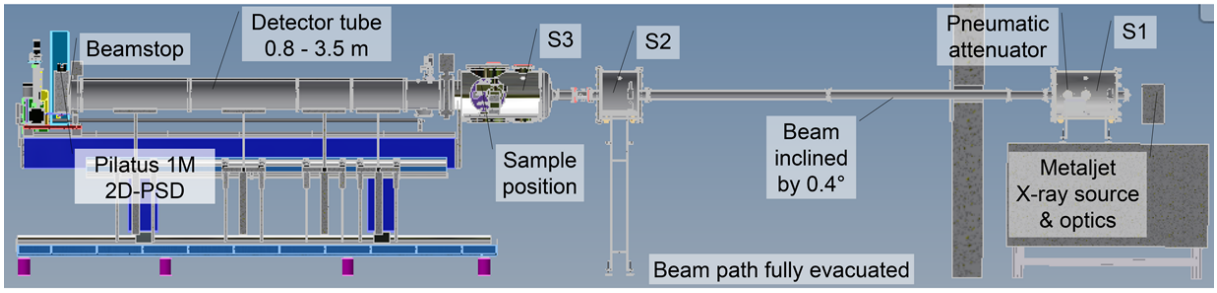

Figure 3.5: Layot of the X-ray diffractometer GALAXI. Figure is from Ref.[147]

can be adjusted by two rotational and two translational degrees of freedom. As a detector, a Pilatus 1M 2D position sensitive detector with 169 x 179 mm^2 active area is used.

SAXS measurements were performed in transmission geometry with a wavelength of 0.134 nm.

3.2.3 Neutron reflectometry

To probe the structure of the adsorbed microgels in direction normal to the surface neutron reflectometry experiment was performed on the MARIA (magnetic reflectometer with high incident angle) instrument[148] operated by Jülich Centre for Neutron Science (JCNS) at the research reactor FRM II of the Heinz Maier-Leibnitz Zentrum (MLZ) in Garching, Germany. Layout of the instrument is presented in Figure 3.6. For experiments neutrons with wavelength of 5Å and wavelength spread $\Delta\lambda/\lambda$ of 10% were used. Measurements were performed in non-polarised beam mode.

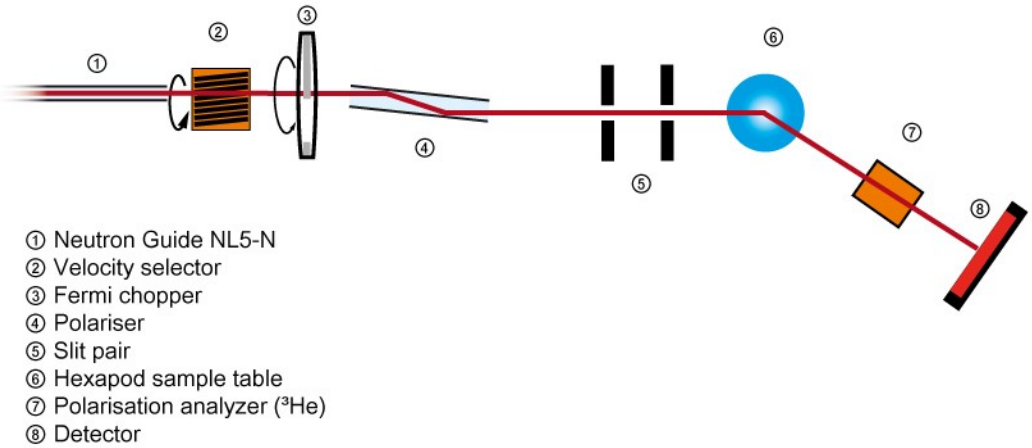

Figure 3.6: Scheme of MARIA diffractometer. © FZJ

Neutron reflectometry data were treated using Motofit package within the analysis

package IGORPro[116] and BornAgain 1.14.0[149] software.

3.2.4 Neutron spin-echo spectrometry

In order to investigate polymer dynamics spin-echo experiments were carried out on J-NSE spectrometer operated by Jülich Centre for Neutron Science (JCNS) at the research reactor FRM II of the Heinz Maier-Leibnitz Zentrum (MLZ) in Garching, Germany. In the period of this work, old precession coils[122] on J-NSE instrument were replaced by the novel superconducting solenoid sets[135]. They increased instrument resolution and reduced measurement time. In both instrumental set-ups measurements were performed in q-range of 0.04 – 0.19 Å^{-1} at wavelength of 8 Å, probing Fourier times up to 40 ns. Layout of the J-NSE instrument is presented in Figure 3.7.

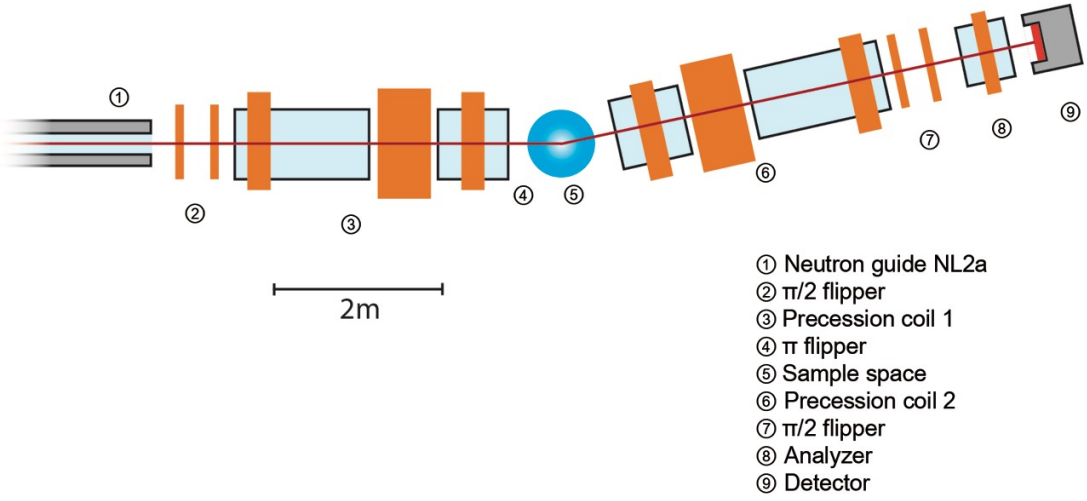

Figure 3.7: Layout of the J-NSE instrument. © FZJ

3.2.5 Dynamic light scattering

For temperature-dependent dynamic light scattering (DLS) experiments the microgel dispersions with a concentration of $c = 0.1$ mg/mL were measured using an LS spectrometer equipped with a He-Ne laser ($\lambda = 632.8$ nm). Each autocorrelation function was measured for 45 s and temperatures between 20 and 50°C were chosen. At each temperature, the scattering angle was varied between 30° and 100° in 5° steps.

The size analysis with DLS is only valid for single light scattering event. Samples of high concentrations show a large proportion of multiple scattered light and the method

reaches its limitations. Therefore, to generate reliable results, samples have been diluted down to 0.01 wt%.

3.2.6 Atomic force microscopy

Atomic force microscopy (AFM) of microgels in dry state was performed with an Cypher (Asylum) microscope under ambient conditions. Images were scanned in the intermittent contact mode with a silicon cantilever (OMCL-AC160TS) with a spring constant of 26 N/m and a resonance frequency of 300 kHz. The chosen scan size was 20×20 μm. For image analysis MFP3D software was used.

Measurements in water environment were performed with KeySight 5500 SPM in contact mode at room temperature. Cantilever PNP-TR-20 with a spring constant of 0.08 N/m and a resonance frequency of 17 kHz was used. For image analysis Gwyddion 2.4 software was used.

Chapter 4

Inner structure and dynamics of microgels with low and medium crosslinker content prepared via surfactant-free precipitation polymerization and continuous monomer feeding approach *

Abstract

Preparation of poly(*N*-isopropylacrylamide) particles via classical precipitation polymerization and continuous monomer feeding approach leads to different internal crosslinker distributions, i.e. from core-shell-like to more homogeneous. Peculiar properties of these microgels with low and medium crosslinker concentration are studied by means of dynamic light scattering and small-angle neutron scattering in a wide q-range below and above the volume phase transition temperature. Influence of the cross-linking degree, initiator concentration and preparation process on the internal structure of the microgels are investigated. In contrast to the classical conception where polymer particles possess a core-shell structure with uniform distribution of the polymer segments (averaged internal polymer density distribution), a detailed insight into the internal inhomogeneities of the PNIPAM microgels and the presence of the internal domains even above the volume phase transition temperature, when polymer particles are in the collapsed state are presented. The correlations (i) between initiator concentration with a fluffiness of the particles and (ii) a size of internal domains which appear inside the microgel with temperature increase are demonstrated. Moreover, influence of the internal inhomogeneities on the dynamics of the polymer particles studied by means of neutron spin-echo spectroscopy is presented.

*Similar content is presented in "Inner structure and dynamics of microgels with low and medium crosslinker content prepared via surfactant-free precipitation polymerization and continuous monomer feeding approach", T. Kyrey, J. Witte, A. Feoktystov, V. Pipich, B. Wu, S. Pasini, A. Radulescu, M. U. Witt, M. Kruteva, R. von Klitzing, S. Wellert, O. Holderer, Soft Matter (2019) 15, 6536 – 6546, doi: 10.1039/c9sm01161g

4.1 Introduction

Despite the number of works dedicated to the investigation of the PNIPAM/BIS structure and its influence on physico-chemical properties of the microgels[27,150,151], a direct comparison of the microgels with different internal crosslinker distribution is very limited[40].

The internal structure of microgels in solvent is difficult to access. In the swollen state, below the VPTT, slight polymer density variations are mostly hidden by the low contrast in scattering experiments. And also above the VPTT, microgels are mainly regarded as rather compact spherical particles.

Therefore, in this chapter a detailed view into the inner microgel structure is revealed with light, X-ray and neutron scattering methods. The combination of small- (SANS) and very small- (VSANS) angle neutron scattering, small-angle X-ray scattering (SAXS) and dynamic light scattering (DLS) provides a detailed characterisation of the structural particularities within a single microgel in dependence on (i) preparation process, (ii) crosslinker and initiator concentration and (iii) temperature.

In order to investigate the influence of the internal crosslinker distribution on the internal dynamics of the microgels prepared via batch and feeding approaches neutron spin-echo (NSE) spectroscopy was applied.

4.2 Results

In order to investigate the influence of the amount of the crosslinker (BIS) on the structure of microgels synthesised by the batch and feeding method, small-angle neutron scattering experiments in a wide q-range (2×10^{-4} – 0.4 Å^{-1}) at temperatures below and above the VPTT were performed.

4.2.1 Structure of microgels below the VPTT

The microgel structure in the swollen state according to *Shibayama*[35] was analysed in terms of the correlation length of the fluctuation and the frozen inhomogeneities (see Section 2.2.2), which become detectable below the VPTT, in our case at 20°C. While the correlation length (ξ) and the frozen inhomogeneities (Ξ) characterize the crosslinker distribution within microgel (Figure 2.2), here the internal structure of the microgels was investigated based on the model at first presented by *Bastide* and *Leibler*[36]. Hence, the fitting function of the scattering spectra of the microgels at 20°C was performed with Eq. 2.28.

Results of the fits according to Eq. 2.28 and fit parameters for the batch- and feeding-microgels at 20°C are presented in Figure 4.1 and Table 4.1, respectively.

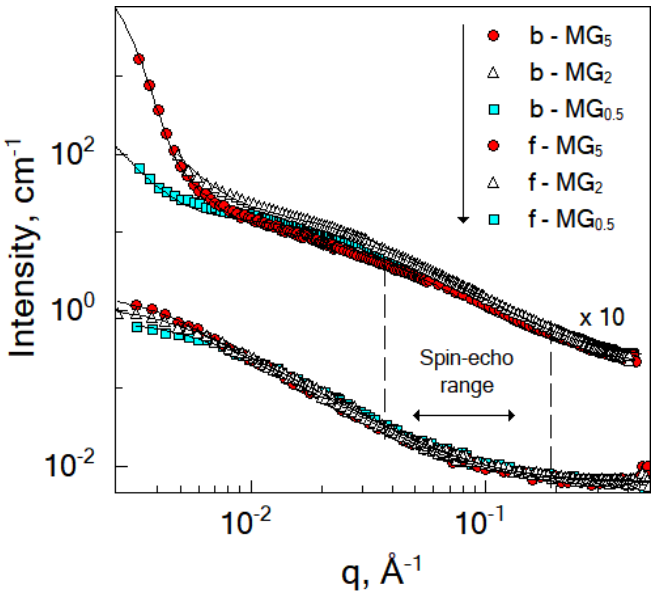

Figure 4.1: SANS spectra and the corresponding fits of the the batch-microgels (top curves, b-MG$_X$) and the feeding-microgels (bottom curves, f-MG$_X$) crosslinked with 0.5 mol% BIS (cyan squares), 2 mol% BIS (white triangles) and 5 mol% BIS (red circles). Measurements were performed at 20°C in D_2O.

Table 4.1: Fit parameters of the SANS data of the microgels at 20°C according to Eq. 2.28. R_{DLS}^{20C} and R^{20C} is radii of microgels according to DLS and SANS measurements, respectively. Errors are <5%, otherwise they are given in parentheses. Parameters of b-MG$^*_{0.5}$ are presented here for the comparison with b-MG$_{0.5}$ and will be described in section 4.2.4.

System	ξ, nm	Ξ, nm	R_{DLS}^{20C},nm	R^{20C},nm
b-MG$_{0.5}$	3.5	170	265	-
b-MG$_2$	3.6 (0.6)	86.6 (8.5)	313.4	-
b-MG$_5$	3.6	82.6	350	136.6
b-MG$^*_{0.5}$	3.6	137 (33)	544.6	-
f-MG$_{0.5}$	7.6	12.6	-	-
f-MG$_2$	8.7	19.8	-	-
f-MG$_5$	8.7	20.3	379	-

4.2.2 Structure of microgels above the VPTT

Figure 4.2 represents scattering spectra of the collapsed batch- and feeding-microgels at 50°C in D_2O. The scattering signal of the batch-microgels measured above the VPTT significantly differs from the scattering signal of the feeding-microgels. Therefore, the model applied for the structure characterisation was adjusted for each microgel type (see further).

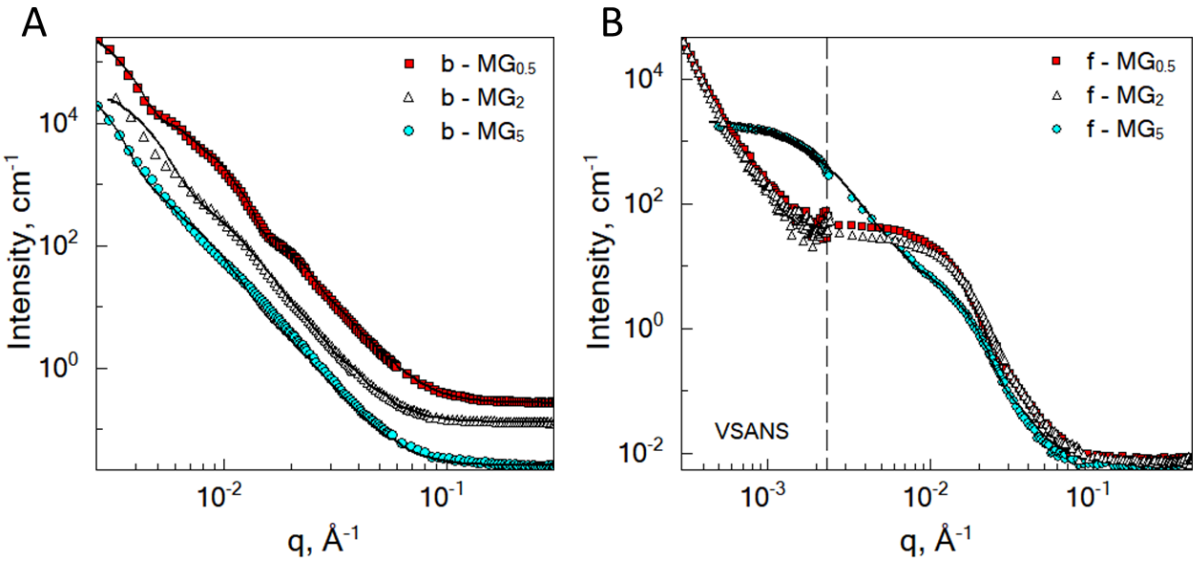

Figure 4.2: A) Scattering spectra of the batch-microgels in classical SANS q-range. Spectra have been offset for clarity. B) Scattering spectra of the feeding-microgels in low (VSANS) and classical (SANS) q-range. Different spectra correspond to the different crosslinker concentration: 0.5 mol% BIS – red squares, 2 mol% BIS – white triangles and 5 mol% BIS – cyan circles. All spectra were measured at 50°C in D_2O. Solid lines correspond to the fits according to the chosen model (see text).

While the microgel b-MG_5 possesses a rather monotonous decay of the scattering intensity with q, the scattering signal of the microgels with 0.5 and 2 mol% BIS (b-$MG_{0.5}$ and b-MG_2) show more distinct features (Figure 4.2A).

Initially, fuzzy-shell as well as core-shell models, which are often used for the characterization of the systems similar to b-MG_x [2,35,45], were applied, but no satisfying results were obtained. Fit curves did not describe the behaviour of the experimental curves in the whole q-range. The deviation of the scattering data from the Porod law fit is presented in Figure A1 in Appendix. Therefore, to fit the scattering spectra of the batch-microgels in the collapsed state a Spheres-in-Sphere (SiS) model was proposed:

$$I(q,R,r) = I_1 P(q,R) S(q,R) + I_2 P(q,r) S(q,r) + I_{inc} \tag{4.1}$$

where $P(q,x) = F^2_{sphere}(q,x)$ is the form factor of a sphere with a radius x (R – radius of microgel in the first term, r – radius of inner spherical domain in the second term), $F_{sphere}(q,x)$ is the scattering amplitude of the homogeneous sphere according to Eq. 2.31, I_{inc} takes into account the incoherent scattering. $I_i(i=1,2) = \phi_i V_i (\Delta\rho_i)^2$ is the scaling factor (ϕ_i is a volume concentration of the object (microgel at $i=1$ and domain at $i=2$) with a volume V_i in the system with volume V, ρ_i is the scattering length density).

Due to the low concentration kept for the polymer microgels in experiment, $S(q,R)$ was assumed to $S(q,R) = 1$. Polydispersity of the microgel radius was taken into account in the fitting procedure (values of 10 – 17% were obtained). Due to a low amount of the spherical domains within a single microgel (see Discussion) the internal structure factor $S(q,r)$ was taken as 1.

Fitting parameters, the hydrodynamic radii (R_{DLS}) as well as the number (N^*) of domains and their volume fraction within one microgel (φ) are presented in Table 4.2. The volume fraction of the domains within the microgel was calculated as $\varphi = N^* r^3/R^3$, N^* was obtained from I_1 and I_2 as presented in Appendix.

Table 4.2: Characteristic parameters of the batch-microgels measured at 50°C: C_{IN} is an initiator concentration, R and r are radii of microgel and internal domains according to Eq. 4.1 from SANS, R^{50C}_{DLS} is the hydrodynamic radius of the batch-microgels, N^* is a number of domains per microgel, φ is a volume fraction of the domains within the microgel. Errors of R^{50C}_{DLS} are <5%, of R, r are <1%. Parameters of b-MG$^*_{0.5}$ are presented here for the comparison with b-MG$_{0.5}$ and will be described in section 4.2.4.

System	C_{IN}, mol%	R, nm	r, nm	R^{50C}_{DLS}, nm	N^*	φ, %
b-MG$_{0.5}$	1.7	100	28.6	101	5-14	12-33
b-MG$_2$	1.7	93.9	21.7	94	4-11	5-14
b-MG$_5$	1.7	132.5	33.2	149	13-38	20-60
b-MG$^*_{0.5}$	0.16	113	40.6	121.6	2-6	9-28

It should be noted, that the chosen SiS model with the same size parameters also describes the SAXS spectrum of the b-MG$_{0.5}$. Due to the higher resolution due to the small wavelength spread compared to SANS, features of the scattering curve are even more pronounced. The SiS model is in good agreement with the experimental data, moreover fitting parameters R and r yield equal results for both methods SANS and SAXS (see Figure A2 and Table A1 in Appendix).

In case of the batch-microgels the inner domains are uncorrelated and no contribution of an internal structure factor is detected, whereas in the case of feeding-microgels the internal structure factor plays an important role. The feeding-microgel contains domain-like inhomogeneities with such a density, that the internal structure factor has to be taken

into account to fit the experimental data (Figure 4.2B). The second term of the fit function (Eq. 4.1) has to include contributions from the internal structure factor, which, according to Teixeira[106], can be written in terms of randomly distributed domains with radius r' organised in clusters (Eq. 2.32).

It was necessary to include a particle size distribution in order to properly describe the scattering curves. Thus a polydispersity factor of 0.29 was used. The parameters D_f, l, r' were free in the fitting procedure. The fitting results are shown in Table 4.3.

Table 4.3: Fit parameters of the feeding-microgels measured at 50°C. r' and l is the radius of domains and the correlation length representing the cluster size, respectively. Errors are <5%.

System	r', nm	l, nm
f-$MG_{0.5}$	15.8	>400
f-MG_2	14.2	>400
f-MG_5	12.5	47.1

4.2.3 Inter-microgel correlations

To study the correlation between microgels in solution, a very small-angle neutron scattering (VSANS) experiment was performed in a q-range of 2×10^{-4} – 2.5×10^{-3} Å^{-1} (length in range of 250 – 3000 nm was probed). Measurements were carried at temperatures from 20°C to 50°C.

The scattering curves of the batch-microgels at 20°C in this very low q-range have clear peaks (Figure 4.3A), while the spectra of the feeding-microgels possess a power-law q-dependence according to Eq. 2.26 with exponent α (Figure 4.3B). Exponent values of 1.5, 1.9 and 2.5 for f-$MG_{0.5}$, f-MG_2 and f-MG_5, respectively, were obtained. Increase of α at higher crosslinker concentration (C_{BIS}) indicates an increase of the number of the polymer branching points, while a lower α at lower C_{BIS} indicates a softer and more flexible polymer structure. According to Hammouda[100] $\alpha = 1.67$ corresponds to the fully swollen chains and $\alpha = 3$ – to the clustered networks.

Figure 4.4 represents selected scattering spectra of the systems b-MG_x at 20°C, 33°C and 50°C. Spectra at 20°C and 33°C possess characteristic peaks, that correspond to the inter-microgel distances. In case of 5 mol% BIS, the peak position shifts to higher q with increasing temperature (Figure 4.4C), whereas for systems with 0.5 and 2 mol% BIS the position of these peaks, i.e. the distance between microgels, does not change with the temperature increase up to 33.5°C and disappears above the VPTT (Figure 4.4 A,B).

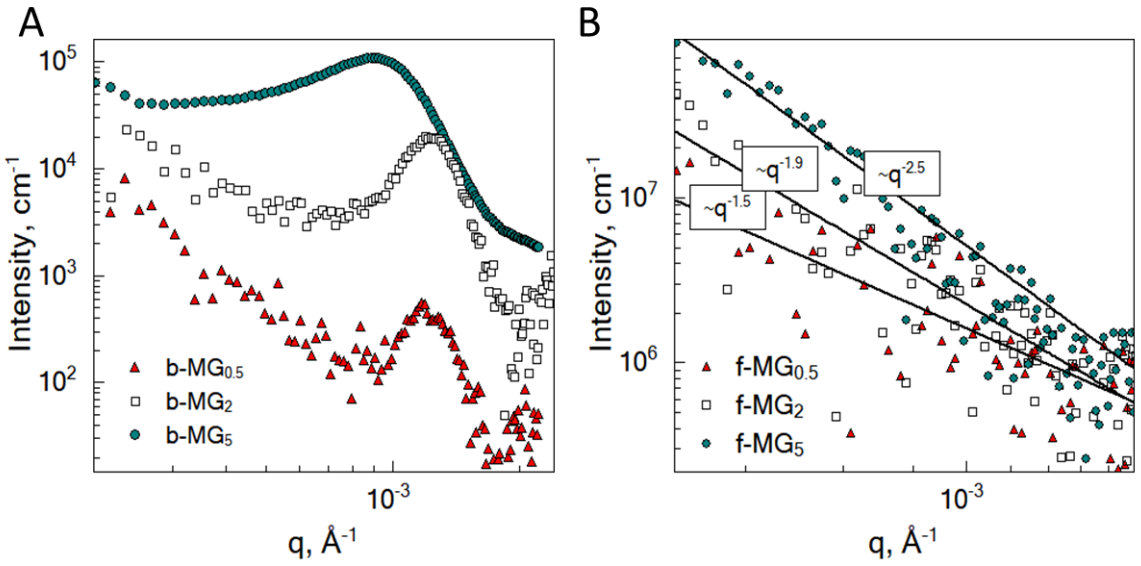

Figure 4.3: VSANS spectrum of the batch- (A) and feeding- (B) microgels at 20°C in D_2O: 0.5 mol% BIS – red triangles, 2 mol% BIS – white squares, 5 mol% BIS – cyan circles. Lines correspond to the fits according to the power-law $I(q) = A/q^{\alpha}$.

The position of each peak (q^*) at 20°C and values of $a \sim 2\pi/q*$, which correspond to the microgel-microgel distance in real space, together with the hydrodynamic radii of microgels measured with DLS are listed in Table 4.4.

Table 4.4: Characteristic parameters of the batch-microgels at 20°C. C_{IN} is an initiator concentration, q^* and a is the peak position from Figure 4.4 and corresponding distance between microgels, R_{DLS}^{20C} is the hydrodynamic radius of the batch-microgels. Errors are <5%, otherwise they are given in parentheses. Parameters of b-$MG_{0.5}^*$ are presented here for the comparison with b-$MG_{0.5}$ and will be described in section 4.2.4.

System	C_{IN}, mol%	q^*x10^{-3}, nm^{-1}	a, nm	R_{DLS}^{20C}, nm
b-$MG_{0.5}$	1.7	11.9 (1.8)	528	265
b-MG_2	1.7	12.2 (1.3)	515	313.4
b-MG_5	1.7	8.8 (2.3)	714	350
b-$MG_{0.5}^*$	0.16	11	571.2	544.6 (22)

The centre-to-centre distance (according to the VSANS spectra in temperature range of 20 – 60°C) decreases with increasing temperature sharper for 0.5 and 2 mol% BIS. For 5 mol% BIS there is a smooth transition through the VPTT. The different behaviour of b-MG_x systems in the vicinity of the VPTT is attributed to the topological constraints that are introduced into the polymer network, i.e. a lower crosslinking degree leads to stronger polymer response on the temperature change close to the VPTT[59,152].

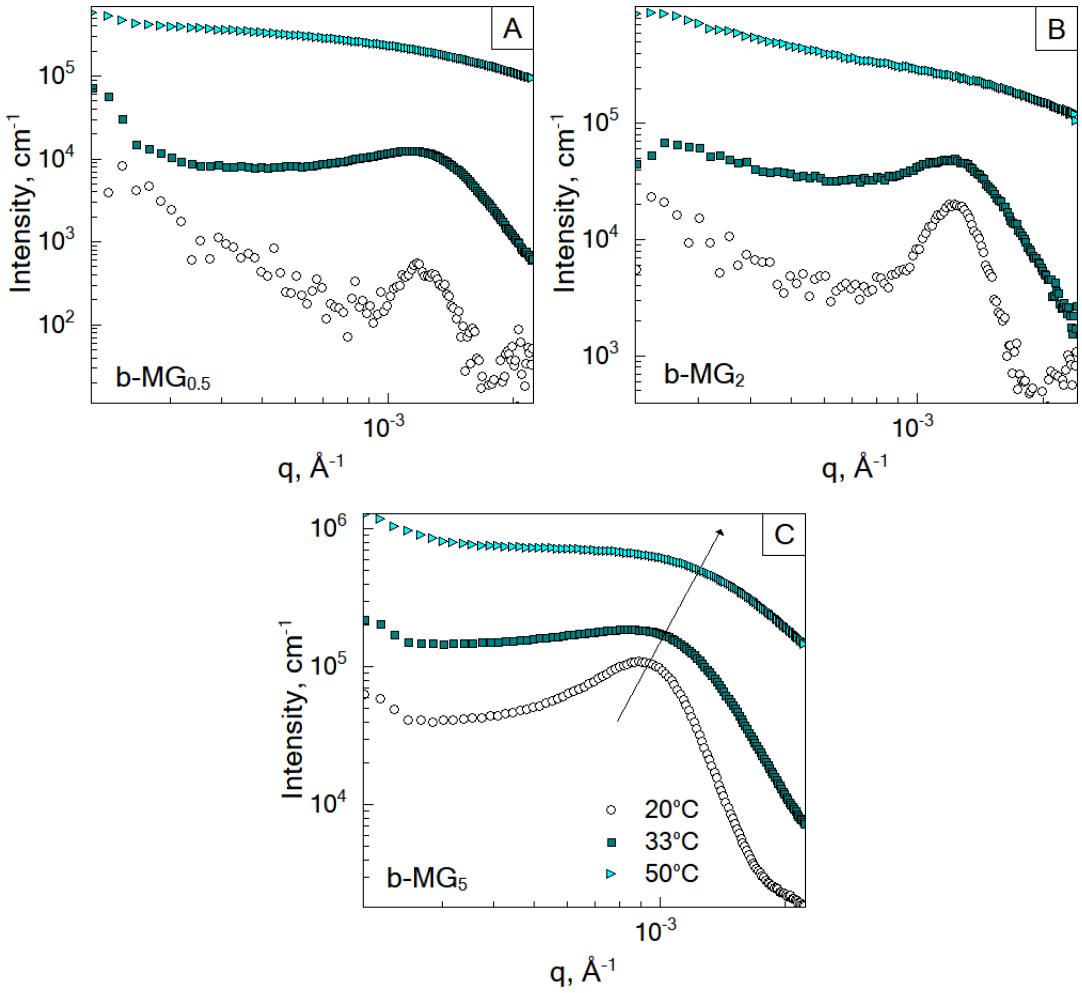

Figure 4.4: Selected scattering spectra of the batch-microgels (A – b-$MG_{0.5}$, B – b-MG_2, C – b-MG_5) in very low q-range at different temperatures (20°C – white circles, 33°C – dark cyan squares, 50°C – cyan triangles).

4.2.4 Effect of initiator concentration

In microgel synthesis an initiator is necessary to start the polymerisation reaction. It was suggested that the amount of the initiator AAPH may also influence the internal structure of the microgels, i.e. size and distribution of the internal domains. To prove this hypothesis, an additional experiment was performed. Since the spectra of b-$MG_{0.5}$ microgel with 1.7 mol% of initiator (AAPH) showed the most pronounced features (Figure 4.2), it was chosen as a model system. An additional microgel with 0.16 mol% AAPH and 0.5 mol% BIS (b-$MG^*_{0.5}$) was prepared via batch precipitation polymerization and studied by means of SANS and VSANS below (20°C) and above (50°C) the VPTT. The scattering spectra of b-$MG_{0.5}$ and b-$MG^*_{0.5}$ are presented in Figure 4.5.

Position of the peaks q^* at 20°C as well as fit parameters of SANS curves for b-$MG_{0.5}$

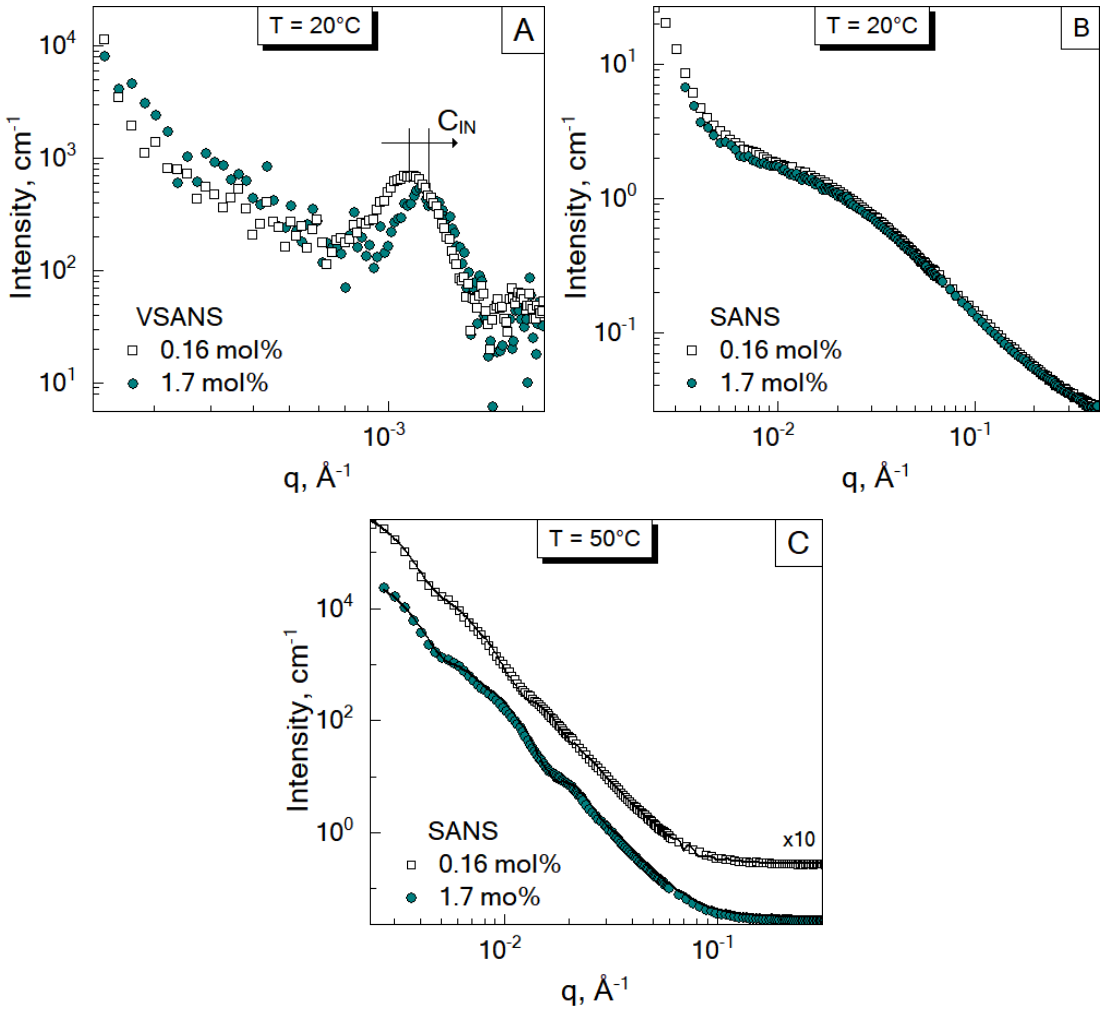

Figure 4.5: A) VSANS scattering spectra of the batch-microgels b-$MG_{0.5}$ and b-$MG^*_{0.5}$ (very low q-range) at 20°C. B) SANS scattering spectra of b-$MG_{0.5}$ and b-$MG^*_{0.5}$ at 20°C. C) SANS scattering spectra of b-$MG_{0.5}$ and b-$MG^*_{0.5}$ at 50°C. In all figures white squares correspond to b-$MG^*_{0.5}$ with 0.16 mol% AAPH and cyan circles to b-$MG_{0.5}$ with 1.7 mol% AAPH.

and b-$MG^*_{0.5}$ at 20°C and 50°C are presented in Table 4.1, Table 4.2 and Table 4.4.

4.2.5 Internal dynamics

To probe the internal dynamics of the microgels in the swollen state a neutron spin-echo (NSE) experiment was carried out at 20°C. The collapse at 50°C limits the free polymer chain motions. It prevents the coverage of the wide q-range and makes the microgel dynamics investigation in collapsed state not feasible. Normalized intermediate scattering functions (ISF) of the microgels b-MG_5 and f-MG_5 measured in a q-range of 0.041 – 0.19 $Å^{-1}$ at 20°C are presented in Figure 4.6.

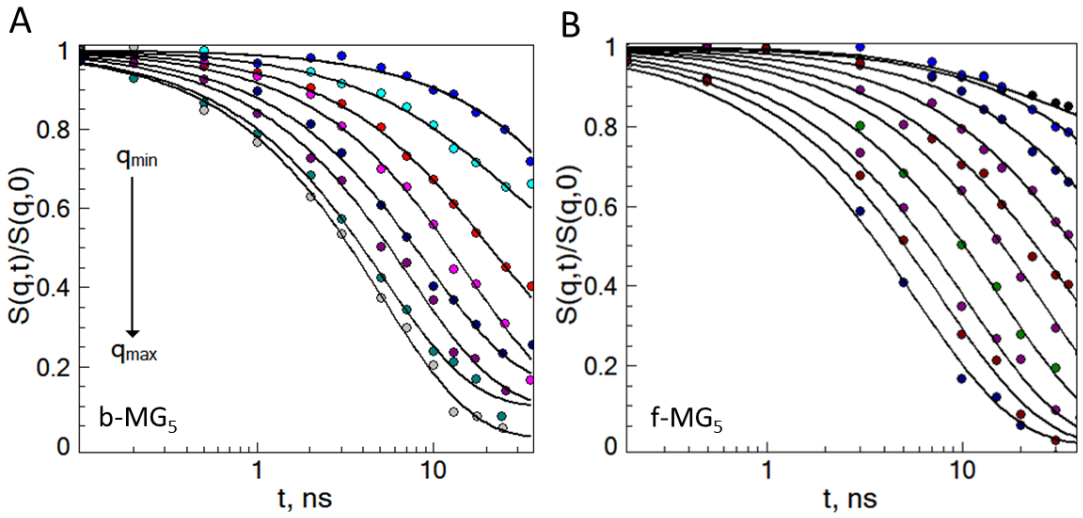

Figure 4.6: Normalized intermediate scattering function of the b-MG_5 (A) and f-MG_5 (B) microgels in the range $q_{min} = 0.041$ Å^{-1}, $q_{max} = 0.19$ Å^{-1}. Measurements were performed at 20°C in D_2O. Lines correspond to the fit according to Eq. 2.71 with $\beta = 0.85$.

Earlier *Hellweg et al.*[3,4] showed that NSE data of the PNIPAM microgels with BIS concentrations of 1, 2 and 5% can be described by a single exponential function with two adjustable parameters (amplitude and relaxation rate). A decrease of the cooperative diffusion coefficient with the increase of the crosslinker concentration was observed. The application of this model to our systems does not give a good agreement with the experimental data over the whole q-range. The application of the different models to the experimental ISF is presented in the Figure A4 (Appendix).

For the characterisation of the dynamics behaviour of microgel systems (except b-MG_5) a full Zimm model presented in Eq. 2.67 was applied[43]. In this case, the microgel dynamics can be described with a single set of parameters by the numerical solution of the Zimm model which include the diffusive contribution for the internal density fluctuations (D_i) and η_s as a second fit parameter.

Since the single chain dynamics becomes modified on a very local length scale (see Discussion), the diffusion coefficient was obtained from the medium q-range (Figure A5 in Appendix). The diffusion coefficient, D_i, as well as the solvent viscosity, η_s, of each microgel obtained in the fit procedure are listed in Table 4.5.

The NSE data of b-MG_5 were fitted with a single exponential function with $\beta = 1$ taking into account cooperative motions (Eq. 2.71). A cooperative diffusion coefficient D_c of $(5.1 \pm 0.1) \cdot 10^{-11}$m^2/s was found (Table 4.5). A value for ξ_d of 3.4 nm was estimated taking into account a pure solvent viscosity $\eta_s(D_2O, 20°C) = 1.25$ cP[153] according to $\xi_d = k_B T / 6\pi\eta_s D_c$, where k_B is the Boltzmann constant, T is the temperature and η_s is

the viscosity of the solvent. The value of ξ_d is in agreement with ξ from SANS experiment.

Table 4.5: Diffusion parameter D_i, cooperative diffusion coefficient D_c and solvent viscosity η_s of the batch- and feeding-microgels. Fit error of η_s is of the order of 50%.

Sample	η_s, cP	D_i, 10^{-11}m^2/s	D_c, 10^{-11}m^2/s	ξ_d, nm
b-MG$_{0.5}$	3.8	6.3 (0.29)	-	
b-MG$_2$	3.2	2.8 (0.15)	-	
b-MG$_5$	-	-	5.1 (0.1)	3.4
f-MG$_{0.5}$	3.8	2.7 (0.37)	-	
f-MG$_2$	4.6	2.3 (0.54)	-	
f-MG$_5$	4.0	3.7 (0.54)	-	

4.3 Discussion

Structure and dynamics investigation of PNIPAM based microgels reveals a significant influence of the preparation process (i.e. crosslinker distribution within the microgels) and the amount of the used crosslinker and initiator on the microgel features.

4.3.1 Structural inhomogeneities below the VPTT

Addition of the crosslinker to the polymer solution leads to both the formation of the polymer network and the formation of the polymer network inhomogeneities. It was found, that a continuous monomer feeding approach leads to microgels with a correlation length ξ of 7 – 9 nm in the swollen state, while the microgels prepared via batch method have ξ of $\sim$ 4 nm. These values correspond to the microgel mesh sizes reported in literature[4,82,154]. According to obtained exponents of the fractal Porod law in the range of 1.5 – 2.5, the polymers in the network of feeding-microgels behave like Gaussian chains in solution.

The length scale Ξ of f-MG$_x$ microgels, which according to *Shibayama*[35] corresponds to the frozen inhomogeneities within a polymer network, indicates thus the characteristic correlation of the internal domains (or inhomogeneities) and increases with the increasing crosslinker concentration (12.6 nm at 0.5 mol% BIS and $\sim$20 nm at 2 and 5 mol% BIS). In case of the batch-microgels, Ξ is much larger and the tendency is opposite to f-MG$_x$. An increase of the BIS concentration leads to the decrease of the Ξ. With it, can be supposed that crosslinker distribution within feeding-microgel are more uniform in respect to the batch-microgels (it is also obtained above VPTT).

It is interesting to note, that a variation of the initiator concentration does not influence significantly the scattering curves of the microgels with 0.5 mol% BIS at 20°C in the q-range of 0.01 – 0.4 Å^{-1} (Figure 4.5B), i.e. the mesh size is the same for both initiator concentrations (Table 4.1).

A decrease of the C_{IN} by a factor of 10 leads to the bigger microgels (544 nm vs. 265 nm, Table 4.4). Moreover, at higher initiator concentration (b-MG$_{0.5}$), the peak position q^* (Figure 4.5A) corresponds to an inter-microgel distance (a) which are twice as large as the microgel radius obtained from DLS, while for the system b-MG$^*_{0.5}$ with lower initiator concentration this parameter is comparable to the microgel radius (all parameters are presented in Table 4.4). It was assumed, that a lower initiator concentration leads to the formation of the softer microgels, which interpenetrate each other. Such interpenetration effect was also observed by *Mohanty et al.*[22]. The authors showed, that the averaged centre-to-centre distance of the microgels can be smaller than the initial unperturbed particle diameter due to their ability to interpenetrate.

Since at higher initiator concentration the centre-to-centre distance a is close to $2R_{DLS}$, that means the microgels of b-MG$_{0.5}$ behave like hard spheres and only small interpenetration (few nanometers) or compression (both processes are possible) of the dangling ends occurs ($2R_{DLS}$ is slightly larger than a). Our systems have much smaller concentration than reported in the literature[22], nevertheless similar behaviour is observed. Such similarities could be explained by the presence of aggregates in the microgel solution in swollen state, in which microgels behave like a dispersion of high particle concentration.

4.3.2 Internal domains-like structure of microgels above the VPTT

The initial application of the commonly used models (core-shell and fuzzy-shell), which were reported in literature, do not fully describe the experimental scattering data. Therefore SiS model (Eq. 4.1) was applied to the batch-microgels at 50°C.

The SiS model considers two possible scenarios: (i) microgels with two different radii r and R coexist simultaneously, (ii) microgels with radius R consist of smaller spherical domains with radius r. To decide about the right model DLS measurements were performed. It was shown that all systems have only one relaxation mode corresponding to the hydrodynamic radius, which is close to the larger radius R in the SiS model. With this, it was concluded that microgels with radius R consist of the smaller spherical domains with characteristic size r.

All spectra of b-MG$_x$ at 50°C were analysed according to the SiS model with the assumption, that independent of the crosslinker concentration the internal part of the microgel has a domain-like structure. Latter is clearly seen at the lowest BIS concentration,

while an increase of the BIS amount may lead to the denser inner part of the particle and hence, the domains become less distinguishable in SANS experiment. To the best knowledge, such behaviour of the SANS spectrum (especially as for 0.5 mol% BIS) was not observed earlier. For this point could be several reasons. According to *Ikkai* and *Shibayama*[48] the ratio of the outer microgel size to the internal domain size plays an important role in the possibility of phase separation within a single microgel: the bigger the difference in sizes, the clearer the phase separation, i.e. domains become detectable. The other possible reason is a scattering contrast, namely difference in the scattering length density between domain and surrounding ambient. At higher crosslinker concentration the scattering from the microgel surface becomes more dominant (spectrum of the b-MG_5 follows Porod-like decay as shown in Appendix) and domains which intersect or interpenetrate each other become thus not distinguishable in SANS experiment.

Previously reported homogeneous polymer segment distributions within the core part of the core-shell PNIPAM microgels have been also discussed by *Matsui et al.*[76]. The authors show that PNIPAM-based microgels may not always exhibit a uniform surface and may transform into an inhomogeneous raspberry-like structures upon heating. The formation of the internal domains (several tens of nanometers in size) was observed during the microgel collapse. In Ref.[111] with the help of GISANS a domain-like internal structure of the adsorbed PNIPAM microgels was shown. Very recently the presence of the clusters with the higher crosslinker density within PNIPAM microgel were shown in real space using high resolution fluorescence microscopy and dye tagging[53,54]. According to these results, it was concluded that domains remain at 50°C even at higher crosslinker concentration. Moreover, the estimation of the domain concentration within a single microgel also confirms this assumption. From the relation of the scaling components I_1 and I_2 in Eq. 4.1, the number of the spherical domains (N^*) of radius r inside the sphere of radius R was estimated (details of the calculation are presented in Appendix).

Since the volume fraction of the domains ϕ of the batch-microgels with 0.5 mol% and 2 mol% BIS ($< 30\%$, see Table 4.2)) is much smaller than it would be in case of the dense packing of the spherical objects, where the highest volume fraction is 74%[155], no structure factor influence of the internal domains could be detected with SANS, in contrast to the feeding approach which leads to much higher internal domain density.

f-MG_x microgels have a higher density of the inhomogeneities in comparison to the b-MG_x. This requires to consider a structure factor contribution in to the scattering in the collapsed state. Higher BIS concentration leads to the formation of the rough fractal surface with the internal domain-like structure, namely clusters consisting of domains of a radius of 12 – 15 nm. The first term in Eq. 4.1 can be neglected because of the size of

the microgels and the influence of the structure factor contributions from Eq. 2.32. From the very low q-region from the VSANS experiments an agglomeration of microgels was observed, resulting in the large value for the fractal cut off length l of the fractal structures and making it impossible to discern single large microgels.

According to the fit of f-MG_5 at 50°C a fractal structure with the fractal dimensions of 3.2 is formed. Small domains with radius r' of 12.5 nm (corresponding to inner domains with radius r of the b-MG_x) build fractal-like clusters with a characteristic size of 47.1 nm. Such organization is similar to the batch-microgels, i.e. after the deswelling process dense spherical islands are formed even by continuous monomer incorporation.

In case of the lower crosslinker amount (0.5 mol% and 2 mol% BIS) a step-like scattering signal was obtained. Due to the difference in the size of the scattering objects (Guinier analysis) and the slope of the linear range, we conclude, that the systems f-$MG_{0.5}$ and f-MG_2 have similar structures and can be characterized by a fractal-like structure with size >0.4 μm. In turn, these objects consist of the smaller domains with a characteristic size of 15.8 nm (0.5 mol% BIS) and 14.2 nm (2 mol% BIS). The obtained exponents of the scattering power-law are larger than 4. The same tendency was previously reported in Ref.[6,59] and indicates the importance of the surface roughness in the probed q-range[156].

Interestingly, the parameters ξ and Ξ of the system f-MG_2 in the swollen state are approx. equal to the parameters of f-MG_5 (Table 4.3), while in the collapsed state the scattering curves, i.e. the characteristic size parameters of f-MG_2 and f-$MG_{0.5}$ for both microgels are the same (Table 4.1).

It was shown, that an increase of the initiator concentration changes the number of the internal domains within a batch-microgel (Table 4.2). In turn, higher C_{BIS} leads to the denser packing of the microgel and decrease of the contrast between in- and out-domain region. Thus, domains become difficult to distinguish and features of the SANS curves become less pronounced (Figure 4.2A).

Figure 4.7 illustrates the internal structure of the batch- and feeding-microgels according to the structural parameters from SANS experiments. The images illustrate the structure of the microgels and indicates the main difference of the internal domain characteristic sizes at batch and feeding synthesis. In the collapsed state, the domain-like structure of the microgel becomes directly visible. In the swollen state, the internal structure is visible through Ξ and ξ, the complete radial density profile including the low q-region of a dilute microgel solution would reveal a less dense shell as seen in many other publications.

It can be concluded that for all investigated microgels (prepared via batch and feeding method) the inhomogeneous internal structure below and above the VPTT exists, while the parameters and distribution of such domains strongly depend on the preparation

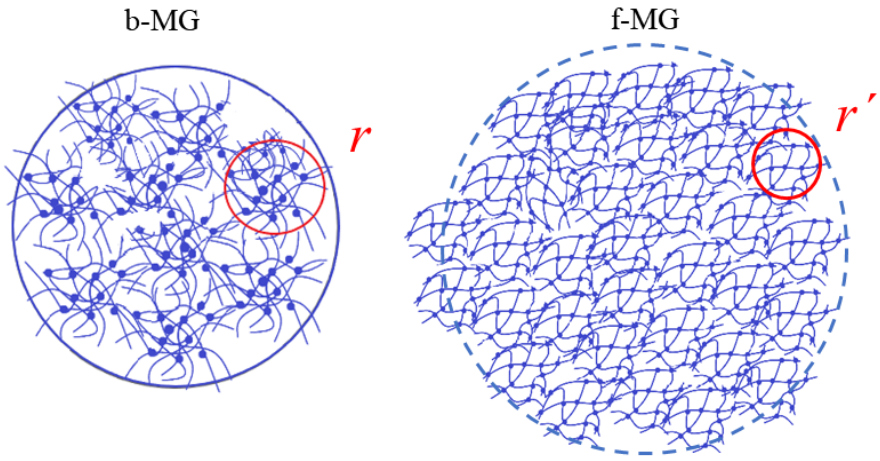

Figure 4.7: Microgel internal structure visualization. In the collapsed state, the sub-domain structure of the microgel becomes directly visible.

process (the way the crosslinker is introduced into the system) and the initial crosslinker and initiator concentration.

4.3.3 Polymer chain dynamics

A study by means of neutron spin-echo spectroscopy reveals that the domain-like internal structure of the microgels and the internal inhomogeneities due to the incorporated crosslinker significantly influence polymer dynamics.

Initially, a model with a non-decaying component $A(q)$ [28,81,126] and a stretching exponent $\beta = 0.85$ was applied to NSE data fit (see Eq. 2.71). The stretching exponent β of 0.85 accounts for the Zimm single chain motions [25] and experimental data were fitted using the Zimm model for the segmental dynamics of the polymers in solution taking into account the contribution from the static inhomogeneities.

Representation of the relaxation rate Γ normalised with q^2 (Γ/q^2) as a function of q allows to identify different dynamic regimes and to estimate a centre of mass diffusion coefficient of the microgels.

Figure 4.8 shows, that the b-MG$_5$ microgel differs from the other investigated systems and parameter Γ/q^2 fluctuates around a constant value in the entire q-range. It indicates that due to the dense polymer and crosslinker distribution in the core region of the microgels cooperative network dynamics dominates. The same behaviour was observable at further increase of C_{BIS} (10 mol% BIS [157]). This is also in agreement with the previous investigation of the PNIPAM systems with 5 mol% BIS [3], where diffusion like density

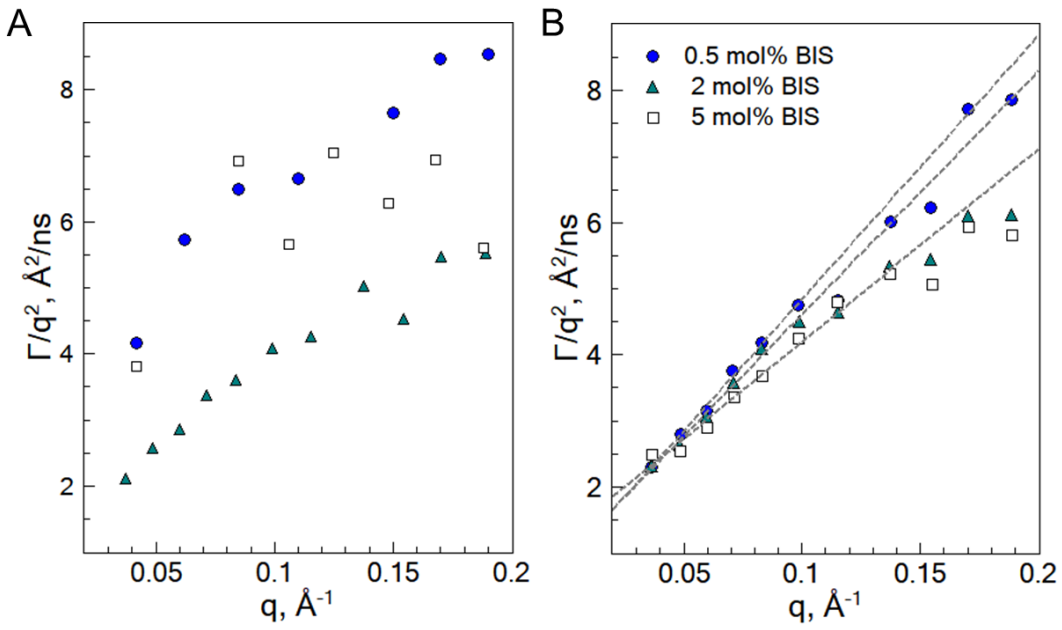

Figure 4.8: A) Γ/q^2 as a function of q for the batch-microgels. B) Γ/q^2 as a function of q for the feeding-microgels. In both figures microgel with 5 mol% BIS is represented with white squares, 2 mol% BIS with cyan triangles and 0.5 mol% BIS with blue circles. Γ was obtained according to fit with Eq. 2.71. Dashed lines indicate the deviation from the single dynamical regime.

fluctuations were observed.

From Figure 4.8, the other microgels investigated in this chapter (except b-MG_5) possess more complex dynamics behaviour. It was found that in low q-range the dynamics deviates from the single-chain motion. Only the batch-microgels with 0.5 mol% BIS possess Zimm-like dynamics over the q-range of the investigation. The same behaviour was previously reported for 0.26 mol% BIS in a PNIPAM gel[5]. The low crosslinker amount and a continuous monomer feeding approach lead to the formation of the fluffy polymer structure, where single chain motion can be observed. Nevertheless inhomogeneous polymer distribution and the presence of the thermal and the frozen fluctuations alter the polymer chain dynamics and their influence becomes non-negligible. Due to the non-monotonous increase of the relaxation rate in the investigated q-range, the superposition of the different types of dynamics is assumed. Independent of the internal crosslinker distribution cooperative motion affects the single-chain dynamics in the presented q-range. Therefore, for the characterisation of the dynamics behaviour of these systems a full Zimm model presented in Eq. 2.67 was applied[43]. The centre of mass diffusion of the whole particle is two orders of magnitude slower and does not contribute significantly in the present time window.

From the analysis with the Zimm model cooperative diffusion coefficient of (2.8 – 6.3)$\times 10^{-11}$m^2/s for the batch-microgel and of (2.3 – 3.7)$\times 10^{-11}$m^2/s for the feeding-microgels were obtained (Table 4.5). The presence of a polymer network with a crowded environment leads to the increase of the solution viscosity compared to the viscosity of D_2O (3.2 – 4.6 cP for microgels vs. 1.25 cP for heavy water). This tendency is in agreement with previous NSE investigations of microgels[28,43,91,157]. At large q (0.17 – 0.19 Å^{-1}) deviations from the Zimm model are observed, whose origin is not yet clear, but seems to be rather diffusive-like. Here we should note, that due to the complex dynamics behaviour, further investigation in a higher q-range are necessary.

It should be noted, that independent of the synthesis route and the crosslinker concentration a pure Zimm-type dynamics was not observed.

4.4 Conclusion

In the current chapter, the influence of the crosslinker distribution due to the different synthesis route (batch and feeding approach), on the internal structure and dynamics of the PNIPAM microgels were studied by means of dynamic light scattering, small-angle neutron and X-ray scattering (in a wide q-range) and neutron spin-echo spectroscopy.

The presence of the inhomogeneous polymer distribution within the microgel below VPTT was found for batch- as well as for feeding-microgels. However the difference in the correlation lengths Ξ and ξ in case of the feeding-microgels is much lower than for the batch-microgels, that indicates a more homogeneous internal structure of f-MG$_x$ rather than for b-MG$_X$. The change of the crosslinker concentration influences the internal correlation parameter in different manner for batch- and feeding-microgels: with the increase of crosslinker concentration Ξ increases in case of f-MG$_x$ systems and decreases in case of b-MG$_X$. In turn, variation of the concentration of the initiator AAPH does not influence the correlation length ξ of the b-MG$_{0.5}$ system at a constant crosslinker amount.

SANS measurements were used to improve the understanding of the inner microgel structure in the collapsed state. The presence of the internal domains inside the individual microgels even at 50°C have been shown. An influence of the crosslinker and the initiator concentration on the internal structure of the microgels above VPTT was obtained. The increase of the initial crosslinker concentration leads to the increase of the internal domain size of b-MG$_X$. The concentration of the initiator influences the fluffiness of the microgel as well as the internal domains. Moreover, an inhomogeneous distribution of the polymer segments above the VPTT with a fractal-like structure was also found for the microgels prepared via continuous monomer feeding approach.

The influence of the crosslinker distribution and its initial concentration within a single microgel on the dynamics of the microgels was observed. While for microgels prepared via feeding approach a segmental dynamics contributes to all crosslinker concentrations, Zimm dynamics was not found even at the lowest crosslinker amount in feeding-microgel, where it was expected. The higher crosslinker concentration in case of the microgels prepared via batch method leads to the denser network and the cooperative dynamics prevails. Polymer interaction with the surrounding environment leads to the increase of the solution viscosity (compared to D_2O viscosity) for all systems.

Chapter 5

Influence of the crosslinker content on adsorbed functionalised microgel coatings*

Abstract

Tunable properties of stimuli-responsive polymer coatings at solid surfaces inspire their application in various electronic devices, as functional tissue in regenerative medicine or for drug release. Especially promising is the exploitation of thermoresponsive poly(*N*-isopropylacrylamide) (PNIPAM) microgels, e.g. as cell-surface adhesion control systems. In this context a morphological and internal structure investigation of thermoresponsive PNIPAM microgels adsorbed on a silicon-surface are presented for the case of low and medium crosslinker content in the microgels. By means of atomic force microscopy, neutron reflectometry and grazing incidence small-angle neutron scattering the swelling behaviour of the adsorbed PNIPAM microgels and the influence of the crosslinker content (*N,N'*-methylenebisacrylamide, BIS) on the polymer layer formation were investigated. The influence of the surface confinement on the responsiveness of the polymer system is discussed.

5.1 Introduction

Responsive polymer systems adsorbed onto solid surface attract a high attention due to their unique properties and wide opportunities for bio-technical and medical applications[15,19–21,46,61–63,65]. Therefore a clear understanding of the properties of the polymer systems at the presence of surface confinement is necessary.

While the bulk properties of the PNIPAM microgels were reported earlier[6,27,58,59,158,159] and detailed investigation of their internal structure is presented in Chapter 4, the understanding of the influence of the surface confinement on the internal structure of the adsorbed PNIPAM microgels is still limited.

In order to study the morphological and structural properties of the PNIPAM microgel at the presence of the solid surface, atomic force microscopy, neutron reflectometry and grazing incidence small-angle neutron scattering were used. Main focus of this chapter is

*Similar content is presented in T. Kyrey, J. Witte, V. Pipich, A. Feoktystov, A. Koutsioubas, E. Vezhlev, H. Frielinghaus, R. von Klitzing, S. Wellert, O. Holderer, Influence of the crosslinker content on adsorbed functionalised microgel coatings, Polymer (2019) 169, 29 – 35, doi: 10.1016/j.polymer.2019.02.037.

addressed to the investigation of the PNIPAM microgels prepared via classical precipitation polymerisation (batch synthesis) with low and medium crosslinker content (BIS: 0.5 and 5 mol%) at temperatures below and above the volume phase transition. The influence of the confinement and the crosslinker content on (i) the thermoresponsiveness, (ii) the morphology and (iii) the internal structural inhomogeneities of the polymer layers at silicon interface are studied.

5.2 Results

5.2.1 Morphological characterisation of the adsorbed microgels

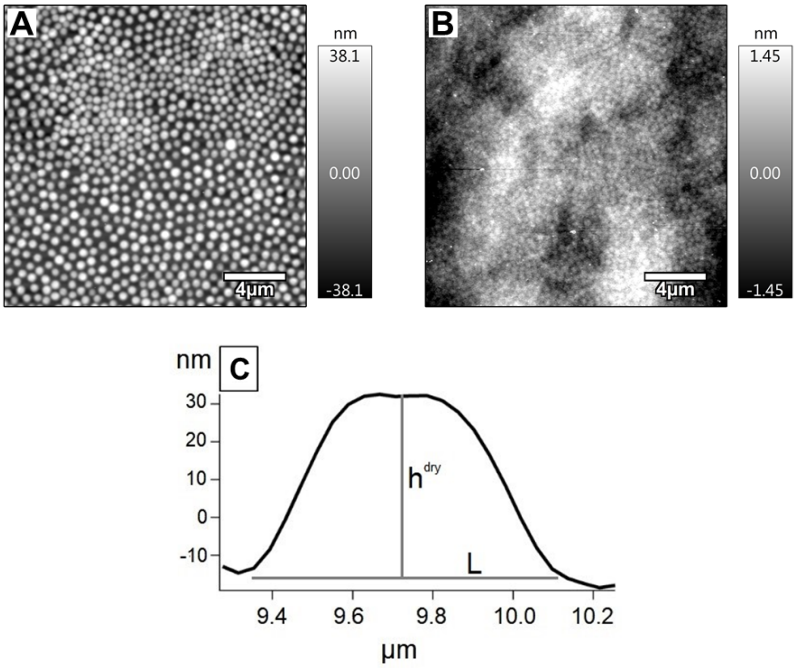

Figure 5.1: A) AFM image of adsorbed Ab-MG_5, B) AFM image of adsorbed Ab-$MG_{0.5}$, C) profile of the single microgel of Ab-MG_5. The samples were scanned at room temperature under dry conditions. Scan area is 20×20 μm^2.

Initial characterisation of the microgels after adsorption was performed with AFM. The AFM images of Ab-MG_5 and Ab-$MG_{0.5}$ as well as the cross section of an individual microgel in dry state are presented in Figure 5.1. The AFM image of Ab-MG_5 measured against water shows the same microgel distribution on local scales (Figure 5.2), while for Ab-$MG_{0.5}$ no individual microgels were detected.

At higher crosslinker concentration the individual microgels are clearly visible on the Si-surface (Figure 5.1A). Here regions with different microgel-microgel distances were

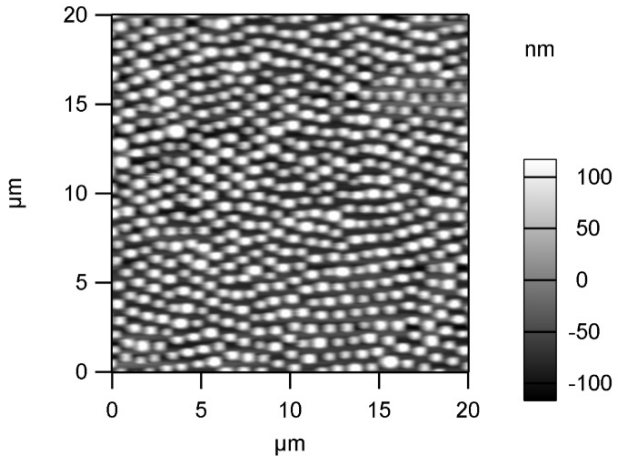

Figure 5.2: AFM image of adsorbed Ab-MG_5 scanned at room temperature in the swollen state under water environment.

observed.

In case of Ab-MG_5 a total number of 459 individual microgels was analysed (edge microgels were ignored) and the following geometrical parameters were obtained: (i) the height of the microgel in dry and wet state, $h_{dry} = (39.1 \pm 7.5)$ nm and $h_{wet} = (120 \pm 57)$ nm, respectively, (ii) the averaged width, $L_{AFM} = (507 \pm 102)$ nm (corresponds to the L in Figure 5.1C).

In contrast to Ab-MG_5, the individual microgels of the Ab-$MG_{0.5}$ were barely indistinguishable from the solid surface due to the small height (Figure 5.1B).

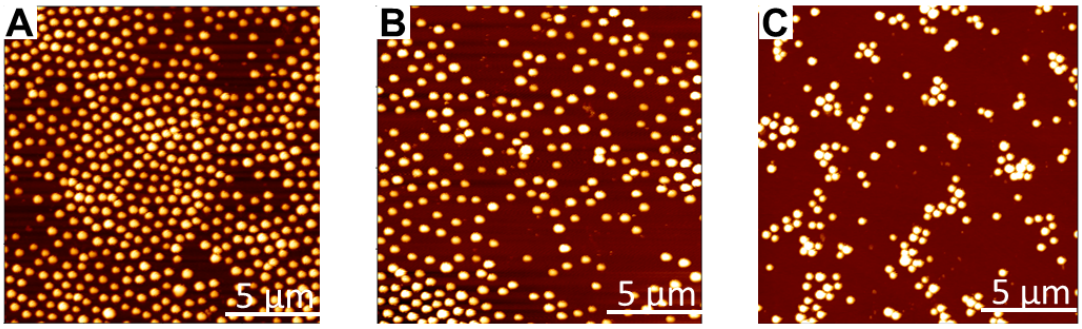

Figure 5.3: AFM image of the Ab-MG_5 adsorbed on Si-block (5×8 cm^2) collected from different block region: A – centre region, B – somewhere in-between and C – edge region. AFM measurements were performed by M. Kühnhammer.

Figure 5.3 exemplarily depicts an AFM image obtained from different parts of Si-block with Ab-MG_5 coating. It should be noted, that microgel deposition on a small wafer (2×2 cm^2) used in AFM experiment is more controllable and microgel distribution on the wafer surface is homogeneous, whereas coating of the Si-blocks (5×8 cm^2) used for neutron

experiments is more difficult to control. Therefore, different microgel densities along the Si block were observed.

5.2.2 Depth probing of the microgel structure by NR

To characterize the structure of the adsorbed microgels perpendicular to the surface a neutron reflectometry experiment was performed. NR-profiles of the reflectivity curves in Figure 5.4A clearly indicate a difference in adsorbed polymer microgels with 0.5 mol% and 5 mol% of BIS.

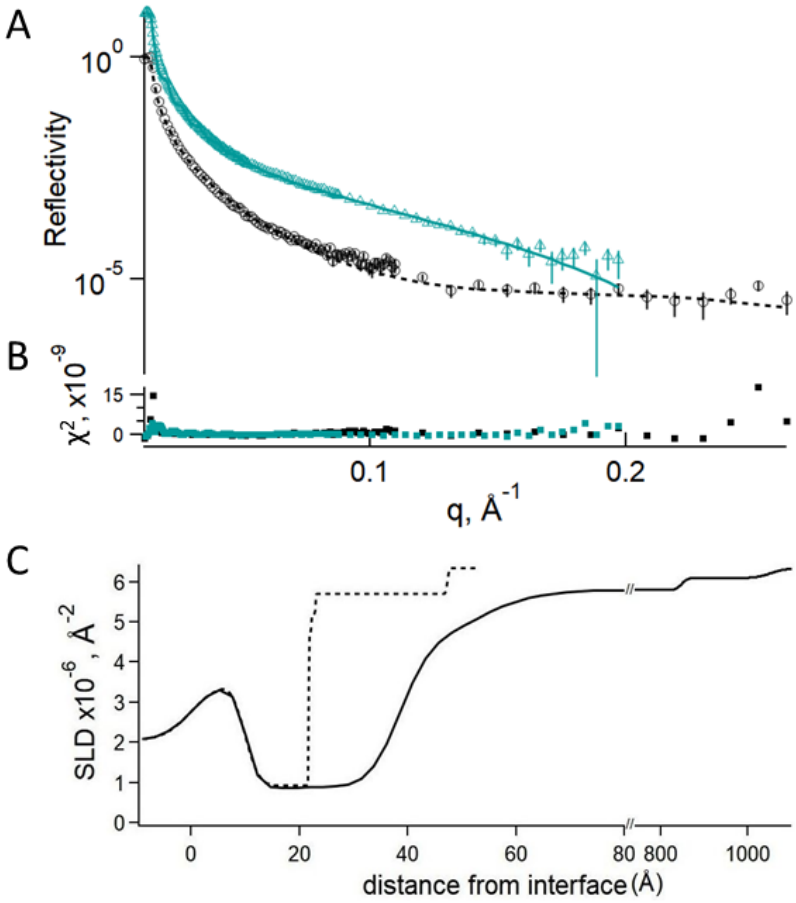

Figure 5.4: A) Reflectivity curves of the adsorbed microgels cross-linked with 0.5 mol% BIS (Ab-$MG_{0.5}$ – black circles) and 5 mol% BIS (Ab-MG_5 – cyan triangles) measured against D_2O at 20°C. For better visualisation the reflectivity spectra of Ab-MG_5 was scaled by one order of magnitude. Solid line and dotted line correspond to the best fit of systems with 5 and 0.5 mol% BIS respectively. B) Fit quality is demonstrated via χ^2. C) SLD profiles corresponding to the fit curves: Ab-$MG_{0.5}$ – dotted line, Ab-MG_5 – solid line.

To characterise the polymer distribution in the direction normal to surface, the scattering length density (SLD) profile was reconstructed with the Motofit[116] software package.

The following assumptions were made: each layer component, including microgels, was represented as a single layer. Si block and water layer were simulated as a sub-layer with an infinite thickness. The SLD of silicon and D_2O ($\rho_{Si} = 2.07 \cdot 10^{-6}$ Å^{-2}, $\rho_{D_2O} = 6.34 \cdot 10^{-6}$ Å^{-2}) as well as roughness of Si-surface ($\phi = 4$ Å) were fixed. Layers of SiO_2 and PEl were considered as a single layer with thickness of 10 Å and roughness of 3 Å. As free parameters the SLD, roughness and thickness of the polymer layer were used.

According to the AFM results one has to deal with a distribution of microgel sizes, microgel shape and coating density as well as possibly with an internal gradient of the SLD from the core to the outer part of the microgel. Therefore, an iterative fitting has been applied to the experimental data (Figure 5.4A).

The first layers described above were fitted alone in a first step (with the SLD determined mainly from the high-q behaviour). Then thick polymer layers with the averaged SLDs (ρ_{layer}) were added successively as long as the quality (χ^2) of the fit was still improving. The SLD in this layer was calculated as $\rho_{layer} = x\rho_{PNIPAM} + (1 - x)\rho_{D_2O}$, with the polymer amount (x) in the range from 20% to ∼1% in the layer. With this iterative fitting, the systems Ab-$MG_{0.5}$ and Ab-MG_5 were modelled with three and four polymer layers, respectively.

According to the obtained SLD profiles (Figure 5.4B) in case of Ab-$MG_{0.5}$ the water content in the direction normal to the surface increases sharply and a thin polymer layer of ∼30 Å is obtained. Moreover, 30% of the hight of the adsorbed microgel has an SLD of $0.93 \cdot 10^{-6}$ Å^{-2} and the rest has an SLD of $5.7 \cdot 10^{-6}$ Å^{-2}. It means, that polymer layer in the vicinity of the solid surface has a content of 3% water, whereas the outer layer is water-rich with a 90% of water.

The Ab-MG_5 profile has a more complex structure: directly at the solid surface a thin polymer layer of ∼30 Å with a negligible water content is formed. Then, in contrast to Ab-$MG_{0.5}$, water amount gradually increases further away from the surface. Since at 20°C the polymer is in the swollen state and a high amount of water molecules is within the microgel. The microgels are in a water environment and hence, the averaged SLD of the layer is altered. Therefore, a thick polymer layer of ∼800 Å with a SLD of $5.8 \cdot 10^{-6}$ Å^{-2} was obtained. The thickness of the microgel layer is in agreement with the height from AFM.

A rather dense polymer layer strongly adsorbed at the substrate has been found for both samples with reflectometry at large q, with a rather flat surface for Ab-$MG_{0.5}$ and a smoother polymer-water transition for Ab-MG_5. This confirmed the AFM results.

5.2.3 Structure of the adsorbed microgels: GISANS

Internal microgel structure

Lateral arrangement and internal structure of the adsorbed microgel systems Ab-$MG_{0.5}$ and Ab-MG_5 were studied below and above the VPTT by means of GISANS. To probe the internal structure of the batch-microgel a q-range of 10^{-3} – $2 \cdot 10^{-2}$ Å^{-1} was chosen. Figure 5.5 represents 2D-detector images of the microgels at 20°C.

To characterise the internal structure of the PNIPAM microgels in lateral direction, line cuts of the 2D detector images at q_z corresponding to the Yoneda peak were performed. Such q_z was chosen due to the unique properties of the scattering at the Yoneda peak position, which corresponds to the critical angle of total reflection (α_c). Here the lateral scattering intensity increases and maximal information can be achieved[108].

In Figure 5.6 the horizontal line cuts of the 2D GISANS data for Ab-$MG_{0.5}$ and Ab-MG_5 in the swollen and collapsed state are presented. For better visualisation data at 50°C were multiplied by a factor of 10. The dashed lines represent fits according to Eq. 2.60. By means of the mesh model the characteristic correlation length ξ_s and the size of the inhomogeneities Ξ_s for both systems were determined with Eq. 2.60.

The temperature increase does not alter the shape of the line cuts and therefore there is no change of the correlation lengths. The obtained correlation lengths ξ_s is 5.7 nm and 4.7 nm for Ab-$MG_{0.5}$ and Ab-MG_5, respectively, and Ξ_s is 23 – 24 nm for both systems.

Lateral ordering of microgels on surface

To characterise the lateral ordering of the microgels on the Si-surface, GISANS measurements in the low q-range were performed. In Figure 5.7 the horizontal line cuts of the 2D-detector images for Ab-$MG_{0.5}$ and Ab-MG_5 at 20°C and 50°C are presented. While for the system with 0.5 mol% BIS an increase of the intensity with the temperature is observed, in case of Ab-MG_5 an additional peak appears above the VPTT at $q_y = 7.8 \cdot 10^{-4}$ Å^{-1}. The low intensity and smearing of this peak have been attributed to the distribution of the microgels on the solid surface. Due to the adsorption of the microgels onto the solid surface via spin-coating, the inter-microgel distances are shorter in the central region of the block, while on the edges of the block they are larger (see Figure 5.3).

In real space, the position of the peak maximum corresponds to a characteristic length of $d \approx 805$ nm. Taking into account the microgel parameters from the AFM measurements, the parameter d has been attributed to the center-to-center distance between the individual microgels. There are two possible explanations of the peak appeared above the VPTT. First, free dangling ends of neighbouring microgels can intersect with each other in the

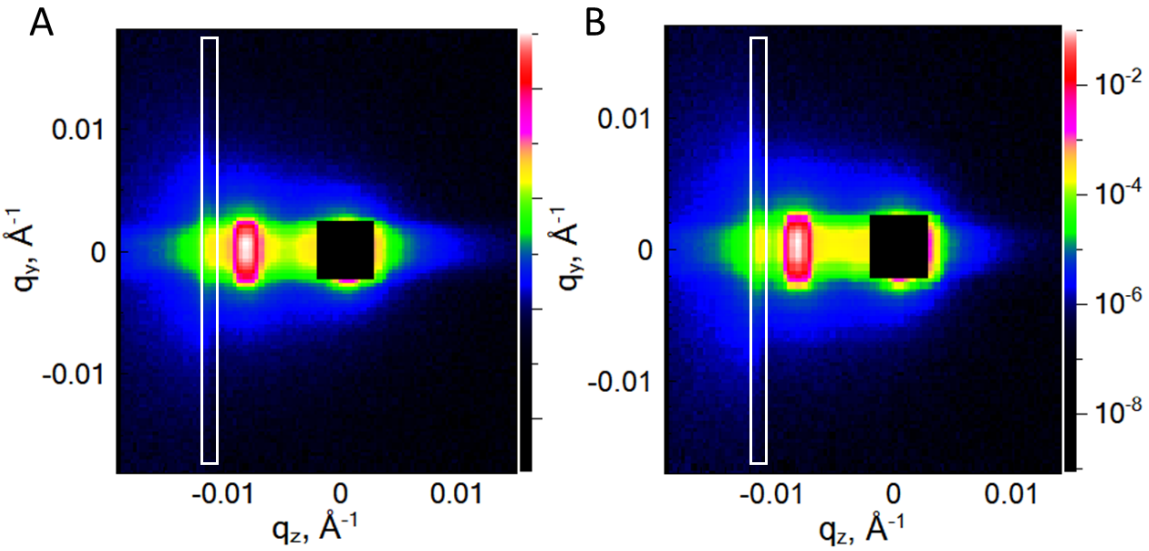

Figure 5.5: 2D GISANS data of the system Ab-$MG_{0.5}$ (A) and Ab-MG_5 (B) at 20°C. White rectangles indicate the positions at which line cuts were performed for the further microgel structure characterisation in lateral direction.

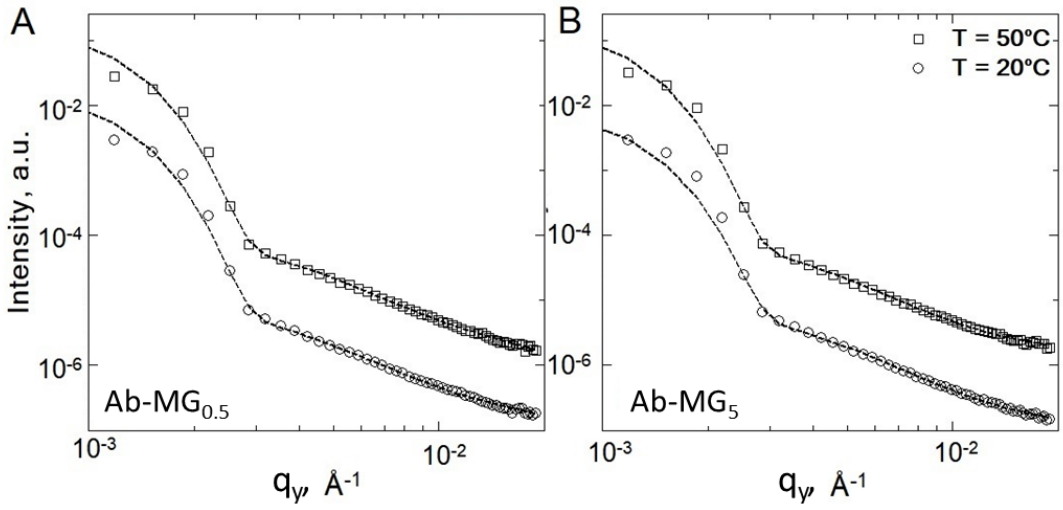

Figure 5.6: Horizontal line cuts of the 2D GISANS data of the PNIPAM batch-microgels crosslinked with 0.5 mol% BIS (A) and 5 mol% BIS (B). The dashed lines represent fits according to Eq. 2.60. The curves were shifted along the Y-axis for the clarity.

swollen state. It smears out the outer contour of the individual microgel below the VPTT, and becomes visible above VPTT, when the related polymer chains collapse. In case of the layers with mean inter-microgel distances much larger than the mean microgel lateral distance (non-dense packing) such chain intersection is negligible. Moreover, the first explanation is unlikely due to the strong confinement of the dangling ends.

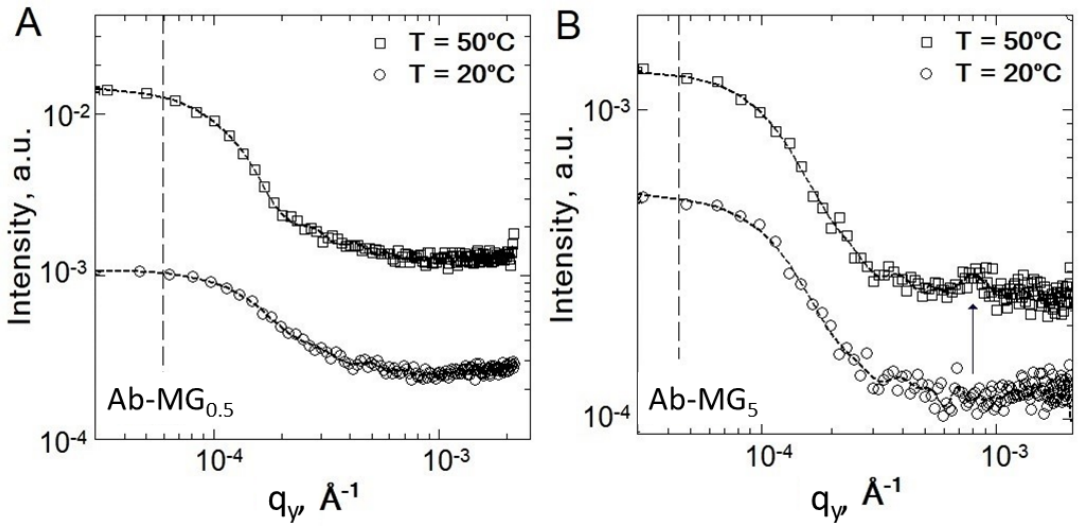

Figure 5.7: Horizontal line cuts of the 2D intensity distribution of the system Ab-$MG_{0.5}$ (A) and Ab-MG_5 (B) at temperatures above and below VPTT. The curves were shifted for the sake of clarity. Lines are the guides for the eye. The vertical dashed line indicates the resolution limit. Errors are <15% in the whole q-range.

The second explanation is based on the PNIPAM transition from hydrophilic to less hydrophilic across its VPTT. Below the VPTT the PNIPAM microgels are in the swollen state, thus a high amount of water within the microgel decreases the scattering contrast between microgels and bulk water and only after the temperature increase and water expulsion the collapsed microgels become detectable in GISANS experiments.

In case of the system Ab-$MG_{0.5}$, the microgels present a layer-like structure at the Si-surface and even an increase of the temperature does not lead to the microgel separation.

5.3 Discussion

The investigation of the adsorbed PNIPAM microgels Ab-$MG_{0.5}$ and Ab-MG_5 with AFM, NR and GISANS provided the structural information at different length scales. The comparison of the microgel parameters in bulk and in adsorbed state are presented in Table 5.1 (details of DLS and SANS measurements were presented in Chapter 4).

It was found, that the main difference in film quality is in the ability to arrange the separated microgels on the solid surface. The crosslinker concentration influences the stiffness and deformability of the microgels[72]. Initially, in the swollen state the bulk PNIPAM microgels possess a core-shell-like structure with a crosslinker gradient from the core with a high polymer density to a loosely crosslinked outer shell[6,20]. At low crosslinker concentration (0.5 mol%) fluffy microgels are formed and the adsorption process leads

Table 5.1: Radii of the microgels measured with DLS (R_{DLS}) and SANS (R), the radius of internal microgel domains r according to SiS model presented in Chapter 4, the mesh size of the polymer network and characteristic size of inhomogeneities in bulk (ξ, Ξ from SANS) and in the adsorbed state(ξ_s, Ξ_s from GISANS) and parameters of the individual microgel, namely width of adsorbed microgel L_{AFM} from AFM. In parentheses standard deviation is indicated. All parameters were measured at 20°C and are presented in nm. Errors are <1%, otherwise are presented in parentheses.

System	R_{DLS}	R	r	Ξ_s	Ξ	ξ_s	ξ	L_{AFM}
Ab-$MG_{0.5}$	265	-	28.6	22.7	170	5.7	3.5	-
Ab-MG_5	350	136.6	33.2	23.9	82.6	4.7	3.6	507.1 (102.5)

to strong deformations of the microgels perpendicular to the substrate surface with the formation of a layer-like structure. At 5 mol% of crosslinker the microgels possess a distinct inhomogeneous structure and in the adsorbed state at a Si-surface individual and clearly separated microgels are observed (Figure 5.1).

In the adsorption process, microgels are immobilised at the surface due to the attractive polymer-surface interaction. The polymers are compressed normal to the surface ($h_{AFM}/R_{DLS} \approx 0.3$) and stretched in the lateral direction ($L_{AFM}/R_{DLS} \approx 1.45$), which results in the increase of ξ_s as compared to the mesh size in the bulk (see Table 5.1). Due to the compression, the volume of the adsorbed Ab-MG_5 microgels decreases by one order of magnitude as compared to the microgels' volume obtained from DLS and is comparable to the volume from the SANS experiment: $V_{AFM}/V_{DLS} \approx$ 1:10, $V_{AFM}/V_{SANS} \approx$ 1:1.

Thus, in case of Ab-MG_5 the denser core of the microgels constitutes the main part in the adsorbed state, whereas the shell of Ab-MG_5 as well as the much fluffier microgels of Ab-$MG_{0.5}$ undergo strong adhesion toward the surface and acquire a flat layer-like structure with partially overlapping of the polymer chain segments.

Such differences in layer formation are also in good agreement with the theoretical predictions. According to *Vilgis et al.*[73] the adsorption behaviour of the microgels is determined by the gain in energy under surface contact that leads to the microgel spreading and deformation to some extent. The maximum gain would be achieved if all polymer chains are adsorbed, but simultaneously it would lead to a high penalty in elasticity[47]. This deformability strongly depends on the molecular weight of the chains and becomes large for weakly crosslinked microgels. Therefore, at higher crosslinker concentration microgels of Ab-MG_5 possess a fried-egg-like structure and the well-defined individual microgels are observable. In case of Ab-$MG_{0.5}$, the amount of crosslinker is small and adsorption of the polymer chains is not accompanied by a high penalty in elasticity and a more fluffy

structure of Ab-$MG_{0.5}$ undergoes larger deformation. It leads to the overlapping of the PNIPAM chains from neighbouring microgels and the formation of the layer-like structure.

The different types of the adsorbed microgels in the swollen state (individual microgels at 5 mol% BIS and smoothed layer at 0.5 mol% BIS) are also in agreement with the results of the neutron reflectometry experiments. It was shown that the scattering length density (SLD) profile in case of Ab-$MG_{0.5}$ has a step-like shape, that corresponds to the layer-like structure with a sharp transition to the water interface. In contrast, the SLD profile of Ab-MG_5 indicates a gradual increase of the water content in the polymer layer from the Si-surface.

The AFM images of Ab-$MG_{0.5}$ are very smooth and an identification of the individual microgels is not possible. The application of GISANS allows the detection of the internal structure and characteristic correlation lengths of the microgel independent of the crosslinker concentration. The line cuts through the 2D intensity pattern provide the component of the correlation length ξ_s parallel to the interface. The obtained correlation lengths of the polymer network in the adsorbed state ξ_s are slightly larger than in the bulk (ξ). The GISANS experiments further revealed the existence of frozen inhomogeneities with a length scale Ξ_s of 22.7 nm and 23.9 nm for microgel with 0.5 and 5 mol% BIS, respectively. The presence of the characteristic domains within the microgels in bulk was demonstrated in Chapter 4 and was also recently confirmed by *Matsui et al.*[76] in the adsorbed state. They showed that during a temperature increase the microgels gradually contract, whereas domains of several tens of nanometers in size are present inside. The finding is in agreement with the values of Ξ_s obtained in our experiment. These domains persisted near the VPTT and did not disappear above the VPTT. It should be noted, that in swollen state the internal inhomogeneities Ξ_s of the adsorbed microgels is smaller then this parameter in bulk (Ξ), however Ξ_s is close to the size of the internal domains in collapsed state r obtained with SiS model in Chapter 4 (see Table 5.1). Speculatively, the adsorption process as well as the temperature increase leads to the collapse of the internal structure of the microgels and to decrease of the internal inhomogeneities.

A further point of interest is that the correlation length ξ_s as well as the characteristic size of the inhomogeneities Ξ_s are independent of the temperature in the adsorbed state, i.e. they remain constant above and below the VPTT for both systems (obtained values of ξ_s and Ξ_s at 20°C and 50°C do not differ, therefore were not presented separately). Consequently, the strong microgel-surface interaction makes it hard to change the correlation lengths and so the internal structure of the adsorbed microgels in the vicinity to the surface. Similar behaviour was recently reported for PNIPAM-co-AAc and PEG based microgels[75,129,160].

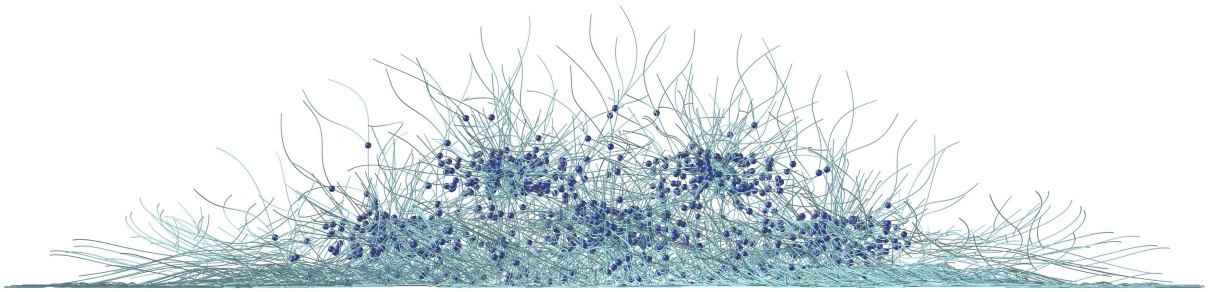

Figure 5.8: Model of the adsorbed microgel. The solid lines represent linear polymer chains, the cross-links are represented by the blue spheres.

Figure 5.8 sketches a microgel in adsorbed state with the characteristic internal density fluctuations and the waterless microgel layer in the vicinity to the Si-surface as in case of microgel with 5 mol% of crosslinker.

5.4 Conclusion

Using the combination of atomic force microscopy, neutron reflectometry and grazing incidence small-angle neutron scattering over a wide q-range allows detailed characterisation of the lateral arrangement of the adsorbed microgels in dependence on the crosslinker content and the temperature.

While polymer-surface and microgel-microgel interactions determine the layer formation, the strong influence of the crosslinker content on the surface structure of the microgel layer was obtained. Higher crosslinker concentration leads to the lower deformability of the microgels and the well-defined individual microgels on the solid surface were formed, while at 0.5 mol% of crosslinker the fuzzy microgels formed the layer-like structure.

In terms of the thermal fluctuations and static density or frozen inhomogeneities the characteristic correlation lengths ξ_s and Ξ_s were determined. Strong influences of the solid surface on the properties of the adsorbed microgels were observed. Due to the adsorption process, the mesh parameter ξ_s increases as compared to the bulk by $\sim$23% and $\sim$40% in case of Ab-MG_5 and Ab-$MG_{0.5}$, respectively. The much flatter conformation of the microgels with lower crosslinker content leads to a larger correlation length.

Moreover, the surface confinement strongly affects the temperature behaviour of the adsorbed microgels, namely the temperature increase does not lead to any significant structural changes of the microgels in lateral direction independent of the crosslinker content.

Chapter 6

Modelling and interpretation of the evanescent wave scattering

Abstract

Grazing incidence small angle neutron scattering (GISANS) and grazing incidence neutron spin-echo spectrometry (GINSES) are powerful experimental methods for investigation of structure and dynamics of the adsorbed polymer systems (microgels, brushes, microemulsions, etc.). Neutron scattering provides access to the internal dynamics. Combination of neutron spin-echo spectrometry with grazing incidence geometry opens the possibility to probe dynamics of the polymer system in vicinity to the solid substrate in the time range up to 100 ns. In turn, the usage of the GINSES technique has some peculiarity and, due to the novelty of the method and complexity of the scattering geometry, difficulties in further data analysis appear.

In the current work it is presented how simulations within the Distorted Wave Born Approximation (DWBA) with the BornAgain software package can be used for GINSES and GISANS data treatment and for the preparation to the experiment under grazing incidence conditions. Simultaneously, it is reported on the possible challenges and reefs appearing in choosing the best model and the "wrong" understanding of the roughness parameter. With two showcase examples (a PNIPAM-brush and a PEG-microgel adsorbed on Si-surface), the simulation process as well as the application of the simulations to the GINSES data analysis are presented.

6.1 Introduction

This chapter aims at handling the peculiarities arising at the investigations of thin polymer systems in the vicinity of the solid interface.

As mentioned in Section 2.2 grazing incidence neutron scattering is a powerful non-destructive tool that provides in-situ and in-operando access to the intrinsic properties of the adsorbed polymer systems (microgels, brushes, microemulsions, etc.)[90,92,111,112]. While grazing incidence small-angle neutron scattering (GISANS) is a widely used technique that allows accessing of the internal lateral structure of the polymer system adsorbed at a solid surface or at a water/oil interface[72,128–132], a combination of neutron spin-echo spectroscopy with grazing incidence geometry allows to probe dynamics of the polymer

system in vicinity of the solid substrate in the time range up to 100 ns[78,91,94,133]. However, due to the novelty of the GINSES method and complexity of the scattering geometry, further data analysis and dynamics characterisation is the challenging task.

In this chapter, the simulations in the framework of the Distorted Wave Born Approximation (DWBA)[118] performed with BornAgain software package[149] are proposed as a auxiliary tool, served for the optimisation of the experimental set-up under grazing incidence conditions and the further GINSES and GISANS data treatment. Such questions as background correction, scattering intensity distribution, contribution from compositional layers of the sample to the general scattering signal etc. are addressed. Simultaneously the possible challenges and reefs appearing in the selection of the best model and the erroneous understanding of the roughness parameter are discussed.

While GINSES experiment on adsorbed PNIPAM microgels, as well as GINSES experiment in general, would require justified and proven strategies in experiment performance and further analysis, in this chapter the simulation process (including problems and questions mentioned above) as well as the application of the simulations to the GINSES data analysis are tested on the two showcase examples: a PNIPAM-brush and a PEG-microgel adsorbed on Si-surface.

Since the simulation process and the model design require initial collection of the structural parameters of the system under interest, in section 6.2 of this chapter the results of the structure investigations of the adsorbed PEG-microgel with neutron reflectometry and GISANS are presented. Additional AFM measurements reported in Ref.[70] have been used as an input to the scattering simulations, which are presented in Section 6.3.

6.2 Experimental results: Initial characterisation of the PEG-microgel structure*,†

6.2.1 PEG-microgel composition

Ethylene glycol based (PEG)-microgels presented in this chapter consist of the monomer 2-(2-methoxyethoxy)ethyl methacrylate (MeO_2MA), the comonomer poly(ethylene glycol) methyl ether methacrylate (OEGMA), and the crosslinker ethylene glycol dimethacrylate (EGDMA) and have been synthesized via precipitation polymerization[161,162]. Detailed description of the preparation process can be found in Ref.[91]. The sample presented here has 5 mol% of comonomer. The amount of the cross-linker was set to 3 mol%. The sample is designated as p-ME_3O_5.

6.2.2 Depth probing of the PEG-microgel

To characterise the polymer density profile of the adsorbed microgel vertical to the substrate neutron reflectometry measurements were performed at the angle dispersive reflectometer NREX$^+$ (with neutron wavelength of 4.28 Å). Figure 6.1A shows the Fresnel normalized reflectivity curves as well as corresponding scattering length density profiles of p-ME_3O_5 at temperatures below (15°C) and above (60°C) the VPTT of the microgels.

At 60°C the reflectivity data shows only extremely smeared oscillations with a small amplitude and a broad peak at higher q. The peak is attributed to the inner densely cross-linked core region of the adsorbed microgels. This core has a height of about 50 nm and is surrounded by the fluffy, less crosslinked polymer shell. The total height of the microgel layer is about 150 nm. This agrees with the previous observations in AFM measurements on selected isolated microgels[70]. At high q values the film roughness leads to a linear decrease of the normalized signal.

From the difference in the SLD profiles measured at 15°C and 60°C (Figure 6.1B) a slight increase of the core thickness with temperature due to the collapse of the polymer network of the microgels and a decrease of the shell SLD at higher temperature due to water expulsion can be concluded. It should be noted, that the thermoresponsiveness is preserved in the adsorbed state but the swelling ability is significantly limited compared to the bulk[163]. Speculatively, this can be attributed to a strong adhesion of the dangling

*Similar content is presented in T. Kyrey, M. Ganeva, K. Gawlitza, J. Witte, R. von Klitzing, O. Soltwedel, Zh. Di, S. Wellert, O. Holderer, Grazing incidence SANS and reflectometry combined with simulation of adsorbed microgels, Physica B: Condensed Matter (2018) 551, 172-178, doi: 10.1016/j.physb.2018.03.049.

†NR and GISANS experiments on PEG-microgel were performed by K. Gawlitza.

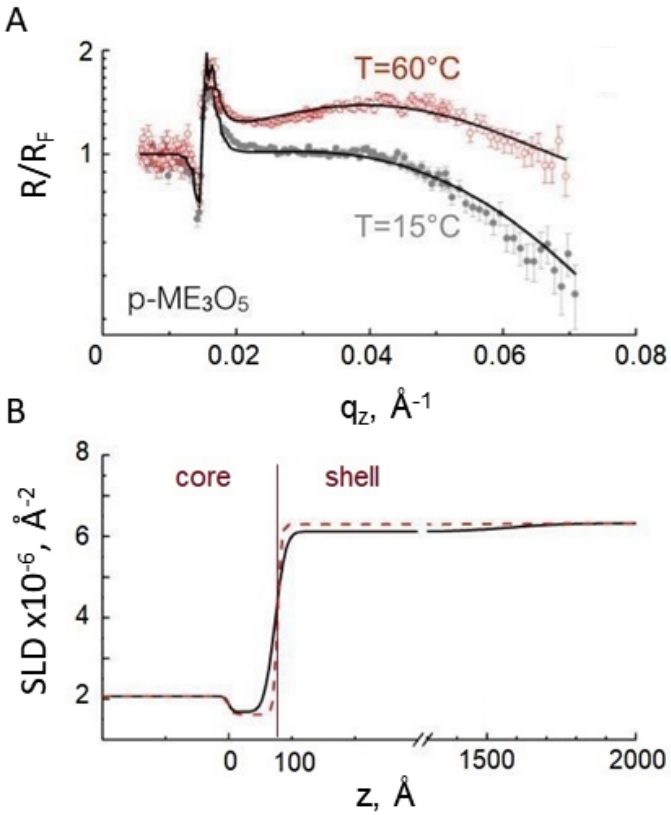

Figure 6.1: A) Fresnel normalized reflectivity curve of the p-ME_3O_5 at 15°C (grey) and 60°C (red). The solid lines are fits to the data. B) Corresponding scattering length density profiles of p-ME_3O_5 at 15°C (black solid line) and 60°C (red dashed line). For better visualization a break between 300 Å and 1300 Å was inserted. The red vertical line depicts imaginary boundary between core and shell part.

ends of the polymer network to the substrate which occurs via hydrogen bonds.

6.2.3 Internal network correlations

The network correlation length of the PEG-microgels was studied with GISANS. Measurements were performed at the KWS-2 instrument. Sample-to-detector distances of 8m and 4m and a neutron wavelength of 5 Å were used. An angle of incidence (α_i) of 0.7°, which is above the critical angle of the total external reflection of the PEG-microgel, was chosen to probe the structure of the entire layer of microgel. Further experimental details can be found elsewhere[129].

Figure 6.2 represents the 2D scattering signal of PEG-microgel at 20°C as well as a horizontal line cut at the position of the Yoneda peak (q_z = 0.017 Å^{-1}) with the corresponding fit curve.

At low q the resolution function determines the intensity distribution. This contribution was fitted with a Gaussian function as described with the first term of Eq. 2.60. In the range $q > 0.015$ Å^{-1}, where the diffuse scattering dominates, the intensity was fitted with a Lorentzian function which describes the lateral Ornstein-Zernike contribution to the wings of the Yoneda peak.

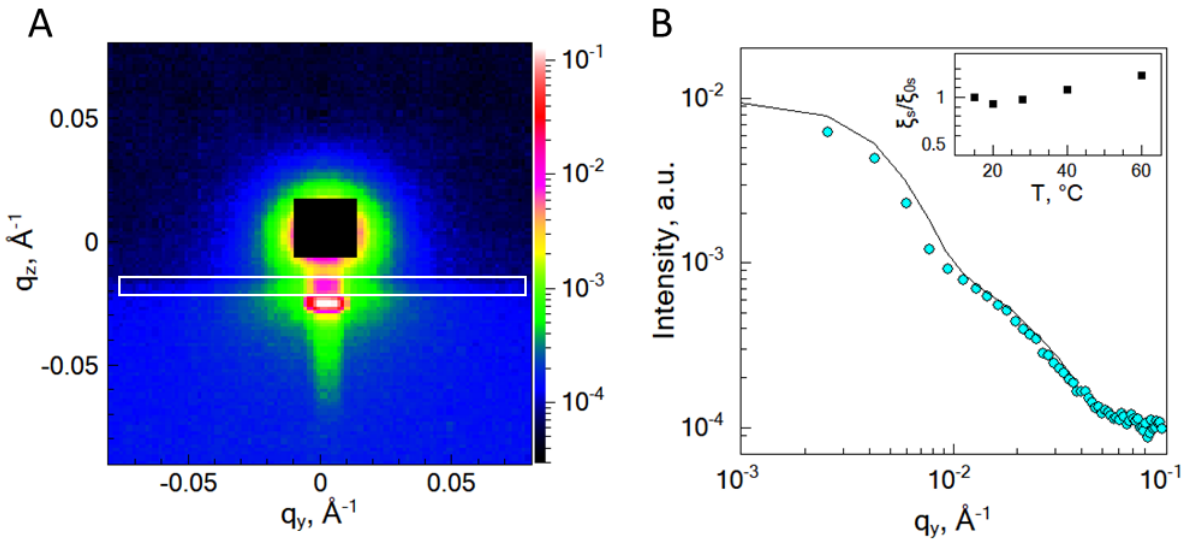

Figure 6.2: A) 2D scattering pattern of PEG-microgel at 20°C. White rectangle determines the position of the line cut used for further microgel network characterisation. B) Horizontal line cut of the 2D GISANS data (cyan circles) at the position of the Yoneda peak and the corresponding fit curve (black line). Inset shows temperature dependence of the correlation length ξ_s normalised to ξ_{0s}, where ξ_{0s} is the correlation length at the 15°C.

From the fit the correlation length of 5.7 nm was obtained. It is pertinent to note that within the precision of the experiment, the correlation lengths ξ_s remain constant and independent of the temperature. The similar behaviour was observed for the adsorbed PNIPAM-microgels in Chapter 5 and was also reported for PNIPAM-co-AAc microgels adsorbed at a silicon surface[75].

According to the theoretical predictions, the correlation length of the thermal network fluctuations diverges when approaching the critical point of the volume phase transition. This was the case, for example, for PNIPAM macrogels[164] and PNIPAM microgels at crosslinker densities below 15 mol%[4]. However the strong attractive interaction with the confining substrate and the reduced deswelling in lateral direction could suppress this divergence for surface adsorbed microgels and hence, no critical behaviour can be observed.

6.3 Simulations within frames of DWBA‡

All simulations presented here were performed in the framework of the Distorted Wave Born Approximation with BornAgain software package[149]. BornAgain is an open-source multi-platform framework for simulation and fitting of the grazing incidence small-angle scattering and reflectometry data.

Parameters of the PEG-microgel and PNIPAM-brush used for the model development are in agreement with the previous investigation presented in Section 6.2 and Ref.[70,163,165]. The simulation takes into account the instrument resolution, layer roughness and the absorption contribution of each component. The simulated geometry of the experiment corresponds to the geometry of a real experiment (neutron beam penetrates sample through the Si block). The scripts for exemplary BornAgain simulations are presented in Appendix.

6.3.1 Polymer system models and their peculiarities

PEG-microgel model

The PEG-microgels are modelled as truncated spheres placed on a Si substrate and buried into D_2O. Among parameters mentioned above, this simulation takes also into account the size distribution of the microgels and contribution from specular reflection. SLD and roughness for p-ME_3O_5 have been obtained from the NR measurements (Section 6.2). The mean radius and height of the microgels and full width at half maximum (FWHM) of the size distribution[166] have been taken from the AFM measurements[70]. To account for the effect of the density fluctuations, the form factor has been represented as a sum of the form factor due to the scattering from the microgel shape $F_p(q)$ and the Ornstein-Zernike form factor related to the internal thermal fluctuations:

$$F(q) = AF_p(q) + \frac{B}{1 + \xi_{xy}^2(q_x^2 + q_y^2) + \xi_z^2 q_z^2} \tag{6.1}$$

where A and B are the scaling parameters, q_x, q_y and q_z are the components of the vector q, and ξ_{xy}, ξ_z are the correlation lengths in lateral and vertical directions, respectively. Since the microgel dimensions are sufficiently larger than the correlation length, the cross-terms between both contributions can be neglected[167].

The following assumptions have been made to construct the sample model:

- According to the previous investigation of the p-ME_3O_5 structure[70,163], for a form factor,

‡Similar content will be presented in T. Kyrey, M. Ganeva, J. Witte, R. von Klitzing, S. Wellert, O. Holderer, Evanescent wave simulations: challenges and opportunities for the interpretation of grazing incidence scattering experiments (2019)

a core-shell particle has been chosen. Both, core and shell are considered as truncated spheres with mean radii of 53 and 135 nm and heights of 53 and 97 nm, respectively.

- The size distribution of the microgels is assumed to be Gaussian with FWHM equal to 20% of the microgel radius. Radius and height of the microgels are assumed to be fully correlated. The same assumption has been made for both, core and shell. The size of the core is scaled according to the shell size.

- For the core material p-ME_3O_5 was taken, while the shell material is assumed to be a mixture of p-ME_3O_5 and D_2O. The SLD for the shell material of $3.9 \cdot 10^{-6}$ Å^{-2} and for the core material of $2.0 \cdot 10^{-6}$ Å^{-2} are fixed from the fitting result of NR data.

- The Si/D_2O interface roughness is fixed at 1.2 nm. Hurst parameter of 0.8 was used in roughness function to characterises the smoothness of the surface (the closer to 1 the smoother it is). Lateral correlation length was set to 570 nm. These parameters were obtained from fitting of the NR and AFM data.

- The detector resolution has been estimated from the shape of the specular peak. It is assumed to be 2D Gaussian with a FWHM equal to 1.5×pixel size in the lateral direction and 0.7×pixel size in the vertical direction.

The simulation has been performed in decoupling approximation, where no correlation between microgel size and layout is assumed. The model also neglected the possible interference between the microgels due to their large size (no influence in the probed q-range). Any beam divergence has been neglected in the present simulation.

Simulation of the GISANS pattern. In Figure 6.3 the first iteration of the simulation together with the experimental GISANS pattern for p-ME_3O_5 are shown. The simulation and the experiment match to some extent. However, the simulation does not fully reproduce the diffuse scattering detected in the experiments. The form factor in the q_z slice (Fig. 6.3C) is well represented by the simulated GISANS pattern, showing that the overall structure of the modelled microgels is in agreement with the real one.

The deviations in the q_y cuts between the experiment and the simulation (Figure 6.3D) and diffuse scattering around the specular peak (Figure 6.3B) at first was attributed to the inhomogeneities inside the microgels or other features of the sample, which were not considered in the present model[129].

As the first attempt to characterise the internal structure of the adsorbed PEG-microgel and to reconstruct a lateral intensity dependence at the position of the Yoneda peak was in general acceptable, it turned out, however, to be a challenging task to reproduce the full 2D scattering pattern. Especially challenging was the simulation of the diffuse scattering contribution at the non-zero out-of-plan angle ($\psi \neq 0$ in Figure 2.16).

Commonly in the analysis of the 2D GISANS pattern only the reflected half space (GIS) is

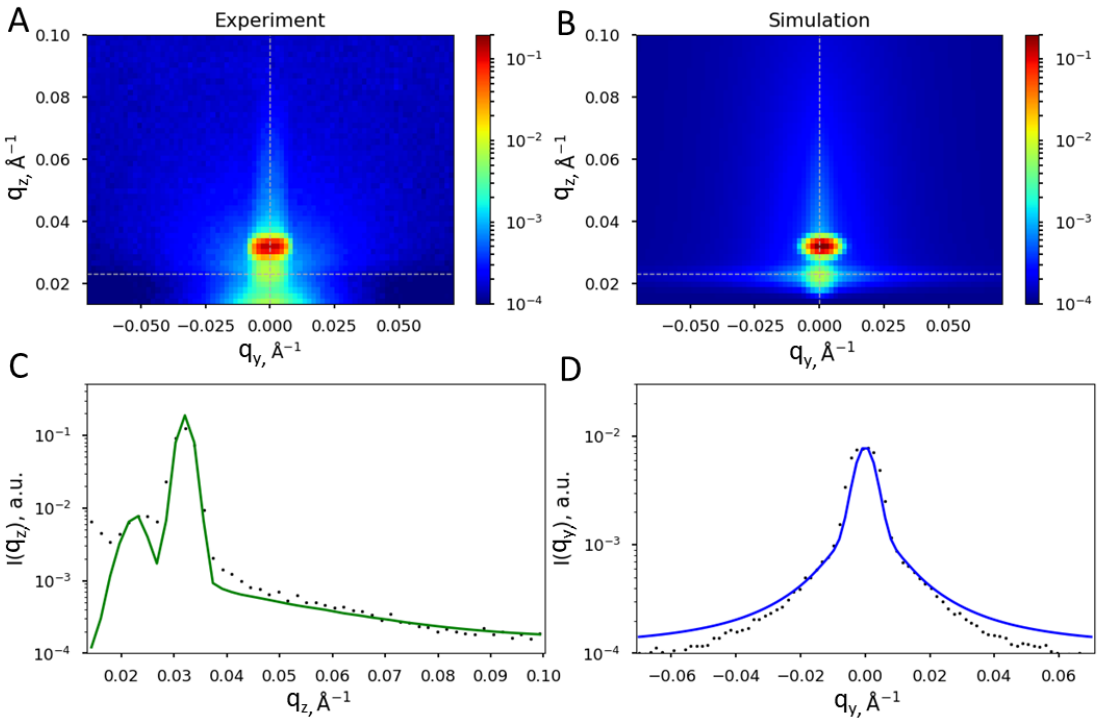

Figure 6.3: A) measured GISANS pattern. B) Simulated GISANS pattern. C) q_z slice at $q_y = 0$. D) q_y slice at the position of Yoneda peak. Solid green and blue lines represent simulation and dots represent experimental data. Slice positions are shown by thin dashed lines in 2D image.

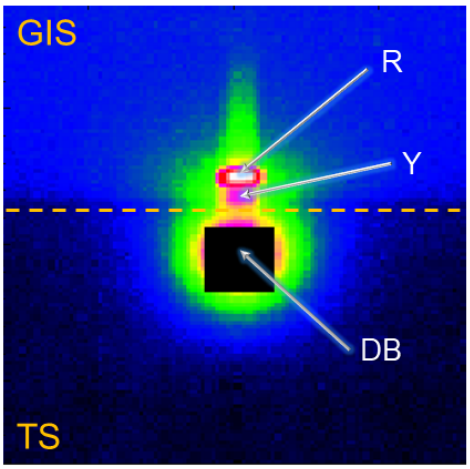

Figure 6.4: Experimental 2D-detector pattern. Orange dashed line divides the scattering pattern in two regions: GIS, where grazing incidence scattering is detected and TS part where signal from transmitted scattering and direct beam are detected. White arrows indicate reflected beam (R), Yoneda peak (Y) and direct beam (DB). DB is blocked by a beamstop to avoid detector damage.

considered and the scattering signal in transmission direction (TS) usually is not taken into account (Figure 6.4). The same approach was initially also utilized for the PEG-microgel simulation (as presented in Figure 6.3). However, transmitted signal can complement the data obtained from the GIS part[90] and depending on the experimental setup, namely an incident angle, sample-to-detector distance, detector size etc., the transmitted signal may influence the scattering in the GIS part.

In contrast to the X-ray experiment in GI geometry, where the beam is highly collimated and the beam divergence is low, in the GISANS experiment the neutron beam has a certain width and the wavelength distribution of approx. 10% (e.g. for KWS-1[142] or KWS-2[144]). It enhances the scattering signal but simultaneously leads to some peculiarities, which should not be overlooked during the data treatment.

At incidence angles α_i, which are slightly above the critical angle of the total reflection (α_c), the transmission scattering (TS) occurs. The scattering signal in the TS part corresponds to the transmission experiment with non-perpendicular to the sample surface incoming beam, that influences the shape of the scattering signal and also scattering intensity distribution. It leads to the differences in the footprint of the scattered beam for its upper- and lower-part. In Figure 6.5 area 1 and 2 correspond to the sample amount which crosses each "half" of the neutron beam. While the area 1 is bigger than the area 2, i.e. contains larger scattering volume, the intensity of the 2D scattering pattern in AB part is higher than in BC part (Figure 6.5). For the sake of clarity of the illustration, the incidence angle in Figure 6.5 is significantly larger than would be in a real experiment.

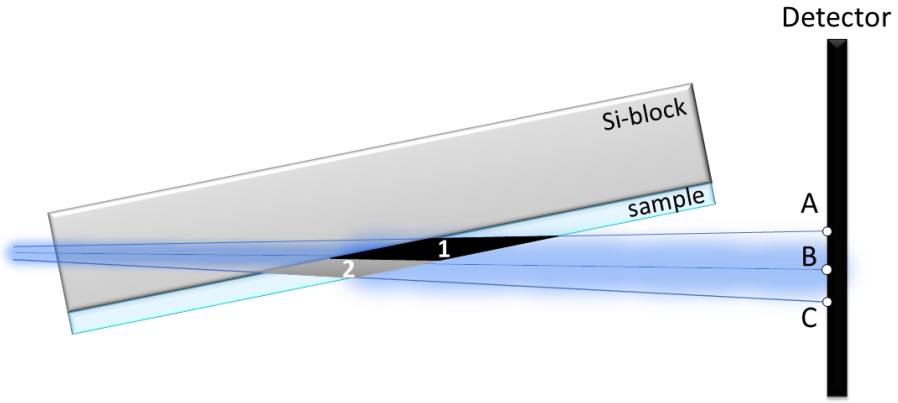

Figure 6.5: Schematic illustration of the transmission scattering in GISANS experiment: difference in the footprints of the upper- and down-part of the neutron beam due to the beam divergence.

To reconstruct the transmission scattering (TS) with BornAgain, the PEG-microgel model applied for the GIS simulation was taken. The incoming angle was set to 90°. To

account for the difference in the intensity distribution mentioned above, matrix of 2D scattering signal was multiplied with the vector, which provide more intense scattering in the upper part of the TS pattern (intensity relation of 2.5:1 was taken).

It should be noted that the neutron path through the sample is small. It allows to neglect the multiple scattering effects[128].

Figure 6.6 represents the experimental and the simulated 2D GISANS signal including the transmitted scattering in the direct beam direction. The simulated 2D pattern as well as line cuts at $q_y = 0$ (along q_z) and at α_c (parallel to the sample surface) are in good agreement with the experimental data. Speculatively, the difference in the diffuse scattering at the edge of the GIS part (Figure 6.6A,B) can be attributed to the instrumental imperfections and particle size distribution, which were not included in the simulations.

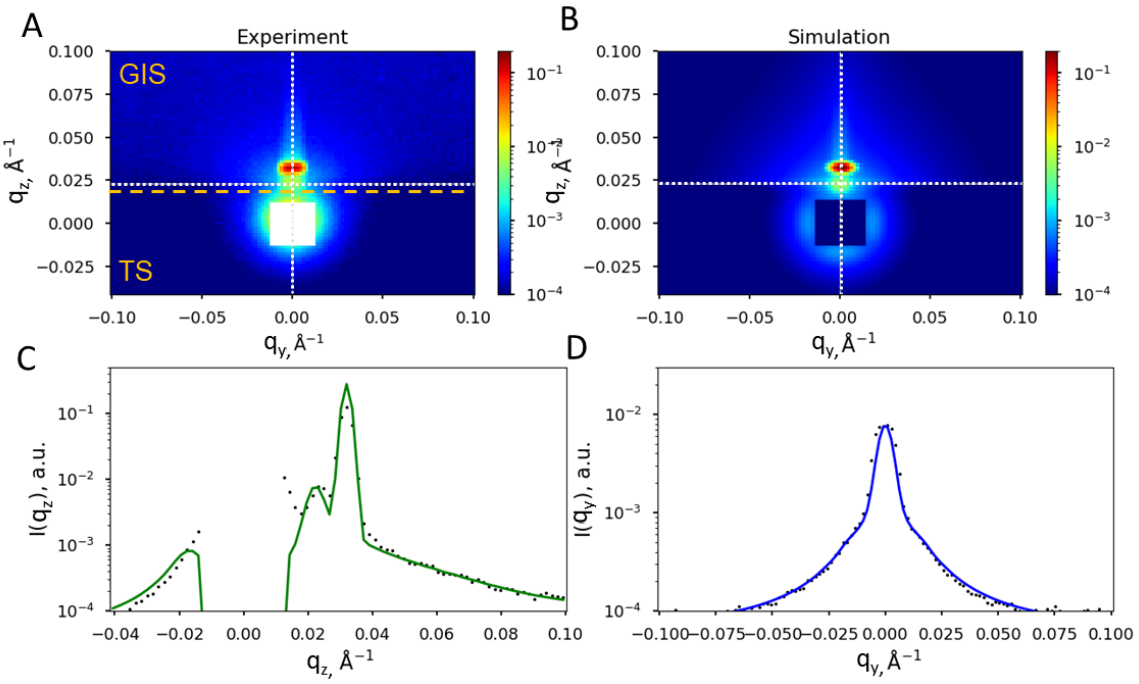

Figure 6.6: A) Experimental 2D scattering pattern. B) Simulated 2D scattering pattern. White dotted lines in (A, B) corresponds to the cuts depicted in (C, D). C) q_z slice at $q_y = 0$. D) q_y slice at the position of Yoneda peak. Dots and solid lines correspond to the experimental and the simulated data, respectively. Orange dashed line divides the scattering pattern in two regions: GIS and TS.

PNIPAM-brush model

According to the reported results of the structural investigation of the PNIPAM-brushes[165], they possess a non-constant SLD-profile, i.e. lower water content in the vicinity to the

solid surface and gradually increasing amount of the water in the outer brush layers.

The reflectivity experiments are commonly used to obtain information about the density distribution of the polymer brushes, in the direction normal to the surface[168–172]. The measured reflectivity depends on the variation of the scattering length density (SLD). To reconstruct the SLD profile of the polymer brushes, they are approximated as a combination of the layers with certain SLDs, thickness and roughness. And then, using minimising procedure a difference between the theoretical and the measured reflectivity curves is reached by changing the parameters which describe each layer[116]. In this case brushes are commonly represented as a one layer or two-layers structure with some averaged SLD and roughness. The initial characterisation of the SLD profile of the PNIPAM-brush was also performed in this manner. The PNIPAM-brush was described as one layer with SLD of $3.63 \cdot 10^{-6}$Å^{-2}, placed between the quasi-infinite sub-layers of the Si and D_2O. The initiator layer used for the grafting of the PNIPAN-brush on the silicon surface as well as SiO_2 layer were also accounted to the model. The fitting parameters obtained with the Motofit[116] are listed in Table 6.1.

Table 6.1: Fitting parameters of PNIPAM-brush according to initial one-layer model from Ref.[165].

System layer	Thickness nm	SLD $\times 10^{-6}$, Å^{-2}	Roughness nm
Si-block	∞	2.07	<1
SiO_2	1.3	3.47	<1
Initiator	1.3	0.56	<1
PNIPAM-brush	81	3.63	22
D_2O	∞	6.34	-

While the water penetrates the polymer brush and the height of the brush is not unique over the whole sample, no distinct interface between polymer and D_2O exists. Therefore, the high value of the roughness of the polymer/water interface (used in such simulations) is required to describe a gradual transition from the polymer to the water layer. The higher the SLD gradient between polymer and water is, the higher the roughness parameter should be applied (Figure 6.7). However, the roughness parameter here does not really mean the roughness of the polymer structure (in contrast to the Si-block surface roughness, which defines the polishing quality of the block surface) and yields a number of problems, especially for GIS simulations (see further).

To minimize the influence of the roughness on the numerical simulation, the transition from the polymer to the water layer was described with a slice model within BornAgain

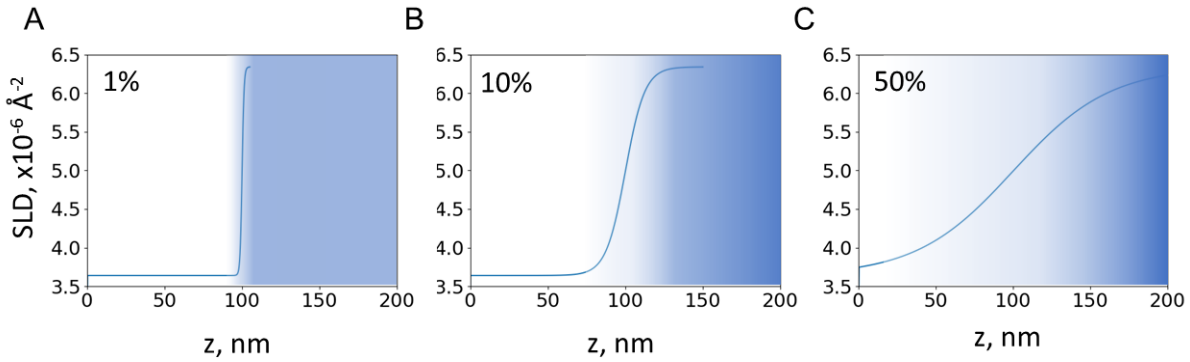

Figure 6.7: Variation of the polymer/water transition as a function of the ration between the roughness value and thickness of the polymer layer: A) 1%, B) 10%, C) 50%. White/blue gradient schematically illustrates polymer/water transition according to presented curves.

simulations. The brush was divided into 100 slices (1 slice is approx. 1 nm) with a progressive change of the polymer SLD from slice to slice. The SLD in the slice model alters according to the polymer volume fraction profile described by self-consistent field (SCF) theory[173] and is presented in equation 6.2.

$$\begin{cases} \phi(z) = \phi_0 * (1.0 - (z/h)^2) \\ \rho_i(z) = \phi(z) * \rho_{PNIPAM} + (1.0 - \phi(z)) * \rho_{D_2O} \end{cases} \tag{6.2}$$

where z is the distance from the surface, $\phi(z)$ is a polymer fraction at z, ϕ_0 is the polymer volume fraction at $z = 0$, h is the thickness of the brush, $\rho_{PNIPAM} = 0.8 \cdot 10^{-6}$ Å^{-2} and $\rho_{D_2O} = 6.34 \cdot 10^{-6}$ Å^{-2} are the scattering length density of PNIPAM and D_2O, respectively.

In Figure 6.8 fitting curves as well as SLD profiles according to the one-layer model and the slice model are presented. Since the scattering methods rely on the reciprocal space and the phase information is missing, an infinite number of the mathematical solutions is possible (well-known *phase problem*)[174]. Therefore, at least the fit parameters should be limited according to the additional knowledge about the studied system. The result of the fit leads to a slightly different SLD profile, although both fits successfully describe the reflectivity data (see Figure 6.8).

Since reflectivity values vary over several orders of magnitude, for a reliable characterization of the fit quality one needs a measure which equally weights errors along the whole curve. The following fit quality measure (score) complies this requirement:

$$s(q) = \left| \frac{y_s(q) - y_m(q)}{\varepsilon(q)} \right| \tag{6.3}$$

where $s(q)$ is the score calculated for each q value, $y_s(q)$ is the simulated reflectivity value,

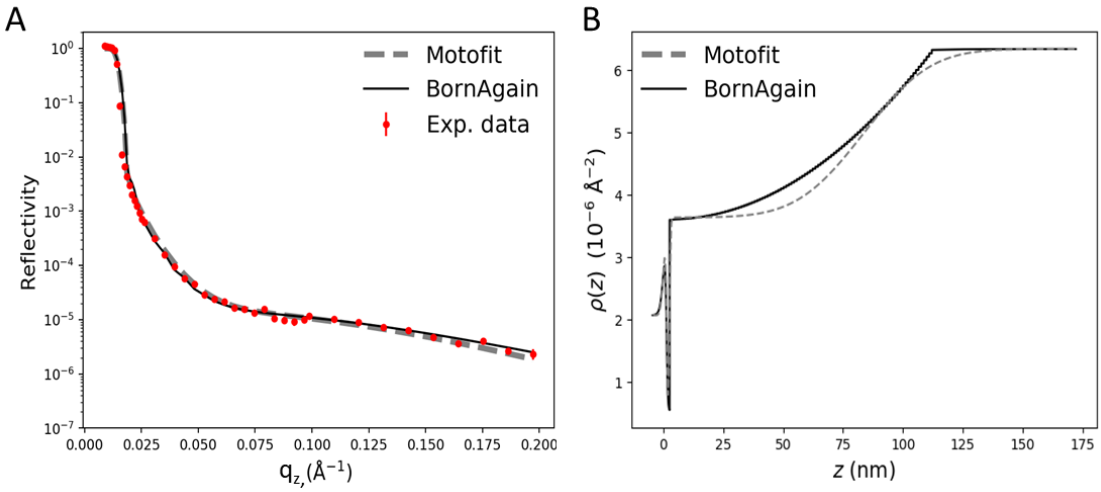

Figure 6.8: A) Fitting of the neutron reflectometry data fit with slice (BornAgain) and one-layer (Motofit) models. B) Corresponding SLD profiles. Solid black describes the result from the slice model, dashed grey line represents result from the one-layer model, red dots are experimental data from Ref.[165].

$y_m(q)$ is the measured reflectivity value, and $\varepsilon(q)$ is the experimental error. Confidence interval for the difference between mean Bornagain score and mean Motofit score is $(-1.1, 1.5)$. As one can see, it contains zero. Hence both, BornAgain and Motofit models fit the experimental data equally. However, from the Figure 6.8B the difference in SLD profiles between the two approaches is clearly visible. In the Motofit the polymer SLD is constant over a certain thickness and then rapidly approaches the SLD of D_2O and high roughness is needed to smear this transition. The slice model in BornAgain provide the stepwise description ot the polymer/water transition and is based on the theoretical prediction (SCF theory) and, thus should more correct describe the polymer brush.

6.3.2 Background correction

Additional to the scattering from the PEG-microgel and PNIPAM-brush, the scattering from solid surface, solvent and auxiliary layers (SiO_2, initiator) occurs, which contributes to the background scattering. To characterise the studied system this contribution should be separated or accounted during data analysis. Unfortunately in a GIS experiment reference measurement can not be directly subtracted from the total signal as in transmission experiment (e.g. SANS). Therefore, to estimate the contribution from the substrate and the different parts of the investigated systems to the general scattering signal, the simulation of GISANS with and without polymer system was performed. While only the relative intensities were of interest, arbitrary instrument parameters were selected and kept

fixed in all simulations. The intensities were compared at q of 0.08 Å^{-1} and 0.06 Å^{-1} for PEG-microgel and PNIPAM-brush, respectively (such q-value was chosen for the GINSES experiment due to the appropriate signal-to-noise ratio).

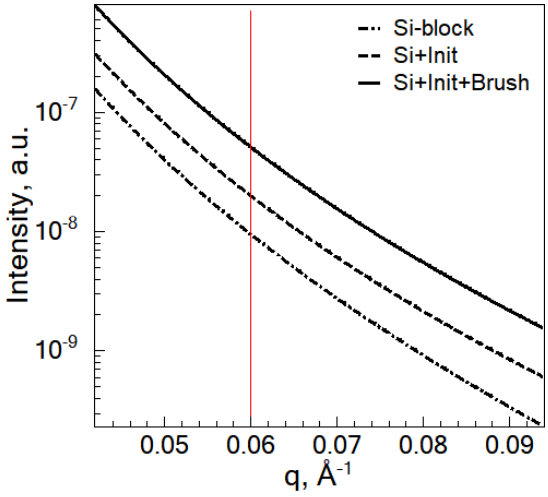

Figure 6.9: Scattering contribution of the Si-block and the initiator layer to the general scattering intensity of the PNIPAM-brush. All simulations are performed against D_2O.

To correctly simulate a roughness of the Si-block the following parameters were applied: Si block was modelled as a sub-layer with SLD of $2.07 \cdot 10^{-6}$ Å^{-2} and a roughness of 1 nm. According to *Teichert*[175], a Hurts parameter of 0.7 and a correlation parameter of 1 μm were applied.

According to Figure 6.9 the intensity contribution of the Si-block to the full scattering signal of the PNIPAM-brush at $q = 0.06$ Å^{-1} is 19%, while the contribution from the Si-block with an initiator layer is 40%. It is interesting to note, that the experimentally measured scattering intensity of the Si-block against D_2O is higher than the scattering from the adsorbed brush. Such difference could be explained with the difference in the roughness contribution. In GI geometry roughness is one of the parameters leading to an imperfection of the scattering surface and, thus, causing the GI scattering. Speculatively the coating of the Si-block with the initiator layer decreases the scattering contrast between Si and an environment, and therefore background contribution from Si surface becomes weaker.

In case of the PEG-microgel the simulated contribution from Si-block is less than 1% at $q = 0.08$ Å^{-1}.

6.3.3 Evanescent wave mapping

In BornAgain the evanescent wave is simulated as:

$$I_{EW}(z) = |\Psi(z)|^2 = \left|R \cdot e^{ik_z z} + T \cdot e^{-ik_z z}\right|^2 \tag{6.4}$$

where I_{EW} is the intensity of the evanescent wave, R is the reflectivity, T is the transmission coefficient, k_z is the z-component of the wave vector and z is the direction normal to surface.

BornAgain enables the 2D mapping of the evanescent wave intensity as a function of the incidence angle and the penetration depth.

To obtain information about the EW intensity distribution, the EW-map for each system was simulated according to the Eq. 6.4 and based on the models described in Section 6.2.1. Since EW-maps will be used for the further GINSES data analysis, the wavelength distribution of the J-NSE instrument[135] of 20% was applied.

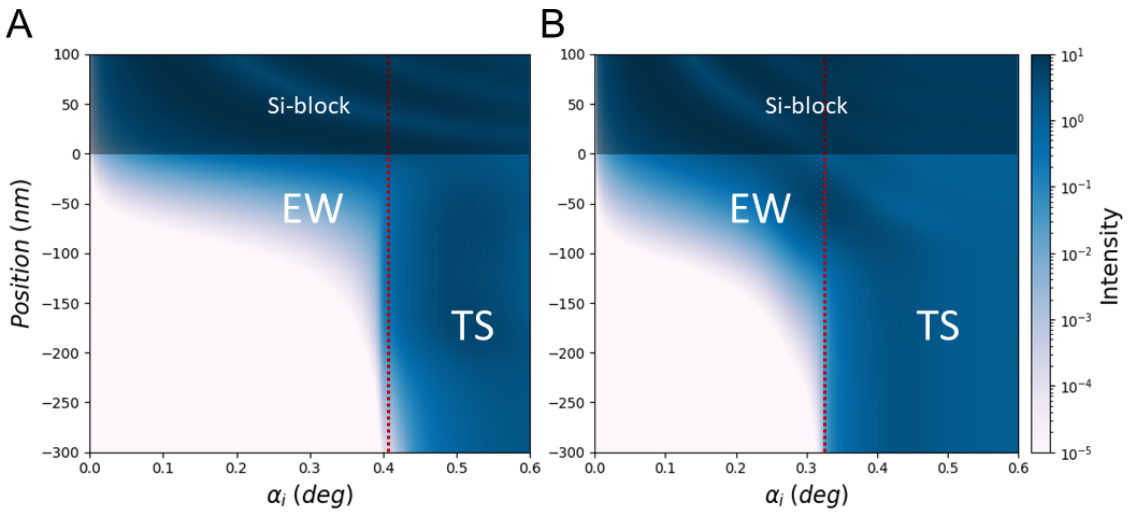

Figure 6.10: Intensity of the evanescent wave as a function of the penetration depth and incident angle for PEG-microgel (A) and PNIPAM-brush (B). Red dashed line roughly separates EW- and transmitted intensities.

In Figure 6.10 the EW-maps of the PEG-microgel and PNIPAM-brush are presented. The intensity in TS (at $\alpha_i > \alpha_c$) corresponds to the transmitted signal. In the EW-part the intensity of the evanescent wave decaying with the penetration depth is illustrated.

Here should be noted, that the above mentioned high values of the roughness parameter of the brush layer (22 nm in the one-layer model) lead to the unstable solution and unphysical results in GI geometry. An example of such negative influence is presented in Figure 6.11. In this case the roughness parameter is perceived as an additional "correlation"

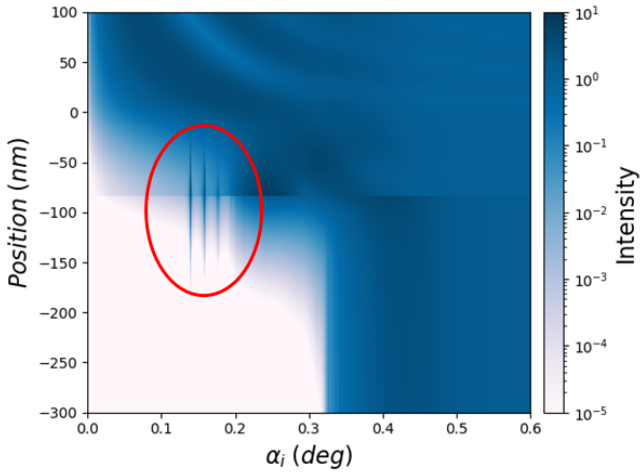

Figure 6.11: EW-map of the PNIPAM-brush according to one-layer model. Red circle indicate parasitic oscillations of the EW intensity caused by the high roughness parameter.

parameters and this leads to the apparent contribution of intensity oscillations to the EW intensity.

6.3.4 Scattering contribution from system components

Analysis of the cuts through the EW-map performed at constant incident angle allows to estimate the scattering contribution from the different parts of the PEG-microgel and PNIPAM-brush.

In Figure 6.12 the evanescent wave intensity as a function of the penetration depth at the incident angle below and above the critical angle of total reflection are presented. The incident angles of 0.35° and 0.2° (below α_c) and the incident angle of 1.0° (above α_c) were initially chosen to experimentally probe the near surface dynamics and dynamics in the whole volume of the PEG-microgel and PNIPAM-brush with GINSES.

Coloured areas represents the EW intensity distribution in different parts of the sample. From that quantitative analysis of the EW intensity at the different penetration depths at $\alpha_i < \alpha_c$, it was obtained: 70% of the evanescent wave intensity falls on the first 20 nm of the PNIPAM-brush, whereas in case of the PEG-microgel 82% of the EW intensity falls on the same thickness. Hence, the dynamics in this near surface region strongly contributes to the measured *S(q,t)*. This should be considered in the comparison of the data from the different samples.

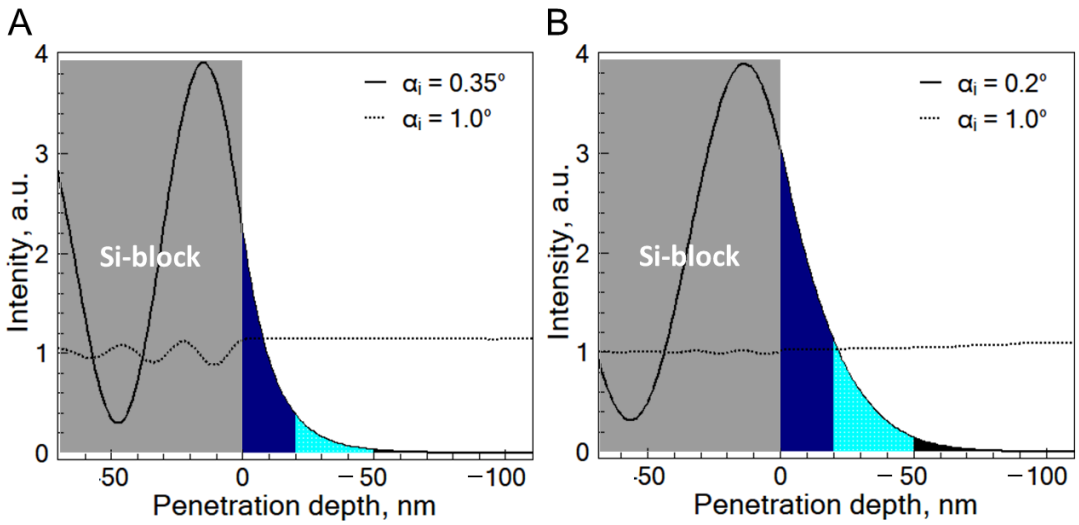

Figure 6.12: EW intensity of the PEG-microgel (A) and PNIPAM-brush (B) as a function of the penetration depth at selected incident angels: solid line at $\alpha_i = 0.35$ and $\alpha_i = 0.2°$, respectively, dotted line at $\alpha_i = 1.0°$.

6.4 Application of the simulation to the GINSES data

Earlier reported GINSES dynamics studies of the PEG-microgel[91] indicate a reduction of the relaxation rate as compared to the value obtained in the classical transmission NSE experiment from 0.0100 ns^{-1} to 0.0036 ns^{-1}. Such difference can be explained with the performed simulation as following. Accordingly to Figure 6.12, at $\alpha_i < \alpha_c$ mostly the near surface layers of the PEG-microgel contributes to the scattering signal. Moreover, the compression of the microgels after the adsorption process leads to the formation of the denser packed polymer sub-layer close to the Si-surface (the same tendency was also found for the PNIPAM microgels in Chapter 5). It causes the limitation of the polymer chain dynamics and thus leads to the slowing of the relaxation rate.

At $\alpha_i > \alpha_c$ on the other hand, the relaxation rate value measured in GI geometry is equal to the one obtained in the transmission NSE experiment, namely 0.01 ns^{-1} at $q = 0.8$ $Å^{-1}$.

At first sight it is in conflict with the logic, since the first confinement layers should noticeably contribute to the scattering and reduce the polymer dynamics, i.e. relaxation rate. However, the above simulation allows one to estimate the real contribution of the different layers of the probed system to the scattering signal at $\alpha_i > \alpha_c$. The adsorption process similar to the temperature collapse of the polymer chains leads to the decrease of the internal scattering contrast. The internal inhomogeneities become indistinguishable that leads to the SANS scattering intensity decrease at the probed q. From the SANS

data of the PEG-microgel the scattering intensities ratio at $q = 0.08$ Å^{-1} in the swollen and collapsed state is approx. 2:1[163] that also decreases the contribution from the first layer. Taking into account the thickness ratio of the first dense layer and the rest of the microgel of approx. 1:4 and EW intensity distribution according to the performed simulation (Figure 6.12), the scattering contribution from the first layers (20 nm) becomes smaller than from the rest. It means, that at $\alpha_i > \alpha_c$ the outer bulk-like region to a large extent contributes to the general scattering signal and the latter explains the equal values of the relaxation rate of the microgel in bulk and in adsorbed state, when the whole sample thickness is probed.

Figure 6.13 shows data from GINSES experiments on PEG-microgels in bulk and at the interface as reported in Ref.[91] at $q = 0.08$ Å^{-1}. The relaxation rates of the bulk sample and the one with $\alpha_i > \alpha_c$ have the same relaxation rates, as already mentioned.

Instead of fitting the relaxation rate for $\alpha_i = 0.35°$ with about 20 nm penetration depth separately, the fit function has been split into a bulk-like and a rigid component (as an extreme case) with the formula:

$$\frac{S(q,t)}{S(q,0)} = A + (A_1 - A)exp\left(-(\Gamma t)^{\beta}\right) \tag{6.5}$$

with an elastic component A and the amplitude A_1. Data have been normalized to 1 for accounting for different levels of incoherent and background contributions. The rate $\Gamma = 0.01$ Å^2/ns was taken from the bulk measurement, $\beta = 0.67$ as in Ref.[91]. The ratio $A/A_1 = 0.17$ indicates that at least 1/6 of the material in the first 20 nm of the particle has a reduced mobility compared to the bulk (assuming here mobility zero, otherwise it would be a larger fraction).

This example illustrates that the BornAgain simulations can help obtaining more precise knowledge of the interface properties even if the statistics does not allow to fit, e.g. stretch exponents as in a standard bulk experiment. Instead of including all changes into a changed relaxation rate, an immobile fraction could be extracted.

The coating of the Si block with PNIPAM-brush differs from the one with the PEG-microgels, and thus the background contribution from the additional initiator layer and the Si-block becomes more significant at $\alpha_i = 0.2°$ (20 – 40% as was shown in Section 6.3.2). Further work with PNIPAM-brushes with improved statistics is ongoing work[165].

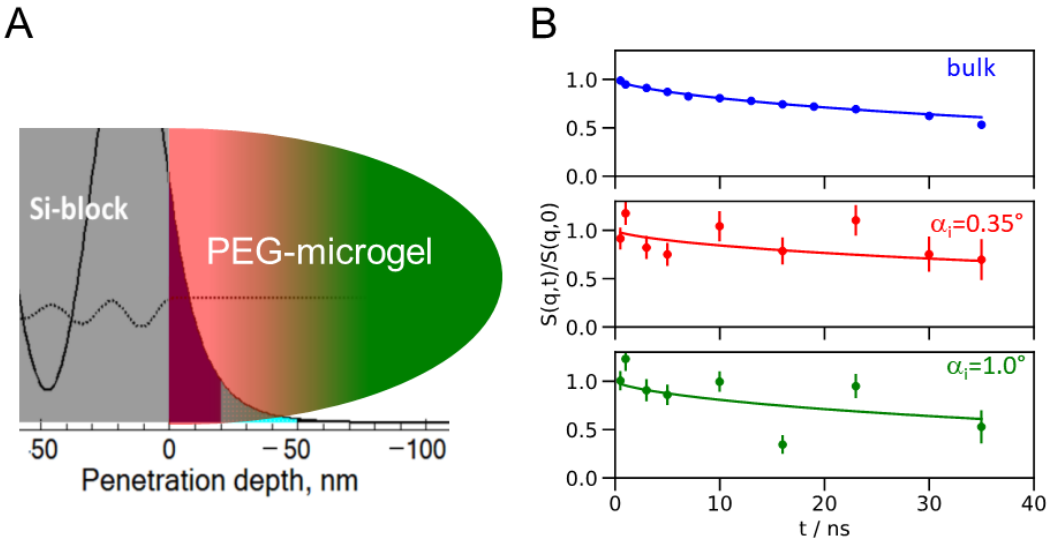

Figure 6.13: A) Schematic illustration of the EW intensity distribution within PEG-microgel according to the simulation. Red-green transition represents depths probed at different incident angles in GI geometry (colours correspond to the data in (B). B) Intermediate scattering functions of the PEG-microgels measured in bulk (blue) and adsorbed state at $\alpha_i = 0.35°$ (red) and $\alpha_i = 1.0°$ (green).

6.5 Conclusion

In the present chapter, for the examples of the PEG-microgel and PNIPAM-brush it was demonstrated how computing simulation in the frame of DWBA can help with GI scattering data analysis. Based on the previous studies of the mentioned systems, corresponding models were developed.

It has been shown, that commonly avoided scattering signal in the transmission geometry can significantly influence the grazing incidence scattering signal. Impact of the transmission scattering on the GI scattering should be accounted for depending on the experimental setup. To avoid such contribution the experimental parameters such as sample-to-detector distance and detector area, an incident angle should permit a splitting of the transmission and GI scattering contributions on detector. Using the presented simulation, the best experimental setup can be predicted or the contribution of the transmitted scattering to the total scattering signal considered.

Moreover, it was reported how the high roughness parameter of the polymer/water interface can lead to the problems in numerical simulations and unphysical results in GI geometry. To substitute the mathematically overstated roughness parameter, the slice model was presented.

The presented results illustrate, that a combination of numerical simulations pattern

can contribute to a better understanding of the near surface behaviour of the complex polymer systems.

Chapter 7

Test of simple neutron resonator at the substrate surface for grazing incidence scattering experiments*

Abstract

A simple resonator structure with three layers at the silicon substrate has been tested with respect to the impinging wave enhancement in terms of amplified scattering signals. The results are compared with the first resonator with three double layers in terms of background signal and intensity gain. The new 3-layer resonator promises much better performance than the earlier 7-layer version.

7.1 Introduction

To achieve a satisfied signal-to-noise ratio and to collect meaningful statistics in GISANS experiment approximately 12 hours are necessary (e.g. for PNIPAM microgels). To be able to detect small energy changes and thus to analyse the dynamics of the adsorbed polymer network by means of GINSES, the time-range expands even more (from hours to days). In this context, an improvement of the impinging intensities is demanded.

One possible way to solve the mentioned problem is the application of a resonater wave-guide. Neutron wave-guides reflect the neutron waves many times and, thus, can develop resonances at distinct incident angles through the constructive interference. These resonances give rise to higher primary intensities and enhanced evanescent wave, from which higher scattering signals can be obtained. This has been shown to be feasible for the sample of interest being embedded in the multilayer structure[176,177]. However, a sample of interest can be also placed outside the layered structures[93,138], how it was done in the current chapter. The separation of the layered structure from the sample allows to use advantages of resonator (enhanced signal) and makes the usage of the resonator more

*Similar content is presented in T. Kyrey, J. Witte, M. Gvaramia, S. Wellert, A. Koutsioubas, S. Mattauch, O. Holderer, H. Frielinghaus, Simpler neutron resonator enhances the wave-field for grazing incidence scattering experiments with lower parasitic scattering, Physica B: Condensed Matter (2018) 551, 405–406, 10.1016/j.physb.2018.07.022.

universal, and allows for reusing the costly parts.

Earlier *Frielinghaus et al.*[138] have presented a 7-layer resonator: three double titanium-platinum layers with a single finishing titanium layer caused three resonances and led to the intensity gain. Simultaneously, unwanted scattering signals from the resonator structure itself were observed. In order to achieve a higher scattering signal in GINSES as well as in GISANS experiments and to avoid the interference within the resonator structures being detected for 7-layer resonator, a simpler 3-layer resonator is tested in this chapter. Since the previous test of the 7-layer resonator[138] was done using the microemulsion as scattering sample, in the presented studies the same system was used to be able to compare an impact of the simpler resonator to the scattering signal.

7.2 Results and Discussion

The scheme of the 3-layer resonator is presented in Figure 7.1. Since the resonator is working properly as long as the critical q_c of total reflection is bigger than the q-values of the resonance(s), i.e. $q_c = 4\pi(\Delta\rho/\pi)^{1/2} > q_{res} \approx 2\pi/d$ (with d being the repeat distance of the layered structure), the proposed resonator was constructed of Ti/Pt/Ti layers with thickness of 130/320/130 Å on top of a large silicon block with dimensions of 50×80×15 mm^3. The sputtering of Ti/Pt/Ti was done by Swiss Neutronics (Klingnau, Switzerland). These two materials are ideally suited for the sputtering, and serve for rather low and high scattering length densities (i.e. -1.91 and 6.36 · 10^{-6} Å^{-2}) even at natural isotope abundances. Moreover, non-magnetic materials used for the resonator fabrication ideally serve for the neutron spin-echo experiments and do not disturb neutron polarization.

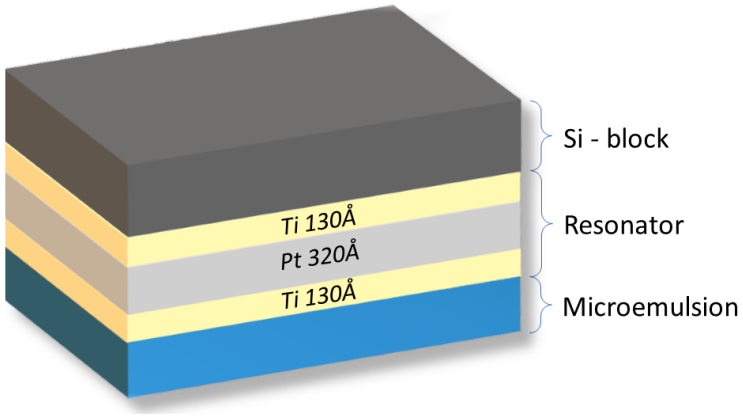

Figure 7.1: Scheme of the sample 3-layer resonator embedded between silicon block and sample of interest (here microemulsion).

The microemulsion selected for the resonator test consisted of 41.5 vol% D_2O, 31.1 vol% d-decane, 10.3 vol% h-decane, and 17 vol% non-ionic $C_{10}E_4$ surfactant. In previous studies of this microemulsion[178], four perfect lamellar domains of water or oil adjacent to the solid-liquid interface before the order decays over the perforated lamellae to the bicontinuous structure were found. The scattering length densities for Si/Ti/Pt/D_2O/d-decane/surfactant are 2.07/-1.95/6.36/6.36/6.49/0.12 $\cdot$ 10^{-6}Å^{-2}.

The GISANS experiment in normal and grazing incidence mode was performed on the MARIA reflectometer. The microemulsion was probed against a neat Si-block and the one with the simple resonator. The instrument was operated at a wavelength of 10 Å with $\Delta\lambda/\lambda = 10\%$ and beam divergence of 0.02°.

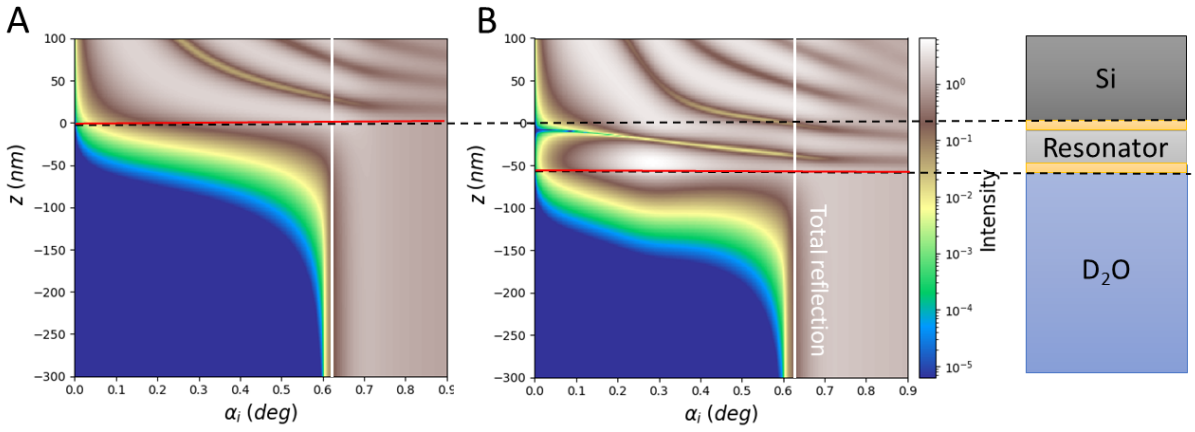

Figure 7.2: Simulated evanescent wave intensity as a function of an incident angle, α_i, and a penetration depth, for A) silicon block against D_2O and B) Si-block with the simple 3-layer resonator against D_2O. An intensity penetrated sample of interest is below a black dashed line. White line roughly separates EW- and transmission intensities.

To proof the functionality of the 3-layer resonator DWBA simulations with the BornAgain software package and reflectivity test measurements of the resonator against D_2O were performed. Figure 7.2 illustrates the simulated EW-intensity distribution as a function of an incident angle (α_i) and a penetration depth (z) of the neat silicon block (A) and the 3-layer resonator (B) against D_2O. The presence of the resonator causes an intensity increase of the evanescent wave at α_i of 0.2 – 0.35° with maximal intensity at $\alpha_i \approx 0.27$. In Figure 7.3 the reflectometry data of the resonator against D_2O and the simulated NR data are presented. The experimental data clearly showed the dip within a plateau of the total reflection. Here, neutrons are scattered from the enhanced wave-field by the D_2O (incoherent scattering) that are then finally missing in the specular reflex. This proofs for the resonator working properly. This effect was not simulated by the DWBA that covers only the wave distortion in the normal direction[138]. The position of the dip minimum

corresponds to the incident angle of $\sim 0.27°$. According to the simulation (Figure 7.2) and the experimental data (Figure 7.3), an incident angle of 0.28° was taken for the GISANS experiment to be below the critical angle of the total reflection and to cover the resonance.

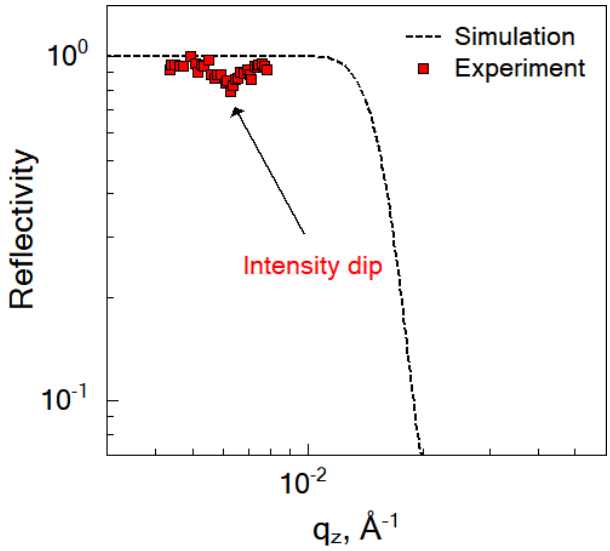

Figure 7.3: Intensity dip within the plateau of total reflection caused by the simple resonator. Red squares – NR experimental data, dashed line – BA simulation.

In Figure 7.4A reflectivity scans of the microemulsion with and without the resonator are compared. Fresnel fringes appear with the maxima at ca. 0.016, 0.032, 0.052 $Å^{-1}$ etc. only in presence of the resonator layers and correspond to the theoretically calculated peaks corresponding to the microemulsion layers at surface and not to the resonator layer as it was obtained in case of 7-layer resonator. There the oscillation of the neutron reflectivity intensity was caused by the double layer periodicity of the 7-layer resonator structure. It should be noted that the first order Bragg peak (theoretically at ca. 0.013 $Å^{-1}$) in case of 3-layer resonator is partially hidden below the critical angle of the total reflection (not seen in Figure 7.4A) and leads to the intensity enhancement.

Figure 7.4B shows the GISANS scattering when the detector cut along the q_z (at $q_y = 0$) is performed. There is a clear shoulder at $q_z = 0.02$ to 0.04 $Å^{-1}$. While it is weak for the neat silicon block, it is much more pronounced in the presence of the resonator. Comparison of the intensities at $q_z = 0.03$ $Å^{-1}$, where the highest intensity of the microemulsion is expected, gives an intensity gain of 3.9 (9.3 vs. 36 a.u.). The high-q background subtraction increases this value to 7.2. Taking into account the overall diffuse signal, that is rather high (in units of Figure 7.4B of approx. 30), the gain factor might be smaller than initially estimated, but is higher than for 7-layer resonator.

The other parameter, that significantly influences the diffuse scattering intensity, is the

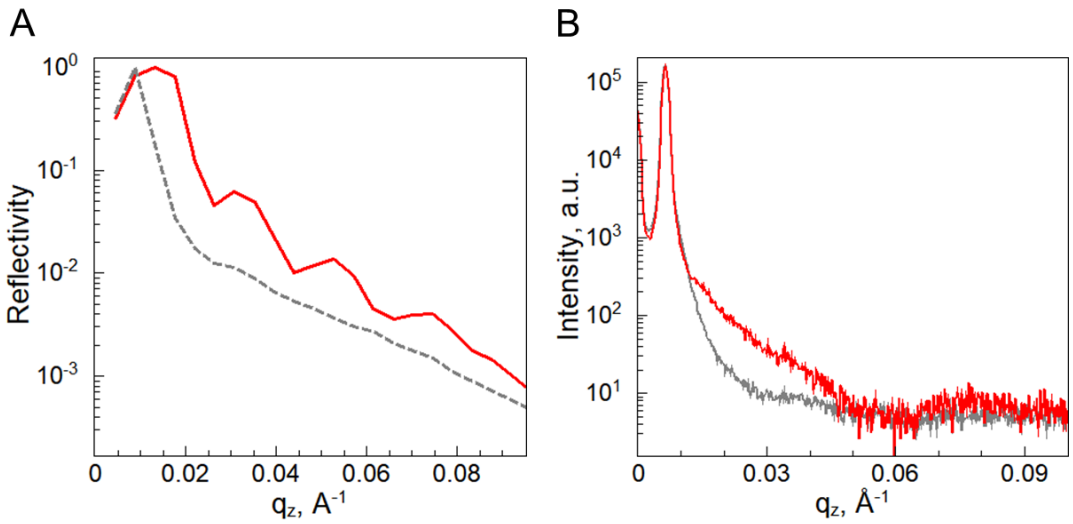

Figure 7.4: A) Reflectivity curves of the microemulsion with (red line) and without (grey dashed line) resonator measured. B) Line cuts of two-dimensional GISANS data along q_z for the microemulsion with (red line) and without (grey line) resonator. The curves are normalized with respect to the acquisition time. Incident angle $\alpha_i = 0.28°$, wavelength λ = 10Å. Measurement were performed at temperature of 27°C.

roughness of the solid surfaces (Si-block, resonator). It is one of the crucial points of the "ideal" resonator performance. However, while best possible polishing leads to a very low roughness, the variations with rather long correlation length could still have a significant influence on the resonator performance[179]. These points should be taken into account in further improvement of the resonator quality and in improving of the gain factor of this technique.

7.3 Conclusion

In this chapter the initial test of the simple 3-layer resonator was performed. The presence of the resonater layers clear indicates enhanced intensity of scattered signal compare to neat Si-block. It was shown, that simple resonator has advantages compared to the resonator with a 7-layer structure, namely lower background and higher intensity gain of 4 to 7 (vs. ca. 3 obtained in Ref.[138]) were observed.

It was shown, that devices based on resonator principle could be used for the enhancing of scattering signal in gracing incidence geometry, however further development and better understanding of parameters influencing the intensity gain factor is still needed.

Chapter 8

Conclusion and future perspectives

8.1 Conclusion

This thesis comprises two main parts dedicated to microgels investigations. In the first one an impact of the internal crosslinker distribution on the structure and dynamics of the PNIPAM microgels was studied with respect to the spacial confinement, namely the fundamental investigations of the internal structure and dynamics of the PNIPAM microgels in bulk and the internal structure in the adsorbed state were performed (Chapter 4-5). The second part was devoted to the peculiarities appearing in the investigation of the thin polymer films at grazing incidence conditions, the improvement of the experimental conditions and the subsequent data analysis (Chapter 6-7).

In the first part structure and dynamics of the microgels prepared via batch and feeding synthesis with 0.5, 2 and 5 mol% of crosslinker (BIS) were investigated. The shape and internal structure of the PNIPAM microgels were probed by means of DLS, SANS and SAXS at temperatures below and above the volume phase transition. Influence of the crosslinker distribution on the dynamics of the PNIPAM microgels was investigated with NSE at 20°C.

Different preparation procedures and variation of the crosslinker concentration had a remarkable influence on the internal structure. While both batch- and feeding-microgels possess the inhomogeneous domain-like internal structure, which is preserved even above the VPTT, the number and the size of the domains within a single microgel strongly depend on preparation process, crosslinker and initiator concentration.

The feeding approach leads to a more homogeneous crosslinker distribution with larger correlation length ξ, but significantly smaller frozen inhomogeneities Ξ below the VPTT and smaller spherical domain size above the VPTT compared to the batch-microgels.

At 20°C (temperature below the VPTT), an increase of the crosslinker concentration leads to a slight increase of the mesh size for all six microgels: from 3.5 nm to 3.6 nm for the batch-microgels and from 7.6 nm to 8.7 nm in case of the feeding-microgels. At 50°C the BIS concentration variation leads to the domain size in the range of 20–33 nm. The largest number of the domains is formed at the highest crosslinker content.

Interesting to note, that the variation of the initiator AAPH concentration in the microgel with 0.5 mol% BIS does not influence the mesh size of its network below the VPTT, however above the VPTT at lower AAPH amount the size of the internal domains is larger: 40.6 nm at 0.16 mol% AAPH vs. 28.6 nm at 1.7 mol% AAPH.

The structural peculiarities of the PNIPAM microgels also affect their internal dynamics

and leave an imprint on the resulting segmental chain behaviour. In case of the feeding-microgels, segmental dynamics contributes at all investigated BIS concentrations, however, due to the presence of the internal structural inhomogeneities a clear Zimm dynamics, even for the feeding-microgel with the lower crosslinker concentration was not observed. In case of the batch-microgels, the increase of the BIS concentration leads to the denser network and the cooperative polymer dynamics becomes dominant at 5 mol% BIS.

Since microgels can be potentially used for the controlled producing of the polymer matrix used for active agents loading, where the matrix parameters should be commensurate with the size of potential active agents, the variation of the internal characteristic sizes of the polymer network by the variation of the crosslinker concentration and preparation process can be of great use for such approach (Chapter 4).

The presence of the rigid interface leads to changes of the microgels physico-chemical properties, that can be in a large extent elucidated in changes of the network structure. Concerning latter problem, the internal structure of the adsorbed PNIPAM batch-microgels was studied with the surface sensitive neutron scattering methods such as NR and GISANS at temperatures below and above the VPTT. The morphology of the microgels after adsorption was probed with AFM.

The crosslinker concentration has remarkable influence on the microgels deformability. At 5 mol% BIS well-defined individual microgels on Si substrate of ∼500 nm were formed, while at lower crosslinker concentration the adsorption process leads to the formation of a fuzzy polymer layer. Speculatively, microgels with 0.5 mol% BIS have a fluffier shell, which undergoes stronger deformation through the adsorption. Thus, the dangling ends from the shell part of the microgel cover the whole surface and prevent the microgel recognizability with AFM, however GISANS allows to characterise internal structure of the microgels independent of crosslinker concentration. It was shown, that the surface confinement significantly affects the thermoresponsiveness of the polymer network in the vicinity to the solid interface. Temperature change does not affect the internal microgel structure in lateral direction regardless of the BIS concentration. The thermal fluctuations and static density correlation lengths of ∼5 – 6 nm and ∼23 – 24 nm, respectively, were found to be constant below and above the VPTT within the precision of the experiment for the adsorbed batch-microgels with 0.5 and 5 mol% BIS.

The main alterations of the internal structure of the PNIPAM batch-microgels caused by the adsorption process are presented in Figure 8.1. In particular, the adsorption process significantly alters macroscopic and microscopic parameters of the microgels. The shape of the microgels undergoes deformation, namely suppression in vertical direction ($h < R_{DLS}$) and extension in the lateral direction ($L > R_{SANS}$ and $L > R_{DLS}$). The latter has an

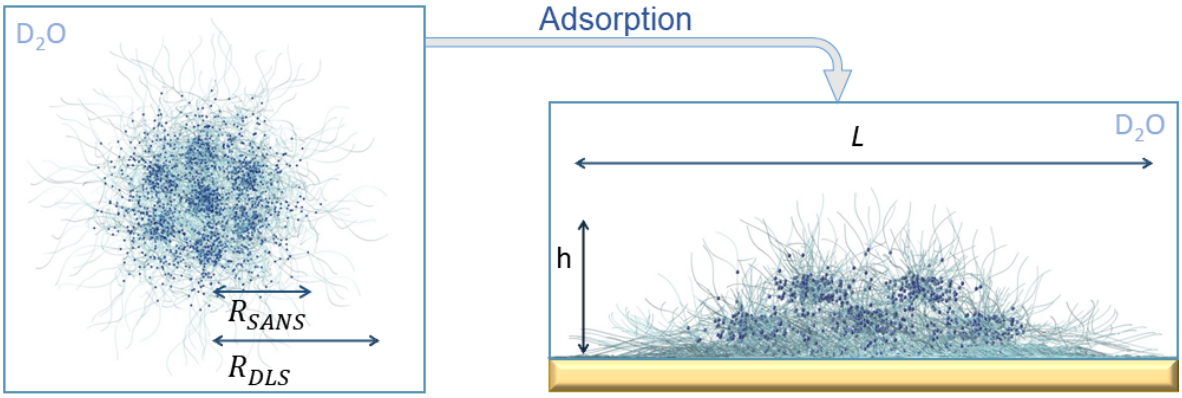

Figure 8.1: Microscopic and macroscopic structural changes of the batch-microgels caused by adsorption process.

impact on the increase of the internal correlation length of the polymer network ($\xi_s > \xi$). The deformation leads to the decrease of the microgel volume.

In contrast to the investigation of the bulk polymer systems with transmission scattering techniques (DLS, SANS, SAXS), probing of the internal structure and dynamics of the adsorbed polymer systems in the vicinity to the solid interface requires application of the grazing incidence (GI) geometry which is still a challenging task. Therefore, in this thesis simulations in the frame of the Distorted Wave Born Approximation as auxiliary tool for the preparation to GINSES/GISANS experiment and further data analysis was applied.

Due to a shallow incident angle in the GI experiments, both the GI scattering signal and scattering around the direct beam (as in transmission mode) are detected on the 2D detector simultaneously. To obtain the structural information of the probed system, usually only the GI signal is taken into account and used for the data analysis. However, in this thesis the considerable influence of the transmitted intensity on the GI scattering was evidenced. Its neglect would lead to the incorrect data analysis and non-physical results.

Adsorbed polymer systems such as microgels or brushes in swollen state (in water) possess a gradual transition from the polymer-rich region to the water interface. To characterise such gradient a roughness parameter of the polymer/water interface is applied in a literature. Large roughness values (up to 50%), are commonly used as compares to the general polymer layer thickness. However, the high roughness value does not correspond to the roughness in classical conception and leads to unphysical results in further GI data treatment (parasitic features), that was shown in this thesis. The slice model was proposed to replace the large roughness of the polymer/water interface and to perform further simulation in BornAgain software for GINSES data treatment.

The simulation of the evanescent wave scattering map allowed obtaining of the scattering

signal as a function of the penetration depth and incident angle. It permitted to account the scattering contribution from the different part (layers) of the probed polymer systems and can be used for the estimation of the best experimental conditions. Moreover, since the background scattering in GISANS/GINSES experiment can not be measured separately and then be directly extracted as e.g. in SANS experiment, simulation of the scattering from the solid surface or additional layers (initiator or fixing layer) has been used to account the background contribution to the general scattering signal.

The major obstacle in the structure and dynamics investigations of the adsorbed thin polymer films in grazing incidence geometry is the low intensity of the scattering signal. To overcome this problem the application of the solid substrate coated with the resonated layers was proposed in this thesis. Test of the simple 3-layer resonator resulted in the enhance of the scattering signal by a factor of 4 to 7 (the intensity gain depends on the background correction). Further studies are necessary, however the current approach has indicated, that employment of the resonated structures in grazing incidence experiments increases the intensity of the scattering signal. Moreover, the simple 3-layer structure tested in this thesis has lower scattering contribution from itself (considered as background) as compared to a more complex 7-layer resonator proposed in earlier studies.

8.2 Future perspectives

Polymer microgels excite high scientific interest due to their unique responsiveness to the external stimuli. Simultaneously, it opens a wide opportunity to possible applications, which demand thorough understanding of the microgel properties in different environments. The combination of the imaging and scattering techniques allow obtaining a clear knowledge about structural and dynamical behaviour of the microgel network in conditions close to practical applications.

The influence of the preparation process, crosslinker and initiator concentration on the behaviour of the internal microgel network was presented in this thesis. However, in the context of the possible application of the loading by pharmaceutical agents further investigations of the batch- and feeding-microgels with a more controlled variation of the synthesis components (e.g. series of the initiator amount variation, control of the final crosslinker concentration) are of high relevance.

In this work the structure of the batch-microgels after adsorption onto Si-surface was studied. The adsorption of the feeding-microgels onto the solid surface may lead to the formation of a more homogeneous structures. The higher order of the internal inhomogeneities over a large surface can promote the "smart" polymer coating development. Therefore, application of the surface sensitive techniques such as NR and GISANS and characterisation of the internal structure of the adsorbed feeding-microgels are necessary. In a future perspective, a comparison of the internal polymer network parameters with and without the embedded pharmaceutical agents is obvious.

The dynamics of adsorbed polymer systems has been theoretically discussed but the experimental studies are scarce. Therefore, a great attention should be directed toward further dynamics investigation of the PNIPAM microgels in the vicinity to solid surface with GINSES. Based on the rare previous measurements, it is clear that the preparation of the GINSES experiment requires better understanding of the investigated systems and accounting for the experimental conditions (e.g. wavelength distribution, geometry of the experiment). As was shown in this thesis the BornAgain simulations of the scattering can help solving these problems. In order to advance the process of the GINSES data analysis and preparation to the GINSES experiment (choosing of the more appropriate experimental setup, i.e. q-range, incident angle α_i), further development and systematisation of the BornAgain simulations are required.

Appendix

Appendix to Chapter 4

Application of the Porod law to the SANS data

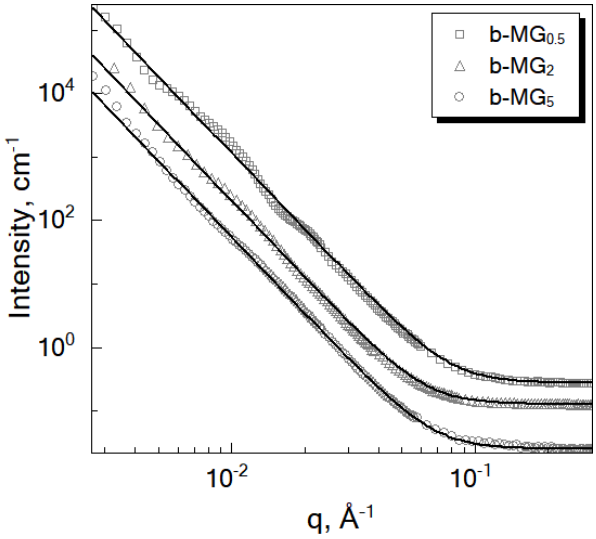

Figure A1: SANS spectrum of b-MG$_X$ fitted with the Porod law ($I(q) = Aq^{-\alpha}$, $\alpha = 4$). Measurements performed at 50°C.

X-ray small-angle scattering

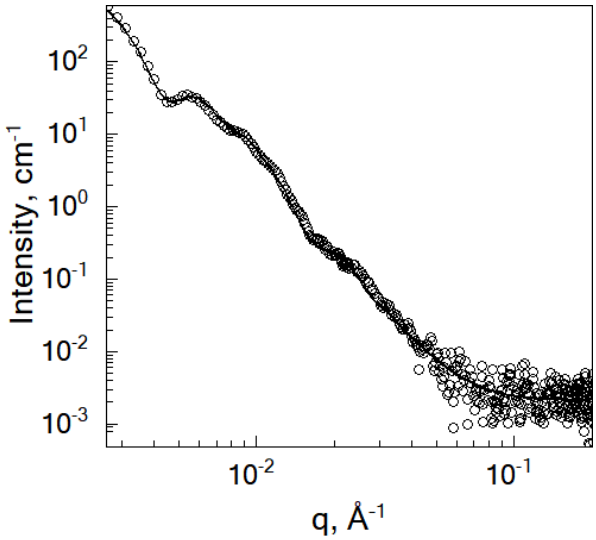

Figure A2: SAXS spectrum of the batch-microgel with 0.5 mol% BIS and 1.7 mol% initiator (b-MG$_{0.5}$) measured at 60°C. Line corresponds to the fit with SiS-model.

Table A1: Comparison of the fit parameters for system b-$MG_{0.5}$ obtained from SANS and SAXS using the same SiS model. Errors are <1%.

Method	R, nm	r, nm
SANS	100	28.6
SAXS	101.4	29.1

Internal domains concentration

To estimate the concentration of the domains (B) inside an individual microgel (A), presented in Figure A3, further calculations were performed. The SiS model used for the fitting of the SANS and SAXS data of the batch-microgels at 50°C is:

$$I(q,R,r) = I_A P(q,R) + I_B P(q,r) + I_{inc} \tag{A1}$$

where $P(q,x) = [3(sinxq - xqcosqx)/(xq)^3]^2$ is the form factor of spheres with a radius x (R or r), $q = 4\pi/\lambda sin\Theta$ is the momentum transfer with neutron wavelength λ and scattering angle 2Θ, I_{inc} takes into account incoherent scattering.

Scaling parameters I_A and I_B are:

$$I_i(i = A,B) = \phi_i V_i (\Delta\rho_i)^2 \tag{A2}$$

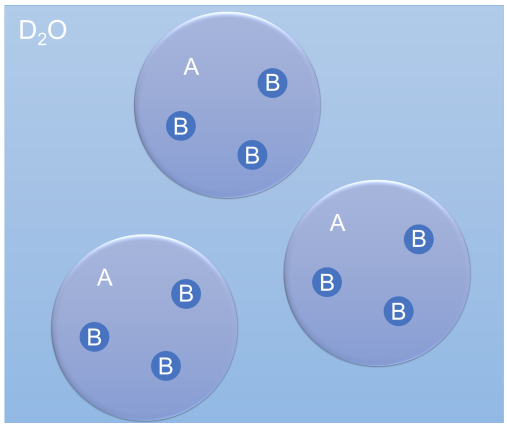

Figure A3: Spheres-in-sphere model visualization.

For individual microgels:

$$I_A = \phi_A V_A (\Delta\rho_A)^2 \tag{A3}$$

Where $\phi_A = n_A V_A / V$ is a microgel volume concentration, n_A – a number of microgels in a volume V, V_A – a volume of the individual microgel A. $\phi_{BinA} = \phi_B/\phi_A = (n_B V_B)/(\phi_A V)$

is a volume concentration of the domains B inside the microgel A.

$$\Delta\rho_A = \phi_{BinA}\rho_B + (1-\phi_{BinA})\rho_{D_2O} \tag{A4}$$

$$I_B = \phi_{BinA}\frac{(n_B V_B)}{(n_A V_A)}V_B(\rho_B - \rho_{D_2O})^2 = \phi_{BinA}^2 V_B(\rho_B - \rho_{D_2O})^2 \tag{A5}$$

Eq. A4 in Eq. A3:

$$I_A = \phi_A V_A(\Delta\rho_A)^2 = \phi_A(\phi_{BinA})^2 V_A(\rho_B - \rho_{D_2O})^2 \tag{A6}$$

From Eq. A6 and Eq. A5:

$$\frac{I_B}{I_A} = \frac{V_B}{V_A\phi_A} \tag{A7}$$

From Eq. A6:

$$\phi_{BinA}^2(\rho_B - \rho_{D_2O})^2 = \frac{I_A}{\phi_A V_A} \tag{A8}$$

While $(\Delta\rho_B)^2 = (\rho_B - \rho_{D_2O})$ is not exactly known parameter, the relation of the domain number to the microgel number $N^* = n_B/n_A = \phi_{BinA}V_A/V_B$ was estimated at possible $\Delta\rho_B$.

Application of different models to ISF fitting process

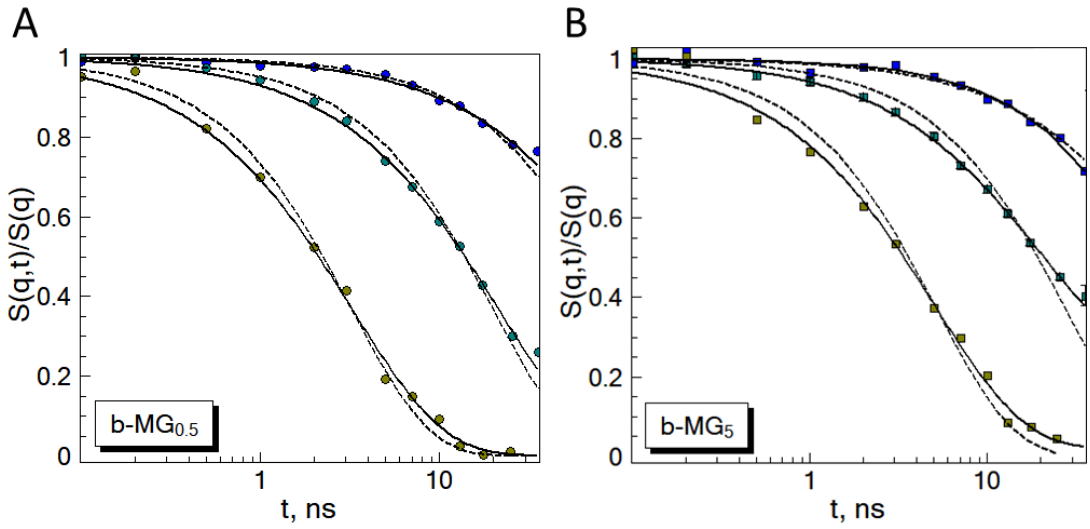

Figure A4: Comparison of the experimental ISF of the batch-microgel b-$MG_{0.5}$ (A) and b-MG_5 (B) with a single exponential function (dashed line) reported by *Hellweg*[3] and a function including Zimm motion (solid line) for selected q.

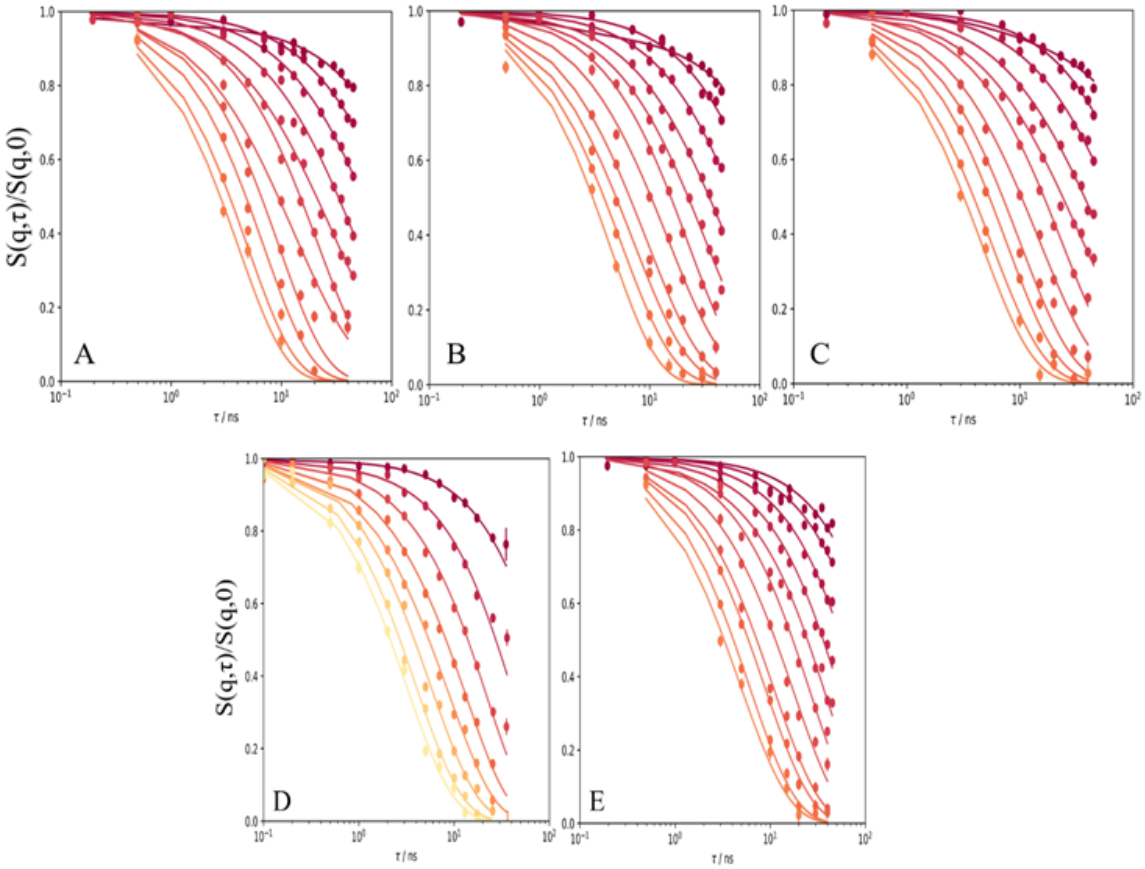

Figure A5: Application of the full Zimm model to the ISF of the f-MG$_x$ (A – 0.5 mol% BIS, B – 2 mol% BIS, C – 5 mol% BIS) and p-MG$_x$ (D – 0.5 mol% BIS, E – 2 mol% BIS) microgels. q changes from $q_{min} = 0.041$ Å^{-1} (top curve) to $q_{max} = 0.19$ Å^{-1} (bottom curve).

Appendix to Chapter 6

BornAgain scripts

Simulation of the PNIPAM-brush with slice model

```
import numpy as np
from matplotlib import pyplot as plt
import bornagain as ba
from bornagain import nm, deg, angstrom

filename102 = "XXX.dat"

sld_D2O = 6.34e-06
sld_pnipam = 2.64e-06 #with D2O content

h = 81.0*nm
phi0 = 0.78

```

```
14 # slice model
15 nslices = 100
16 def phi(z):
17     return phi0*(1.0 - (z/h)**2)
18
19 def get_sld(z):
20     pz = phi(z)
21     return pz*sld_pnipam + (1.0 - pz)*sld_D2O
22
23 # brush collection
24 def add_brush_layers(multilayer):
25     dz = h/nslices
26     zvals = np.linspace(0, h, nslices, endpoint=False) + 0.5*dz
27     for z in zvals:
28         sld = get_sld(z)
29         material = ba.MaterialBySLD("Brush_{:.1f}".format(z), sld, 0.0)
30         layer = ba.Layer(material, dz)
31         multilayer.addLayer(layer)
32
33 def get_sample():
34     # defining Materials
35     material_si = ba.MaterialBySLD("Substrate", 2.07e-06, 2.3e-11)
36     material_sio2 = ba.MaterialBySLD("SiO2", 3.47e-06, 1.05e-11)
37     material_init = ba.MaterialBySLD("Initiator", 5.6e-07, 6.5e-11)
38     material_d2o = ba.MaterialBySLD("D2O", 6.34e-06, 1.13e-13)
39
40     # defining Layers
41     layer_si = ba.Layer(material_si)
42     layer_sio2 = ba.Layer(material_sio2, 1.3)
43     layer_init = ba.Layer(material_init, 1.3)
44     layer_d2o = ba.Layer(material_d2o)
45
46     # defining roughness parameters
47     layerRoughness_1 = ba.LayerRoughness(0.99, 0.7, 1000.0*nm)
48     layerRoughness_2 = ba.LayerRoughness(0.39, 0.7, 1000.0*nm)
49     layerRoughness_3 = ba.LayerRoughness(10.88, 0.7, 1000.0*nm)
50
51     # defining multilayers
52     multilayer = ba.MultiLayer()
53     multilayer.addLayer(layer_si)
54     multilayer.addLayerWithTopRoughness(layer_sio2, layerRoughness_1)
55     multilayer.addLayerWithTopRoughness(layer_init, layerRoughness_2)
56     add_brush_layers(multilayer)
57     multilayer.addLayerWithTopRoughness(layer_d2o, layerRoughness_3)
58     return multilayer
59
60 # running simulation
61 def get_simulation():
62     simulation = ba.SpecularSimulation()
63     scan = ba.AngularSpecScan(10.0 * angstrom, 500, 0.0 * deg, 8.5 * deg)
64     simulation.setScan(scan)
65     simulation.setBeamIntensity(1.0)
66     # add wavelength distribution
67     distr_1 = ba.DistributionGaussian(10.0 * angstrom, 0.430 * angstrom)
68     simulation.addParameterDistribution("*/Beam/Wavelength", distr_1,
69              50, 2.0, ba.RealLimits.positive())
70     return simulation
71
72 def run_simulation():
73     sample = get_sample()
74     simulation = get_simulation()
75     simulation.setSample(sample)
76     simulation.runSimulation()
77     return simulation.result()
78
```

```
79
80 def plot_reflectivity():
81     result = run_simulation()
82     units=ba.AxesUnits.QSPACE
83     intensity = result.array()
84     x_axis = np.array(result.axis(units))/10.0  # convert to 1/A from 1/nm
85     ymax = np.amax(intensity)*2.0
86     ymin = 1.0e-07
87
88     xlabel = r'$\mathrm{Q}$ $(\mathrm{\AA^{-1}})$'
89     ylabel = "Reflectivity"
90
91     plt.plot(x_axis, intensity, color='k', linestyle='-', label=r'BornAgain')
92
93     motofit = np.loadtxt(filename104)
94     motofit = motofit[motofit[:,0].argsort()]
95     plt.errorbar(motofit[:, 1], motofit[:, 0], linestyle='--', color='gray',
96                                                label=r'Motofit')
97     expdata102 = np.loadtxt(filename102)
98     expdata102 = expdata102[expdata102[:,0].argsort()]
99     plt.errorbar(expdata102[:, 0], expdata102[:, 1], yerr=expdata102[:,2],
100                               marker='.', markersize=8, linestyle='None',
101                               color='r', label=r'Exp. data')
102    plt.ylim([ymin, ymax])
103    plt.yscale('log')
104    plt.xlabel(xlabel, fontsize=15)
105    plt.ylabel(ylabel, fontsize=15)
106    plt.legend(loc='upper right', fontsize=12)
107    plt.show()
108
109 def plot_ew_intensity():
110    simulation = ba.DepthProbeSimulation()
111    simulation.setBeamParameters(6.0*angstrom, 500, 0.0*deg, 0.6*deg)
112    simulation.setZSpan(500, -300.0*nm, 100.0*nm)
113    simulation.setBeamIntensity(1.0)
114
115        # add wavelength distribution (20% selector)
116    distr_wl = ba.DistributionTrapezoid(0.6*nm, 0.12*nm, 0.0*nm, 0.12*nm)
117    simulation.addParameterDistribution("*/Beam/Wavelength", distr_wl,
118                          50, 0.0, ba.RealLimits.positive())
119
120    sample = get_sample()
121    simulation.setSample(sample)
122    simulation.runSimulation()
123    result = simulation.result()
124    return result
125
126 if __name__ == '__main__':
127    import matplotlib
128    matplotlib.rcParams['image.cmap'] = 'PuBu'
129    plot_reflectivity()
130    ew_result = plot_ew_intensity()
131    ba.plot_simulation_result(ew_result, intensity_min=1.0e-05,
132              intensity_max=10.0)
```

Simulation of the PEG-microgel

```
import numpy as np
import bornagain as ba
from bornagain import deg, angstrom, nm

#SLDs
sld_Si = 2.074e-6
sld_Si_im = 2.3819e-11
sld_D2O = 6.356e-6
sld_D2O_im = 1.1295e-13

# particle dimensions
b = 1.1e+08
xi = 11.0
xiz = 2.3
height = 97.0*nm
radius = 135.0*nm
core_radius = 53.0*nm
core_height = 53.0*nm

def vol(r, h):
    v = 2.0/3.0 + (h-r)/r - ((h-r)/r)**3/3.0
    return v*np.pi*r*r*r

def get_sample():
    pfraction = 1.2e-05
    sld_core = 2.0e-06
    sld_shell = 3.9e-06

    # defining materials
    m_si = ba.MaterialBySLD("Si", sld_Si, sld_Si_im)
    m_D2O = ba.MaterialBySLD("D2O", sld_D2O, sld_D2O_im)
    m_core = ba.MaterialBySLD("Me3O5:D2O", sld_core, 0.0)
    m_shell = ba.MaterialBySLD("Me3O5:D2O", sld_shell, 0.0)

    # layer with particles
    Vcore = vol(core_radius, core_height)
    Vshell = vol(radius, height) - Vcore
    f_D2O = 0.7
    f_core = (1.0 - f_D2O)/(1 + Vshell/Vcore)
    f_shell = (1.0 - f_D2O)/(1 + Vcore/Vshell)
    sld_mix = f_D2O*sld_D2O + f_shell*sld_shell + f_core*sld_core
    m_mix = ba.MaterialBySLD("mix", sld_mix, 0.0)

    # fluctuation OZ component
    ff_microgel = ba.FormFactorOrnsteinZernike(b, xi, xiz)
    microgel = ba.Particle(m_core, ff_microgel)
    microgel_layout = ba.ParticleLayout()
    microgel_layout.addParticle(microgel, 1.0 - pfraction)

    # collection of particles
    ff = ba.FormFactorTruncatedSphere(radius=radius, height=height)
    ff_core = ba.FormFactorTruncatedSphere(radius=core_radius,
                 height=core_height)
    transform = ba.RotationY(180.0 * deg)
    shell_particle = ba.Particle(m_shell, ff)
    core_particle = ba.Particle(m_core, ff_core)
    core_position = ba.kvector_t(0.0, 0.0, 0.0)
    particle = ba.ParticleCoreShell(shell_particle, core_particle,
             core_position)
    particle.setPosition(ba.kvector_t(0.0, 0.0, 0.0))
    particle.setRotation(transform)

    microgel_layout.addParticle(particle, pfraction)
    microgel_layout.setTotalParticleSurfaceDensity(1.0)
```

```
65
66      # describe layer roughness for resonator
67      roughness_1 = ba.LayerRoughness(1.0*nm, 0.8, 1000.0*nm)
68      roughness_1 = ba.LayerRoughness(1.2*nm, 0.8, 570.0*nm)
69
70
71      D2O_layer = ba.Layer(m_D2O)
72      mix_layer = ba.Layer(m_mix, 2.0*height)
73      mix_layer.addLayout(microgel_layout)
74      si_layer = ba.Layer(m_si)
75
76      multi_layer = ba.MultiLayer()
77      multi_layer.addLayer(si_layer)
78      multi_layer.addLayerWithTopRoughness(mix_layer, roughness_1)
79      multi_layer.addLayerWithTopRoughness(d2o_layer, roughness_2)
80      return multi_layer
81
82  def plot_ew_intensity():
83      """
84      Run simulation and return evanescent wave intensity
85      """
86      simulation = ba.DepthProbeSimulation()
87      simulation.setBeamParameters(8.0*angstrom, 500, 0.0*deg, 0.6*deg)
88      simulation.setZSpan(500, -300.0*nm, 100.0*nm)
89
90          #add wavelength distribution (for 20\% selector)
91      distr_wl = ba.DistributionTrapezoid(0.8*nm, 0.16*nm, 0.0*nm, 0.16*nm)
92      simulation.addParameterDistribution("*/Beam/Wavelength", distr_wl,
93              50, 0.0, ba.RealLimits.positive())
94
95      sample = get_sample()
96      simulation.setSample(sample)
97      simulation.runSimulation()
98      result = simulation.result()
99      return result
100
101 if __name__ == '__main__':
102     import matplotlib
103     matplotlib.rcParams['image.cmap'] = 'PuBu'
104     result=plot_ew_intensity()
105     ba.plot_simulation_result(result, intensity_max=10)
```

Abbreviations and symbols

AAPH	2,2'-azobis (2-methylpropionamidine) dihydrochloride
AFM	atomic force microscopy
BIS	*N,N'*-methylenebisacrylamide
DLS	dynamic light scattering
DWBA	Distorted Wave Born Approximation
GI	grazing incidence
GINSES	grazing incidence neutron spin-echo spectroscopy
GISANS	grazing incidence small-angle neutron scattering
LCST	lower critical solution temperature
NIPAM	N-isopropylacrylamide
NSE	neutron spin-echo
PNIPAM	poly(N-isopropylacrylamine)
SANS	small-angle neutron scattering
SAXS	small-angle X-ray scattering
Si	silicon
StDD	sample-to-detector distance
VPTT	volume phase transition temperature
wt%	percentage by mass

α_a	absorption cross-section
α_c	critical angle of total reflection
α_i	incident angle
α_f	scattered angle
b	coherent scattering amplitude
b_i	scattering length
C	illuminated surface area
D	neutron scattering depth
D_f	fractal dimension
e	electron charge
f_i	real part of the atomic scattering factor
h_{dry}	microgel hight in dry state
h_{wet}	microgel hight in swollen state
γ	Larmor constant
h	microgel hight
H	strength of magnetic field
I_{inc}	incoherent scattering
I_{DB}	the scattering signal of the frozen inhomogeneities at $q = 0$
I_{OZ}	the scattering signal of the thermal fluctuations at $q = 0$
$I(\mathbf{q}, \omega)$	intermediate scattering function (ISF)
$I(\theta, t)$	scattering signal
$\mathbf{k}$	wavevector
k_B	Boltzmann constant
ξ, Ξ	correlation lengths of microgels in bulk
ξ_s, Ξ_s	correlation lengths of adsorbed microgels
l	length of magnetic field (coil)
λ	wavelength
m_e	mass of electron
η	viscosity
n	refractive index
N	atomic number density
P	beam polarization

$P(q)$	form factor
ϕ	volume concentration
ϕ	spin rotation angle
Θ	scattering angle
$\mathbf{q}$	scattering vector
r	internal domain radius
r_e	electron radius
R	reflectivity
R	microgel radius
$\rho(r)$	scattering length density
σ	roughness
σ	FWHM
$d\sigma/d\Omega$	differential cross section
$S(q)$	structure factor
$S(q,\omega)$	scattering function
$S(q,t)$	normalized intermediate scattering function
T	temperature
V	volume
$\overline{\mathbf{V}}$	interaction potential
ϕ	volume fraction
ψ	out-of-plane angle
$\Psi_{i,s}$	wavefunction

Bibliography

[1] Niebuur, B.-J.; Claude, K.-L.; Pinzek, S.; Cariker, C.; Raftopoulos, K. N.; Pipich, V.; Appavou, M.-S.; Schulte, A.; Papadakis, C. M. *ACS Macro Letters* **2017**, *6*, 1180–1185.

[2] Höfl, S.; Zitzler, L.; Hellweg, T.; Herminghaus, S.; Mugele, F. *Polymer* **2007**, *48*, 245–254.

[3] Hellweg, T.; Kratz, K.; Pouget, S.; Eimer, W. *Colloids and Surfaces A: Physicochemical and Engineering Aspects* **2002**, *202*, 223–232.

[4] Karg, M.; Prévost, S.; Brandt, A.; Wallacher, D.; von Klitzing, R.; Hellweg, T. *Progress in Colloid and Polymer Science* **2013**, *140*, 63–76.

[5] Koizumi, S.; Monkenbusch, M.; Richter, D.; Schwahn, D. *Journal of Chemical Physics* **2004**, *121*, 12721–12731.

[6] Fernandez-Barbero, A.; Fernandez-Nieves, A.; Grillo, I.; Lopez-Cabarcos, E. *Physical Review E* **2002**, *66*, 051803.

[7] Meier-Koll, A.; Pipich, V.; Busch, P.; Papadakis, C. M.; Müller-Buschbaum, P. *Langmuir* **2012**, *28*, 8791–8798.

[8] Wu, C.; Wang, X. *Physical Review Letters* **1998**, *80*, 4092–4094.

[9] Marcombe, R.; Cai, S.; Hong, W.; Zhao, X.; Suo, Z. *Soft Matter* **2010**, *6*, 784–793.

[10] Suzuki, A.; Tanaka, T. *Nature* **1990**, *346*, 345–347.

[11] Ahn, S.-K.; Kasi, R. M.; Kim, S.-c.; Zhou, Y. *Soft Matter* **2008**, *4*, 1151–1157.

[12] Hong, W.; Zhao, X.; Suo, Z. *Journal of the Mechanics and Physics of Solids* **2010**, *58*, 558–577.

[13] Tanaka, T. *Physica A: Statistical Mechanics and its Applications* **1986**, *140*, 261 – 268.

[14] Echeverria, C.; Fernandes, S. N.; Godinho, M. H.; Borges, J. P.; Soares, P. I. P. *Gels* **2018**, *4*.

[15] Hu, X.; Tong, Z.; Lyon, L. A. *Colloid and Polymer Science* **2011**, *289*, 333–339.

[16] Islam, M. R.; Serpe, M. J. *Chemical Communications* **2013**, *49*, 2646–2648.

[17] Liu, Y.; Zhang, Y.; Guan, Y. *Chemical Communications* **2009**, 1867–1869.

[18] Nolan, C. M.; Serpe, M. J.; Lyon, L. A. *Macromolecular Symposia* **2005**, *227*, 285–294.

[19] Hoffman, A. S. *Advanced Drug Delivery Reviews* **2012**, *64*, 18–23.

[20] Pelton, R. *Advances in Colloid and Interface Science* **2000**, *85*, 1–33.

[21] Gil, E. S.; Hudson, S. M. *Progress in Polymer Science* **2004**, *29*, 1173–1222.

[22] Mohanty, P. S.; Nöjd, S.; Gruijthuijsen, K. V.; Crassous, J. J.; Obiols-Rabasa, M.; Schweins, R.; Stradner, A.; Schurtenberger, P. *Scientific Reports* **2017**, *7*, 1487.

[23] Karg, M.; Hellweg, T. *Current Opinion in Colloid & Interface Science* **2009**, *14*, 438–450.

[24] Richtering, W.; Saunders, B. R. *Soft Matter* **2014**, *10*, 3695–3702.

[25] Richter, D.; Monkenbusch, M.; Arbe, A.; Colmenero, J. *Advances in Polymer Science* **2005**, *174*, 1–221.

[26] Schulte, M. F.; Scotti, A.; Gelissen, A. P. H.; Richtering, W.; Mourran, A. *Langmuir* **2018**, *34*, 4150–4158.

[27] Su, W.; Zhao, K.; Wei, J.; Ngai, T. *Soft Matter* **2014**, *10*, 8711–8723.

[28] Scherzinger, C.; Holderer, O.; Richter, D.; Richtering, W. *Physical Chemistry Chemical Physics* **2012**, *14*, 2762–2768.

[29] Heskins, M.; Guillet, J. E. *Journal of Macromolecular Science: Part A - Chemistry* **1968**, *2*, 1441–1455.

[30] Li, Y.; Tanaka, T. *Annual Review of Materials Science* **1992**, *22*, 243–277.

[31] Hirotsu, S. *Journal of the Physical Society of Japan* **1987**, *56*, 233–242.

[32] Niskanen, J.; Tenhu, H. *Polymer Chemistry* **2017**, *8*, 220–232.

[33] Atkins, P. W.; de Paula, J. *Atkins' physical chemistry*; W. H. Freeman, 2009.

[34] Wu, X.; Pelton, R. H.; Hamielec, A. E.; Woods, D. R.; Mcphee, W. *Colloid & Polymer Science* **1994**, *272*, 467–468.

[35] Shibayama, M. *Polymer Journal* **2010**, *43*, 18–34.

[36] Bastide, J.; Leibler, L. *Macromolecules* **1988**, *21*, 2647–2649.

[37] Panyukov, S.; Rabin, Y. *Physics Reports* **1996**, *269*, 1 – 131.

[38] Stieger, M.; Richtering, W.; Pedersen, J. S.; Lindner, P. *Journal of Chemical Physics* **2004**, *120*, 6197–6206.

[39] Saunders, B. R. *Langmuir* **2004**, *20*, 3925–3932.

[40] Witt, M. U.; Hinrichs, S.; Mo, N.; Backes, S.; Fischer, B.; von Klitzing, R. *Journal of Physical Chemistry B* **2019**, *123*, 2405–2413.

[41] Acciaro, R.; Gil, T.; Varga, I. *Langmuir* **2011**, *27*, 7917–7925.

[42] Brugnoni, M.; Scotti, A.; Rudov, A. A.; Gelissen, A. P. H.; Caumanns, T.; Radulescu, A.; Eckert, T.; Pich, A.; Potemkin, I. I.; Richtering, W. *Macromolecules* **2018**, *51*, 2662–2671.

[43] Maccarrone, S.; Scherzinger, C.; Holderer, O.; Lindner, P.; Sharp, M.; Richtering, W.; Richter, D. *Macromolecules* **2014**, *47*, 5982–5988.

[44] Kyriakos, K.; Philipp, M.; Silvi, L.; Lohstroh, W.; Petry, W.; Müller-Buschbaum, P.; Papadakis, C. M. *Journal of Physical Chemistry* **2016**, *120*, 4679–4688.

[45] Gasser, U.; Hyatt, J. S.; Lietor-Santos, J. J.; Herman, E. S.; Lyon, L. A.; Fernandez-Nieves, A. *Journal of Chemical Physics* **2014**, *141*, 034901.

[46] Dulle, M.; Jaber, S.; Rosenfeldt, S.; Radulescu, A.; Fo, S.; Mulvaney, P.; Karg, M. *Physical Chemistry Chemical Physics* **2014**, *17*, 1354–1367.

[47] Scotti, A.; Bochenek, S.; Brugnoni, M.; Fernandez-Rodriguez, M. A.; Schulte, M. F.; Houston, J. E.; Gelissen, A. P. H.; Potemkin, I. I.; Isa, L.; Richtering, W. *Nature Communications* **2019**, *10*, 1418.

[48] Ikkai, F.; Shibayama, M. *Polymer* **2007**, *48*, 2387–2394.

[49] Hellweg, T. *Nanoscale Materials* **2007**, 209–225.

[50] Keerl, M.; Pedersen, J. S.; Richtering, W. *Journal of the American Chemical Society* **2009**, *131*, 3093–3097.

[51] Wellert, S.; Radulescu, A.; Carl, A.; von Klitzing, R.; Gawlitza, K. *Macromolecules* **2015**, *48*, 4901–4909.

[52] Papagiannopoulos, A.; Zhao, J.; Zhang, G.; Pispas, S. *European Polymer Journal* **2014**, *56*, 59–68.

[53] Karanastasis, A. A.; Zhang, Y.; Kenath, G. S.; Lessard, M. D.; Bewersdorf, J.; Ullal, C. K. *Materials Horizons* **2018**, *5*, 1130–1136.

[54] Siemes, E.; Nevskyi, O.; Sysoiev, D.; Turnhoff, S. K.; Oppermann, A.; Huhn, T.; Richtering, W.; Wöll, D. *Angewandte Chemie International Edition* **2018**, *57*, 12280–12284.

[55] Seiffert, S. *Macromolecular Rapid Communications* **2012**, *33 (13)*, 1135–1142.

[56] Still, T.; Chen, K.; Alsayed, A. M.; Aptowicz, K. B.; Yodh, A. G. *Journal of Colloid and Interface Science* **2013**, *405*, 96–102.

[57] Wolff, H.; Kather, M.; Breisig, H.; Richtering, W.; Pich, A.; Wessling, M. *ACS Applied Materials and Interfaces* **2018**, *10*, 24799–24806.

[58] Berndt, I.; Richtering, W. *Macromolecules* **2003**, *36*, 8780–8785.

[59] Kratz, K.; Hellweg, T.; Eimer, W. *Polymer* **2001**, *42*, 6631–6639.

[60] Wei, M.; Gao, Y.; Li, X.; Serpe, M. J. *Polymer Chemistry* **2017**, *8*, 127–143.

[61] Gutowski, S. M.; Templeman, K. L.; South, A. B.; Gaulding, J. C.; Shoemaker, J. T.; LaPlaca, M. C.; Bellamkonda, R. V.; Lyon, L. A.; Garcia, A. J. *Journal of Biomedical Materials Research Part A* **2014**, *102A*, 1486–1499.

[62] Cooperstein, M. A.; Nguyen, P. A. H.; Canavan, H. E. *Biointerphases* **2017**, *12*, 02C401.

[63] Lynch, I.; Miller, I.; Gallagher, W. M.; Dawson, K. A. *Journal of Physical Chemistry* **2006**, *110*, 14581–14589.

[64] Schmidt, S.; Zeiser, M.; Hellweg, T.; Duschl, C.; Fery, A.; Möhwald, H. *Advanced Functional Materials* **2010**, *20*, 3235–3243.

[65] Tsai, H.-Y.; Vats, K.; Yates, M. Z.; Benoit, D. S. W. *Langmuir* **2013**, *29*, 12183–12193.

[66] Zhang, X.; Pint, C. L.; Lee, M. H.; Schubert, B. E.; Jamshidi, A.; Takei, K.; Ko, H.; Gillies, A.; Bardhan, R.; Urban, J.; Wu, M.; Fearing, R.; Javey, A. *Nano Letters* **2011**, *11*, 3239–3244.

[67] Harroun, T. A.; Fritzsche, H.; Watson, M. J.; Yager, K. G.; Tanchak, O. M.; Barrett, C. J.; Katsaras, J. *Review of Scientific Instruments* **2005**, *76*, 065101.

[68] Burmistrova, A.; von Klitzing, R. *Journal of Materials Chemistry* **2010**, *20*, 3502–3507.

[69] South, A. B.; Whitmire, R. E.; Garcia, A. J.; Lyon, A. L. *ACS Applied Materials and Interfaces* **2009**, *1*, 2747–2754.

[70] Wellert, S.; Kesal, D.; Schön, S.; von Klitzing, R.; Gawlitza, K. *Langmuir* **2015**, *31*, 2202–2210.

[71] Schmidt, S.; Hellweg, T.; von Klitzing, R. *Langmuir* **2008**, *24*, 12595–12602.

[72] Wellert, S.; Richter, M.; Hellweg, T.; von Klitzing, R. *Zeitschrift für Physikalische Chemie* **2014**, *229*, 1225–1250.

[73] Vilgis, T.; Joanny, J.; Johner, A. *Macromolecular Symposia* **2003**, *200*, 67–80.

[74] Mourran, A.; Wu, Y.; Gumerov, R. A.; Rudov, A. A.; Potemkin, I. I.; Pich, A.; Möller, M. *Langmuir* **2016**, *32*, 723–730.

[75] Wellert, S.; Hertle, Y.; Richter, M.; Medebach, M.; Magerl, D.; Wang, W.; Deme, B.; Radulescu, A.; Müller-Buschbaum, P.; Hellweg, T.; von Klitzing, R. *Langmuir* **2014**, *30*, 7168–7176.

[76] Matsui, S.; Nishizawa, Y.; Uchihashi, T.; Suzuki, D. *ACS Omega* **2018**, *3*, 10836–10842.

[77] Mangiapia, G.; Gvaramia, M.; Kuhrts, L.; Teixeira, J.; Koutsioubas, A.; Soltwedel, O.; Frielinghaus, H. *Physical Chemistry Chemical Physics* **2017**, *19*, 32057–32071.

[78] Jaksch, S.; Lipfert, F.; Koutsioumpas, A.; Mattauch, S.; Holderer, O.; Ivanova, O.; Frielinghaus, H.; Hertrich, S.; Fischer, S. F.; Nickel, B. *Physical Review E* **2015**, *91*, 022716.

[79] Müller-Buschbaum, P.; Cubitt, R.; Petry, W. *Langmuir* **2003**, *19*, 7778–7782.

[80] Magerl, D.; Philipp, M.; Metwalli, E.; Gutfreund, P.; Qiu, X.-P.; Winnik, F. M.; Müller-Buschbaum, P. *ACS Macro Letters* **2015**, *4*, 1362–1365.

[81] Al-Baradi, A. M.; Rimmer, S.; Carter, S. R.; de Silva, J. P. .; King, S. M.; Maccarini, M.; Farago, B.; Noirez, L.; Geoghegan, M. *Soft Matter* **2018**, *14*, 1482–1491.

[82] Hertle, Y.; Zeiser, M.; Fouquet, P.; Maccarini, M.; Hellweg, T. *Zeitschrift für Physikalische Chemie* **2014**, *228*, 1053–1075.

[83] Rouse, P. E. *The Journal of Chemical Physics* **1953**, *21*, 1272–1280.

[84] Holderer, O. In *Scattering! Soft, functional and quantum materials*; Angst, M., Brückel, T., Förster, S., Friese, K., Zorn, R., Eds.; Forschungszentrum Jülich GmbH JCNS, PGI, ICS and IAS, 2019; Vol. 190; pp B4(1–15).

[85] Menke, H. Rouse vs. Zimm regime: hydrodynamic interactions. 2015; `https://www.henrimenke.com/documents/hs-theo-handout.pdf`.

[86] Rubinstein, M.; Colby, R. *Polymer physics*; Oxford University Press, 2003.

[87] Zimm, B. H. *The Journal of Chemical Physics* **1956**, *24*, 269–278.

[88] Roters, A.; Johannsmann, D. *J. Phys.: Condens. Matter* **1996**, *8*, 7561–7577.

[89] Gelbert, M.; Biesalski, M.; Rühe, J.; Johannsmann, D. *Langmuir* **2000**, *16*, 5774–5784.

[90] Jaksch, S.; Gutberlet, T.; Müller-Buschbaum, P. *Current Opinion in Colloid & Interface Science* **2019**, https://doi.org/10.1016/j.cocis.2019.04.001.

[91] Gawlitza, K.; Ivanova, O.; Radulescu, A.; Holderer, O.; von Klitzing, R.; Wellert, S. *Macromolecules* **2015**, *48*, 5807–5815.

[92] Frielinghaus, H.; Kerscher, M.; Holderer, O.; Monkenbusch, M.; Richter, D. *Physical Review E* **2012**, *85*, 041408.

[93] Jaksch, S.; Holderer, O.; Gvaramia, M.; Ohl, M.; Monkenbusch, M.; Frielinghaus, H. *Scientific reports* **2017**, *7*, 4417.

[94] Nylander, T.; Soltwedel, O.; Ganeva, M.; Hirst, C.; Holdaway, J.; Arteta, M. Y.; Wadsa, M. *Journal of Physical Chemistry B* **2017**, *121*, 2705–2711.

[95] Pynn, R. *AUR–95–3840 Los Alamos Science* **1990**, *19*.

[96] Jackson, A. J. *Introduction to small–angle neutron scattering and neutron reflectometry*; NIST Center for Neutron Research, Gaithersburg, MD, 2008.

[97] Lindner, P.; Zemb, T.; (Editors), *Neutrons, X-Rays and Light. Scattering methods applied to soft condensed metter*; Elsevier Science B.V., 2002.

[98] Roe, J. R. *Methods of X-ray and neutron scattering in polymer science*; Oxford University Press, 2000; pp 236–261.

[99] 38th IFF Spring School 2007, *Probing the nanoworld*; Forschungszentrum Jülich, 2007.

[100] Hammouda, B. Probing nanoscale structures - the SANS toolbox. 2009; `https://www.ncnr.nist.gov/staff/hammouda/the_SANS_toolbox.pdf`.

[101] Sears, V. F. *Neutron News* **1992**, *3*, 26–37.

[102] Lindner, P., Zemb, T., Eds. *Neutrons, X-Rays and light scattering methods applied to soft condensed matter*; North Holland, 2002.

[103] Gennes, P. G. d. *Scaling concepts in polymer physics*; Cornell University Press Ithaca, N.Y, 1979; pp 1–324.

[104] Porod, G. *Kolloid-Zeitschrift* **1951**, *124*, 83–114.

[105] Pedersen, J. S. *Advances in Colloid and Interface Science* **1997**, *70*, 171–210.

[106] Teixeira, J. *Journal of Applied Crystalography* **1988**, *21*, 781–785.

[107] Grillo, I. In *Soft matter characterization*; Borsali, R., Pecora, R., Eds.; Springer Nature/Springer Netherland, 2008; pp 723–783.

[108] Müller-Buschbaum, P. *Polymer Journal* **2013**, *45*, 34–42.

[109] Santoro, G.; Yu, S. In *X-ray scattering*; Ares, A. E., Ed.; INTECH, 2017.

[110] Lauter-Pasyuk, V. *Collection SFN* **2007**, *7*, 221–240.

[111] Kyrey, T.; Witte, J.; Pipich, V.; Feoktystov, A.; Koutsioubas, A.; Vezhlev, E.; Frielinghaus, H.; von Klitzing, R.; Wellert, S.; Holderer, O. *Polymer* **2019**, *169*, 29–35.

[112] Müller-Buschbaum, P.; Gutmann, P.; Stamm, M.; Cubitt, R.; S., C.; von Krosigk, G.; Gehrke, G.; Petry, W. *Physica B* **2000**, *283*, 53–59.

[113] Yoneda, Y. *Physical Review* **1963**, *131*, 2010–2013.

[114] Schwartzkopf, M.; Roth, S. V. *Nanomaterials* **2016**, *6*, 239.

[115] Born, M.; Wolf, E. *Principles of optics*; Cambridge: Cambridge UniversityPress, 1999.

[116] Nelson, A. *Computer Programs* **2006**, *39*, 273–276.

[117] Korolkov, D. *Structural analysis of diblock copolymer nanotemplates using grazing incidence scattering, Thesis*; Forschungszentrum Jülich, 2008.

[118] Vineyard, G. *Physical Review* **1982**, *26*, 4146.

[119] Milosevic, M. *Applied Spectroscopy* **2013**, *67*, 126–131.

[120] Knoll, W. *Makromol. Chem.* **1991**, *2856*, 2827–2856.

[121] Dosch, H.; Usta, K. A.; Lied, A.; Drexel, W.; Peisl, J. *Review of Scientific Instruments* **1992**, *63*, 5533–5542.

[122] Holderer, O.; Monkenbusch, M.; Schätzler, R.; Kleines, H.; Westerhausen, W.; Richter, D. *Measurement Science and Technology* **2008**, *19*, 034022.

[123] Mezei, F. *Neutron spin echo lecture notes in physics, vol. 128*; Springer: Berlin Heidelberg New York, 1980.

[124] Tanaka, T.; Hocker, L. O.; Benedek, G. B. *Journal of Chemical Physics* **1973**, *59*, 5151–5159.

[125] Doi, M.; Edward, S. In *The theory of polymer dynamics*; Pethrick, R. A., Ed.; Oxford University Press, Oxford, 1988; Vol. 20; pp 1–299.

[126] Campanella, A.; Holderer, O.; Raftopoulos, K. N. *Soft Matter* **2016**, *12*, 3214–3225.

[127] Ewen, B.; Mours, M.; Richter, D.; Shiga, T.; Winter, H. *Neutron spin echo spectroscopy. Viscoelasticity rheology*; Springer–Verlag Berlin Heidelberg, 1997; pp 1–248.

[128] Nouhi, S.; Hellsing, M. S.; Kapaklis, V.; Rennie, A. R. *Journal of Applied Crystallography* **2017**, *50*, 1066–1074.

[129] Kyrey, T.; Ganeva, M.; Gawlitza, K.; Witte, J.; von Klitzing, R.; Soltwedel, O.; Di, Z.; Wellert, S.; Holderer, O. *Physica B: Physics of Condensed Matter* **2018**, 172–178.

[130] Müller-Buschbaum, P. *Advanced Materials* **2014**, *26*, 7692–7709.

[131] Müller-Buschbaum, P.; Wolkenhauer, M.; Wunnicke, O.; Stamm, M.; Cubitt, R.; Petry, W. *Langmuir* **2001**, *17*, 5567–5575.

[132] Müller-Buschbaum, P. *European Polymer Journal* **2016**, *81*, 470–493.

[133] Lipfert, F.; Frielinghaus, H.; Holderer, O.; Mattauch, S.; Monkenbusch, M.; Arend, N.; Richter, D. *Physical Review E* **2014**, *89*, 042303.

[134] Holderer, O.; Frielinghaus, H.; Wellert, S.; Lipfert, F.; Monkenbusch, M.; von Klitzing, R.; Richter, D. *Journal of physics/Conference Series* **2014**, *528*, 012025.

[135] Pasini, S.; Holderer, O.; Kozielewski, T.; Richter, D.; Monkenbusch, M. *Review of scientific instruments* **2019**, *90*, 043107.

[136] Ohl, M. et al. *Nuclear Instruments and Methods in Physics Research Section A* **2012**, *696*, 85–99.

[137] Frielinghaus, H.; Holderer, O.; Lipfert, F.; Monkenbusch, M.; Arend, N.; Richter, D. *Nuclear Instruments and Methods in Physics Research* **2012**, *686*, 71–74.

[138] Frielinghaus, H.; Gvaramia, M.; Mangiapia, G.; Jaksch, S.; Ganeva, M.; Koutsioubas, A. *Nuclear Instruments and Methods in Physics Research, Section A* **2017**, *871*, 72–76.

[139] Borsali, R.; Pecora, R. *Soft matter characterization*; Springer-Verlag: Berlin Heidelberg, 2008.

[140] Pelton, R.; Chibante, P. *Colloids and Surfaces* **1986**, *20*, 247 – 256.

[141] Feoktystov, A. V.; Frielinghaus, H.; Di, Z.; Jaksch, S.; Kleines, H.; Ioffe, A.; Richter, D. *Applied Crystallography* **2015**, *48*, 61–70.

[142] Heinz Maier-Leibnitz Zentrum, *Journal of large-scale research facilities* **2015**, *A28*, 26–29.

[143] Radulescu, A.; Pipich, V.; Frielinghaus, H.; Appavou, M.-S. *Journal of Physics: Conference Series* **2012**, *351*, 012026.

[144] Heinz Maier-Leibnitz Zentrum, *Journal of large-scale research facilities* **2015**, *1*, A29.

[145] Heinz Maier-Leibnitz Zentrum, *Journal of large-scale research facilities* **2015**, *1*, A31.

[146] Steitz, R.; Gutberlet, T.; Hauss, T.; Klo, B.; Krastev, R.; Schemmel, S.; Simonsen, A. C.; Findenegg, G. H. *Langmuir* **2003**, *19*, 2409–2418.

[147] Kentzinger, E.; Krutyeva, M.; Rücker, U. *Journal of large-scale research facilities* **2016**, *2*, 1–5.

[148] Heinz Maier-Leibnitz Zentrum, *Journal of large-scale research facilities* **2015**, *1*, A8.

[149] Burle, J.; Durniak, C.; Fisher, J. M.; Ganeva, M.; Pospelov, W., G.and Van Herck; Wuttke, J.; Yurov, D. BornAgain – Software for simulating and fitting X–ray and neutron small–angle scattering at grazing incidence, Version 1.14.0 (2013–2019). `http://www.bornagaFestoject.org`.

[150] Plamper, F. A.; Richtering, W. *Accounts of Chemical Research* **2017**, *50*, 131–140.

[151] Füllbrandt, M.; von Klitzing, R.; Schönhals, A. *Soft Matter* **2013**, *9*, 4464–4471.

[152] Hashmi, S. M.; Dufresne, E. R. *Soft Matter* **2009**, *5*, 3682–3688.

[153] Ulrych, G. Properties of liquid heavy water, Table 1. `http://hedhme.com/content_map/?link_id=22146&article_id=532`.

[154] Habicht, A.; Schmolke, W.; Goerigk, G.; Lange, F.; Saalwächter, K.; Ballauff, M.; Seiffert, S. *J. of Polymer Science, Part B: Polymer Physics* **2015**, *53*, 1112–1122.

[155] Weitz, D. A. *Science* **2004**, *303*, 968–969.

[156] Wong, P. *Physical Review B: Condensed Matter* **1985**, *32*, 7417–7424.

[157] Witte, J.; Kyrey, T.; Lutzki, J.; Dahl, A. M.; Houston, J.; Radulescu, A.; Pipich, V.; Stingaciu, L.; Kühnhammer, M.; Witt, M. U.; von Klitzing, R.; Holderer, O.; Wellert, S. *Soft Matter* **2019**, *15*, 1053–1064.

[158] Kratz, K.; Hellweg, T.; Eimer, W. *Colloids and Surfaces A: Physicochemical and Engineering Aspects* **2000**, *170*, 137–149.

[159] Hellweg, T.; Dewhurst, C. D.; Eimer, W.; Kratz, K. *Langmuir* **2004**, *20*, 4330–4335.

[160] Schmidt, S.; Motschmann, H.; Hellweg, T.; von Klitzing, R. *Polymer* **2008**, *49*, 749 – 756.

[161] Synytska, A.; Svetushkina, E.; Puretskiy, N.; Stoychev, G.; Berger, S.; Ionov, L.; Bellmann, C.; Eichhorn, K.-J.; Stamm, M. *Soft Matter* **2010**, *6*, 5907–5914.

[162] Lutz, J.-F.; Hoth, A.; Schade, K. *Designed Monomers and Polymers* **2009**, *12*, 343–353.

[163] Gawlitza, K.; Radulescu, A.; von Klitzing, R.; Wellert, S. *Polymer* **2014**, *55*, 6717–6724.

[164] Shibayama, M.; Tanaka, T.; Han, C. C. *The Journal of Chemical Physics* **1992**, *97*, 6842–6854.

[165] Witte, J.; Krause, P.; Kyrey, T.; Ganeva, M.; Dahl, A. M.; Koutsioumpas, A.; Schmidt, B.; Lutzki, J.; Holderer, O.; Wellert, S. *Macromolecules* **2019**, submitted.

[166] Max-Planck-Institut für Festkörperforschung, *Journal of large-scale research facilities* **2015**, *1*, A38.

[167] Förster, S.; Burger, C. *Macromolecules* **1998**, *31*, 879–891.

[168] Schneck, E.; Berts, I.; Halperin, A.; Daillant, J.; Fragneto, G. *Biomaterials* **2015**, *46*, 95 – 104.

[169] Rodriguez-Loureiro, I.; Scoppola, E.; Bertinetti, L.; Barbetta, A.; Fragneto, G.; Schneck, E. *Soft Matter* **2017**, *13*, 5767–5777.

[170] Varma, S.; Bureau, L.; DÃ©barre, D. *Langmuir* **2016**, *32*, 3152–3163.

[171] von Klitzing, R.; Köhler, R.; Chenigny, C. *Multilayer Thin Films*; John Wiley & Sons, Ltd, 2012; Chapter 11: Neutron reflectometry at polyelectrolyte multilayers, pp 219–268.

[172] Boyaciyan, D.; Braun, L.; Löhmann, O.; Silvi, L.; Schneck, E.; von Klitzing, R. *The Journal of Chemical Physics* **2018**, *149*, 163322.

[173] Milner, S. T.; Witten, T. A.; Cates, M. E. *Macromolecules* **1988**, *21*, 2610–2619.

[174] Rauscher, M.; Dietrich, S. In *Handbook of nanophysics: principles and methods*; Sattler, K. D., Ed.; CRC Press, Taylor & Francis Group, 2011; pp 11(1–23).

[175] Teichert, C.; MacKay, J. F.; Savage, D. E.; Lagally, M. G.; Brohl, M. *Applied Physics Letters* **1995**, *66*, 2346–2348.

[176] Nesnidal, R. C.; Walker, T. G. *Applied Optics* **1996**, *35*, 2226–2229.

[177] Khaydukov, Y.; Aksenov, V.; Nikitenko, Y.; Zhernenkov, K.; Nagy, B.; Teichert, A.; Steitz, R.; Rühm, V.; Bottyán, L. *Journal of Superconductivity and Novel Magnetism* **2011**, 961–968.

[178] Kerscher, M.; Busch, P.; Mattauch, S.; Frielinghaus, H.; Richter, D.; Belushkin, M.; Gompper, G. *Physical Review E* **2011**, *83*, 030401.

[179] Frielinghaus, H.; Kyrey, T.; Holderer, O. *JPS Conference Proceedings* **2018**, *22*, 011031.